Mechanisms of activated hepatic stellate cell removal in acute and chronic liver injury

INAUGURAL–DISSERTATION

zur Erlangung des Grades eines

Dr. med. Vet.

beim Fachbereich Veterinärmedizin
der Justus-Liebig- Universität Gießen

Eingereicht von

Reham Hassan

Aus dem Institut für Pharmakologie und Toxikologie
des Fachbereiches veterinärmedizin
der Justus-Liebig- Universität Gießen
Betreuer: Prof. Dr. Joachim Geyer

und

dem Leibniz-Institut für Arbeitsforschung an der TU Dortmund (IfADo)
Betreuer: Prof. Dr. med. Jan G. Hengstler

Mechanisms of activated hepatic stellate cell removal in acute and chronic liver injury

INAUGURAL–DISSERTATION
zur Erlangung des Grades eines

Dr. med. Vet.

beim Fachbereich Veterinärmedizin
der Justus-Liebig- Universität Gießen

Eingereicht von
Reham Hassan
Tierärztin aus South Valley Universität
Qena, Ägypten

Gießen (2017)

Mit Genehmigung des Fachbereich Veterinärmedizin
der Justus-Liebig- Universität Gießen

Dekan: Prof. Dr. h.c. Martin Kramer

Gutachter:

Prof. Dr. Joachim Geyer

Prof. Dr. med. Jan G. Hengstler

Tag der Disputation: 26.09.2017

Table of contents

Abbreviations

AIF	Apoptosis inducing factor
ALT	Alanine transaminase
APAP	Acetaminophen, Paracetamol, n-acetyl-p-aminophen
AST	Aspartate transaminase
BrdU	5-Bromo-2'-deoxyuridine
BSA	Bovine serum albumen
CCL20	chemokine (C-C motif) ligand 20
CCl_4	Carbon tetra chloride
CCR6	Chemokine receptor 6
DAB	3,3’-Diaminobenzidine
DAPI	4′,6-Diamidin-2-phenylindol
DCs	Dendritic cells
ECM	Extra cellular matrix
EDTA	Etyline diamine tetra acetic acid
EGF	Epidermal growth factor
FFPE	Formalin fixed paraffin embedded

FLT3LG	Fms-related tyrosine kinase 3 ligand
H&E	Hematoxylin and eosin
h/min	Hour / minute
HGF	Hepatocytes growth factor
HMGB1	High mobility group box 1
HRP	Horseradish peroxidase
HSCs	Hepatic stellate cells
i.p.	Intraperitoneal
i.v.	Intravenous
IFN-γ	Interferon gamma
IL	Interleukin
IL-1β	Interleukin 1 beta
ILCs	Innate lymphoid cells
Kg/g/mg	Kilogram/gram/milligram
LPS	Lipopolysaccharide
LSECs	Liver sinusoidal endothelial cells
MHC-1	Major histocompatibility complex class 1
MMP	Matrix metalloproteinases

MPT	Membrane permeability transition
NAPQI	N-acetyl-p-benzoquinone imine
NF*k*-B	Nuclear factor kappa-light-chain-enhancer of activated B cells
NK	Natural killer cells
NKT	Natural killer T cells
PBS	Phosphate buffer saline
PDGF	Platelet-derived growth factor
PFA	Paraformaldehyde
RIPK1	Receptor interacting protein kinase 1
ROS	Reactive oxygen species
rpm	Round per minute
SD / SE	Standard deviation/Standard error
SULT	Sulfotransferase
TBS	Tris buffered saline
TGF-β	Transforming growth factor beta
T_H	T helper cells
TIMPs	Tissue inhibitor metalloproteinases
TNF-α	Tumor necrosis factor alpha

TRAIL	Tumor necrosis factor -related apoptosis inducing ligand
TUNEL	Terminal deoxynucleotidyl transferase dUTP nick end labeling
UGT	UDP-glucuronosyltransferas
VEGF	Vascular endothelial growth factor
WNT2	Wingless-type MMTV integration site family, member 2
α-SMA	Alpha-smooth muscle actin
γδ-T cell	Gamma delta T cells

List of figures

List of tables

1. Introduction

The liver is the largest organ of the body and fulfills complex functions. Its strategic location in relation to the blood drained from the intestinal tract and the unique functions of hepatocytes allow it to serve as a filter that prevents passage of absorbed toxins into the systemic circulation (McCuskey 2006; Michalopoulos 2007).

1.1 Structure of the liver

1.1.1 Liver anatomy

The mouse liver is located in the cranial part of the abdominal cavity with a convex surface facing the diaphragm and a concave surface facing the abdominal viscera (Thoolen et al. 2010). It accounts for 5-6% of the total mouse weight. The liver has a dual blood supply: venous blood delivered by the portal vein and arterial blood delivered by the hepatic artery. The portal vein carries non-oxygenated blood collected from the gastrointestinal tract, spleen as well as pancreas and contributes with 75% of the total blood supply of the liver. The hepatic artery delivers oxygenated blood and contributes with 25% of the total blood supply of the liver (Hollander et al. 1987; Vollmar and Menger 2009). The liver is connected to the intestine via the common bile duct which carries bile from the gall bladder to the duodenum (McCuskey 2006). The mouse liver consists of four lobes: left, median, right and caudate (figure 1.1). The left lobe is the largest of the mouse liver. The median lobe is connected to the diaphragm via the coronary ligament (Fiebig et al. 2012) and is divided by incomplete fissure into two segments where the gall bladder is located in between. The right lobe is subdivided horizontally into anterior and posterior portions. The caudate lobe is located at the visceral surface and subdivided into two-small segments (Hollander et al. 1987).

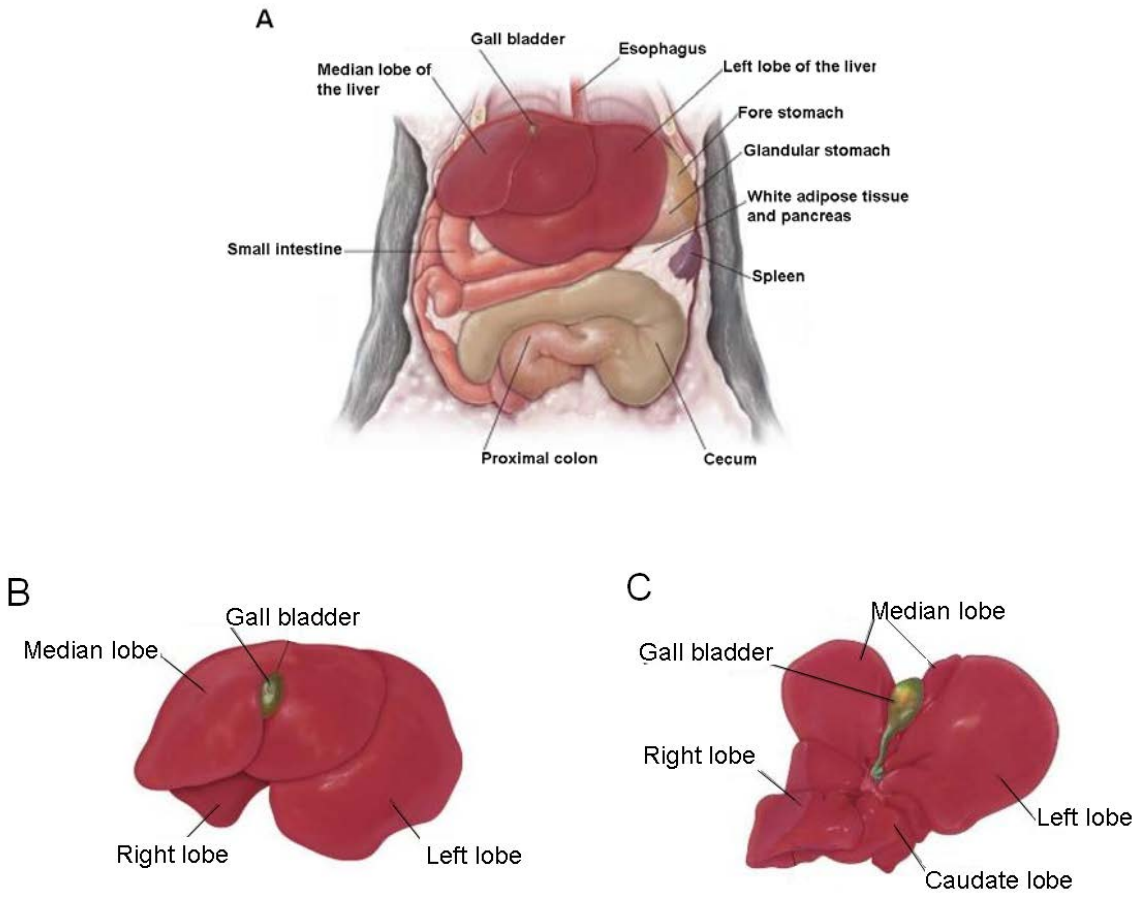

Figure 1. 1: Anatomy of the mouse liver. The liver occupies the cranial third of the abdominal cavity just caudal to the diaphragm (A). It consists of four lobes: left, right, median and caudate (B and C) (Source: Elsevier Inc., WWW.Netterimages.com).

1.1.2 Liver histology

The liver consists of repetitive functional units called lobules (figures 1.2 and 1.3). Branches of the portal vein and the hepatic artery carry the blood to the periportal region of the liver lobule. The blood then flows through the liver sinusoids toward the central vein into the center of the liver lobule. In contrast, bile flux occurs in the opposite direction and leaves the liver lobule in the periportal region via the bile duct (Ishibashi et al. 2009). The liver lobule consists of both parenchymal and non-parenchymal cells. The orchestrated

cooperation between these cells allows the liver to fulfill its functions as well as to efficiently regenerate the lost liver mass following injury.

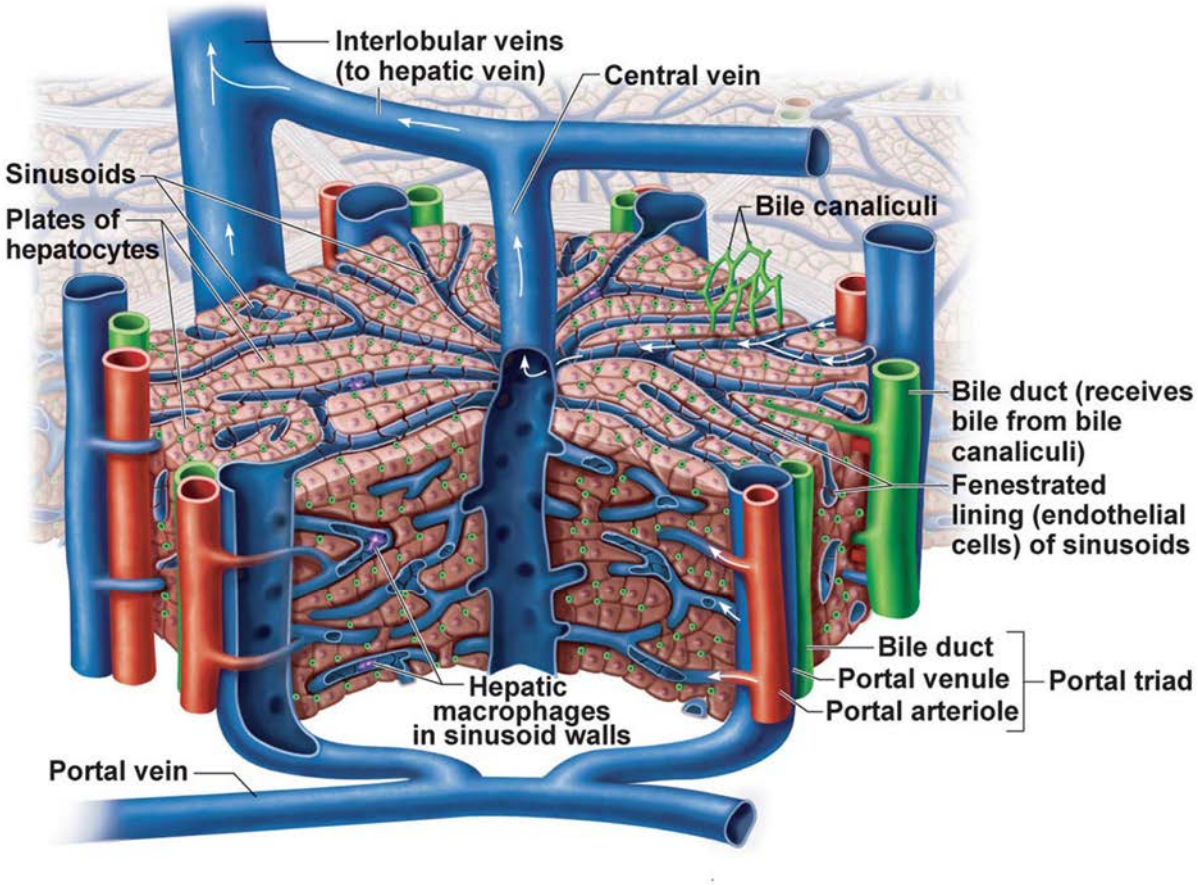

Figure 1. 2: Blood supply and structure of the liver lobule. The liver lobule receives its blood supply at the periportal region via branches of the portal vein and hepatic artery. The blood then flows into the sinusoids (arrows) and drains into the central veins which collect into the liver vein. In contrast, the bile duct which receive bile from the bile canaliculi leaves the liver lobule at the periportal area (Source: https://herbsforhealthandwellbeing.files.wordpress.com/2014/01/bile-caniculi.jpg).

1.1.2.1 Hepatocytes

Hepatocytes (parenchymal cells) are polygonal epithelial cells arranged in 1-2 cell thick plates separated by the blood sinusoids. Hepatocytes make up 80% of the liver mass and approximately 60-65% of the total liver cells number (Gebhardt 1992). The average diameter of hepatocytes is 25-30 µm (McCuskey 2006). Although hepatocytes are homogeneous from the histological point of view, they display heterogeneous functions according to their location along the porto-central axis of the liver lobule (Jungermann

and Kietzmann 1996). There are two well-known metabolic zones in the liver lobule: the periportal zone (zone 1) which involves hepatocytes surrounding the portal vein, and the pericentral zone (zone 3) involving hepatocytes surrounding the central vein (figure 1.3). Hepatocytes in these compartments display different functions. For example, urea synthesis is restricted to the periportal hepatocytes, in contrast glutamine synthesis is restricted to the pericentral hepatocytes (Gebhardt 1992). Moreover, gluconeogenesis occurs predominantly in the periportal area, while glycolysis is most predominant in the pericentral zone (Katz et al. 1977).

Hepatocytes are polarized epithelial cells with basolateral and apical domains (Wang and Boyer 2004). The basal membrane which faces the sinusoids has microvilli to increase the surface area and facilitate the exchange of materials between hepatocytes and blood (figure 1.3). The apical membrane forms the bile canaliculi with the adjacent hepatocytes and also possess microvilli to increase the surface area for bile secretion. Polarity is a critical feature for hepatocytes functions.

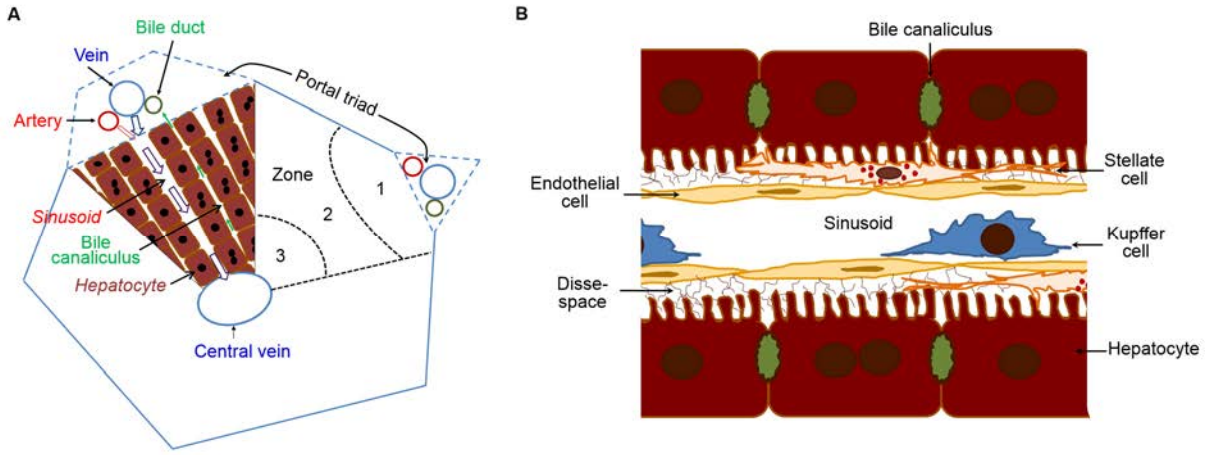

Figure 1. 3: Cellular composition and zonation of the liver lobule. The liver lobule (A) is formed of four major cell types (B): (1) hepatocytes which are arranged in cords and separated from the blood by sinusoidal endothelial cells (2). The basal (facing the endothelial cells) and apical (facing the neighboring hepatocyte) membranes of hepatocyte form microvilli to increase the surface area. The space between hepatocytes and endothelial cells is called Disse space in which another cell type is located called hepatic stellate cells (3). In addition, Kupffer cells (4) are resident within the sinusoidal lumen. The liver lobule contains two distinct metabolic zones: zone 1, involving the periportal hepatocytes, and zone 3, involving the pericentral hepatocytes. In addition, there is a less distinct midzonal area in between (zone 2). (Source: modified from Reif et al. 2017).

1.1.2.2 Liver sinusoidal endothelial cells

Liver sinusoidal endothelial cells (LSECs) represent a unique type of endothelial cells lacking the basement membrane that are fenestrated (Malarkey et al. 2005). They form a barrier between blood and hepatocytes and are separated from hepatocytes by the space of Disse (figure 1.3). LSECs represent approximately 20% of the total liver cells number and 2.8% of the liver volume (Gebhardt 1992). Fenestration of LSECs allows it to control the exchange of fluids and molecules between blood and hepatocytes. Moreover, LSECs play a critical role in liver injury by secretion mitogenic factors (e.g. HGF), which are important for liver regeneration (Ding et al. 2014).

1.1.2.3 Kupffer cell

Kupffer cells (KC), the liver specific macrophages, are located within the sinusoidal lumen (figure 1.3). It account for 8-12% of the total liver cells number and 2.1% of the liver mass (Gebhardt 1992; te Koppele and Thurman 1990). Beside their phagocytic functions, KC play a critical role in liver diseases as they secrete pro-inflammatory cytokines like TNF-α and IL-6 which amplify liver inflammation and affect other liver cells (Ishibashi et al. 2009; Ramadori et al. 2008).

1.1.2.4 Hepatic stellate cells

Hepatic stellate cells (HSCs), also called Ito cells or fat storing cells, are located in the Disse space between hepatocytes and LSECs in healthy liver (figure 1.3). They form about 5% of the total liver cells number and approximately 1.4% of the liver volume (Stockert and Wolkoff 2001). The primary function of HSCs is to store vitamin A and lipids (Malarkey et al. 2005; Senoo 2004). Upon liver injury HSCs get activated, transdifferentiate into myofibroblast like cells, proliferate and migrate to the site of injury where they play a critical role in liver regeneration and fibrosis including production of cytokines, growth factors as well as extracellular matrix (ECM) (Bataller and Brenner

2005; Pellicoro et al. 2014; Senoo 2004).

1.1.2.5 Biliary epithelial cells

Biliary epithelial cells (BECs) form the lining of the bile ducts which carry bile from bile canaliculi to the gall bladder and then to the intestine. It account for approximately 3-5% of the total liver cells number (Ishibashi et al. 2009). It contribute to the final composition and volume of bile (Maroni et al. 2015).

1.1.2.6 Liver associated lymphocytes

In addition to the aforementioned cells, the liver is also enriched in lymphocytes especially natural killer (NK) cells (initially known as pit cells) and natural killer T (NKT) cells. They are resident in the sinusoidal lumen. NK cells provide a line of defense against viral infection and tumors as well as anti-fibrotic action (Nakatani et al. 2004; Seki and Schwabe 2015).

1.2 Acetaminophen induced liver injury: state of the art

Acetaminophen (paracetamol, APAP) is a safe antipyretic and pain relieving drug when used at therapeutic doses (Bessems and Vermeulen 2001; Jaeschke et al. 2011; McGill et al. 2012; Saito et al. 2010). It can be metabolized by sulfation catalyzed by sulfotransferase (SULT) or glucuronidation catalyzed by UDP-glucuronosyltransferase (UGT) leading to products which can easily be excreted (Hinson et al. 2010; Jaeschke 2005). In contrast, overdoses of APAP are commonly associated with acute liver injury both in humans and animals (Bessems and Vermeulen 2001; Jaeschke et al. 2011; McGill et al. 2012). High doses of APAP are metabolized in hepatocytes by cytochrome P-450 enzymes especially the CYP2E1 isoform into a toxic reactive metabolite named N-acetyl-p-benzoquinone imine (NAPQI) (figure 1.4) (Bessems and Vermeulen 2001; Hinson et al. 2010). NAPQI can be trapped by conjugation to glutathione via glutathione-S-transferase

forming glutathione adduct which is safely excreted. Therefore, N-acetyl cysteine is a standard treatment for APAP overdose as it enhance glutathione synthesis (Mitchell et al. 1973). However, high doses of APAP can deplete hepatic glutathione allowing NAPQI to form covalent bonds with cellular and mitochondrial proteins and non-protein thiols which compromise mitochondrial respiration and triggers the release of reactive oxygen species (ROS) (Bessems and Vermeulen 2001; Jollow et al. 1973; McGill et al. 2012; Saito et al. 2010). This leads to formation of peroxynitrite in mitochondria (Jaeschke et al. 2003; Jaeschke et al. 2011) as well as activation of C-Jun NH_2-terminal kinase (JNK), a critical factor in death signaling. Once activated, JNK translocates to the mitochondria where it binds to a scaffold protein in the outer mitochondrial membrane called SAB (Han et al. 2013). This results in further amplification of mitochondrial oxidative stress and peroxynitrite formation which triggers the mitochondrial membrane permeability transition (MPT) leading to loss of mitochondrial function. Furthermore, apoptosis inducing factor (AIF), endonuclease G and cytochrome C are released from the compromised mitochondria and translocate to the nucleus where they induce DNA fragmentation leading to cell death (Bajt et al. 2011; Jaeschke et al. 2003; Jaeschke et al. 2011).

It was reported recently (Guicciardi et al. 2015) that receptor interacting protein kinase 1 (RIPK1) contributes to APAP induced liver injury by activation of JNK. However, the mechanisms of RIPK-1 induced JNK activation are currently unknown (Guicciardi et al. 2015).

It should also be considered that the release of fragmented DNA as well as cellular proteins, for example high mobility group box 1 (HMGB1), from damaged hepatocytes can stimulate Kupffer cells to produce pro-inflammatory cytokines leading to infiltration of immune cells especially neutrophils which can further amplify APAP induced liver injury (Jaeschke 2005; Marques et al. 2015; Williams et al. 2010). Due to the restricted zonation of CYP2E1 to the pericentral region of the liver lobule, this compartment is considered to be the primary target of APAP toxicity.

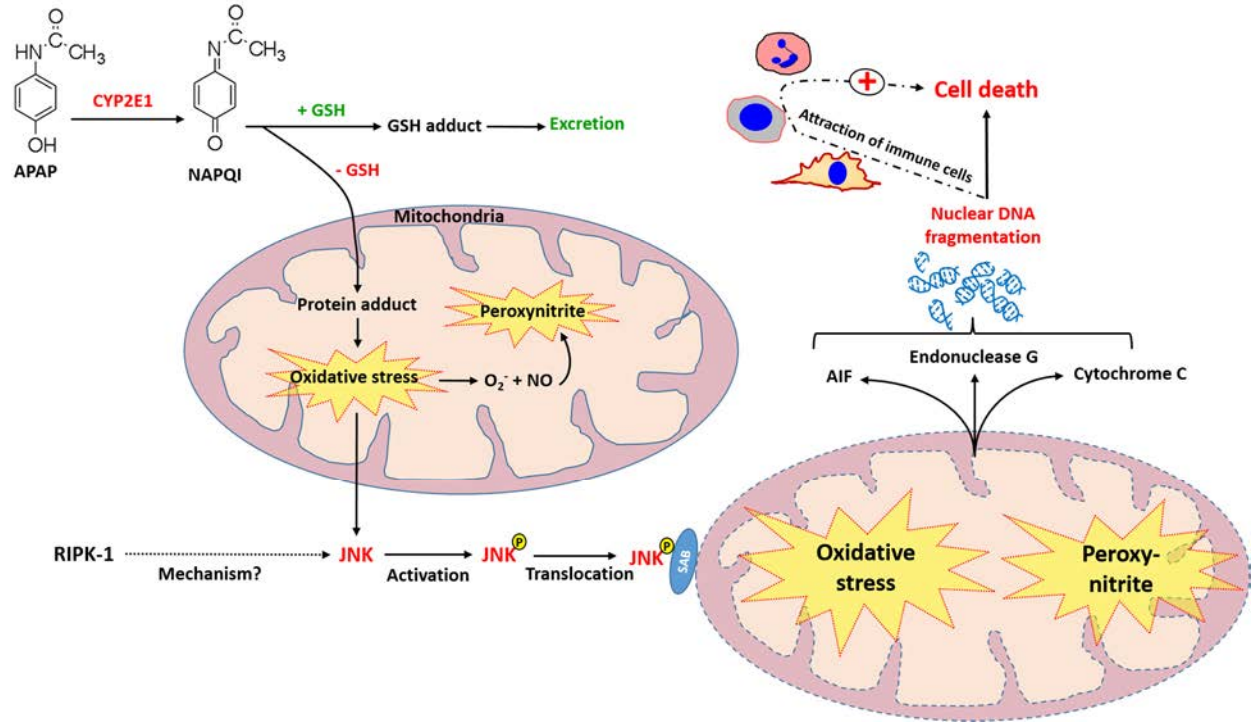

Figure 1. 4: Mechanisms of acetaminophen (APAP) induced liver injury. High doses of APAP are metabolized mainly by CYP2E1 into a reactive metabolite called N-acetyl-p-benzoquinone imine (NAPQI) which bind to mitochondrial proteins and initiate oxidative stress. This results in peroxynitrite formation in the mitochondria, activation and translocation of the death signaling JNK to the mitochondria. Activation of JNK further amplify oxidative stress and peroxynitrite formation leading to induction of mitochondrial permeability transition. As a consequence, apoptosis inducing factor (AIF), endonuclease G and cytochrome C are released from the mitochondria and translocate to the nucleus where they induce DNA damage leading to cell death. The release of damaged DNA to the blood can attract immune cells particularly neutrophils which may further amplify liver inflammation and hepatocytes death.

1.3 Response of the liver to injury: the switch from regeneration to fibrosis

The liver fulfills vital functions of the body particularly metabolic homeostasis and xenobiotics detoxification. Therefore, it is capable to perform a rapid well-orchestrated response upon exposure to injury (Friedman 2012; Michalopoulos and DeFrances 2005; Taub 2004). However, the response of the liver is highly dependent on the duration of injury. For example single exposure to carbon tetrachloride (CCl_4), a hepatotoxic agent that targets the pericentral hepatocytes, is followed by an efficient regenerative response and full recovery of the dead cell area within a week (Ghallab et al. 2016; Hoehme et al. 2010). In contrast, repeated exposure to CCl_4 leads to liver fibrosis (Iredale 2007).

In response to liver injury HSCs get activated and migrate to the site of injury (Iredale et al. 1998). Activated HSCs are the major source of extracellular matrix (ECM) and represent the bottle neck between perfect regeneration and fibrosis (figure 1.5). Acute liver damage leads to a transient activation of HSCs which disappear after regeneration of the dead cell area. In contrast, chronic liver damage leads to compromised regeneration and prolonged activation of HSCs resulting in excessive deposition of ECM and liver fibrosis (Xu et al. 2014).

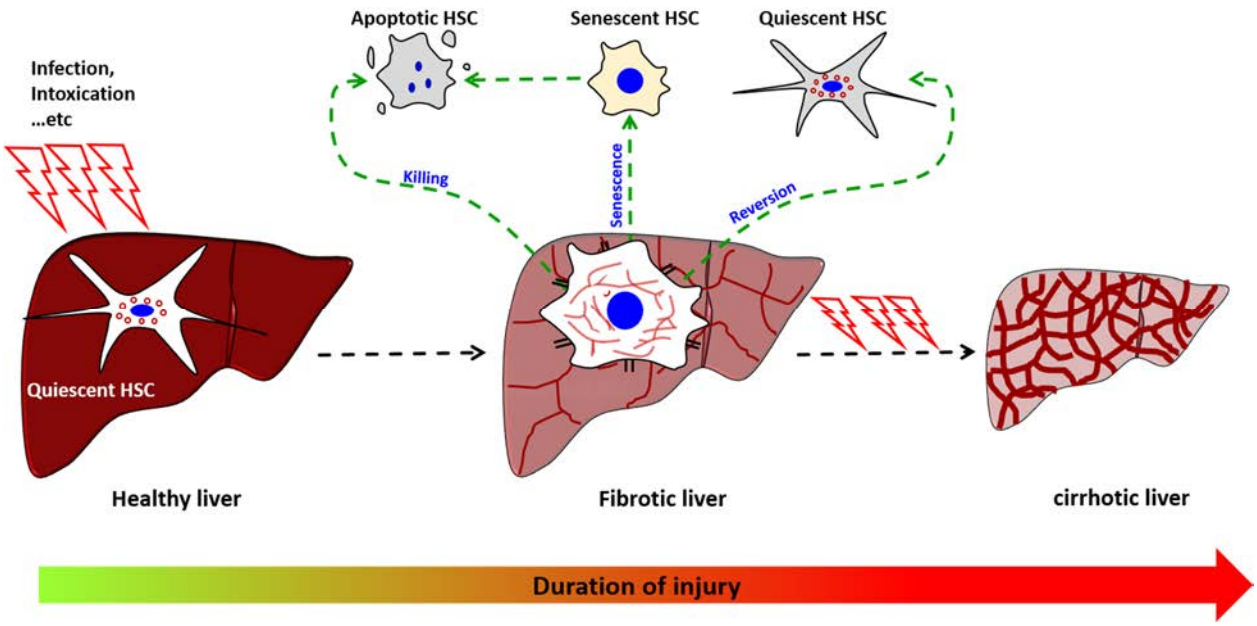

Figure 1. 5: Hepatic stellate cells (HSCs) dynamics after liver injury. Following liver injury HSCs transdifferentiate into myofibroblast-like cells and migrate to the site of injury where they produce extracellular matrix leading to liver fibrosis. However, depending on the duration of injury, this process can be reversible. After cessation of liver injury activated HSCs disappear by apoptosis or by reversion to a quiescent phenotype.

1.3.1 Liver regeneration

Hepatocytes in adult healthy liver are mostly quiescent; the proliferation rate is less than 1% (Taub 2004). In contrast, upon liver injury hepatocytes undergo proliferation leading to full recovery of the dead cell area within a week (Hoehme et al. 2010). Such a rapid regenerative response takes place at the cellular, the lobule as well as the organ level. At the cellular scale, both the parenchymal as well as the non-parenchymal cells cooperate in order to guarantee efficient regeneration of the lost liver mass (figure 1.6). Upon liver injury, some gut-derived factors like lipopolysaccharide (LPS) reach the liver via the portal vein. (Michalopoulos and DeFrances 2005; Taub 2004). This leads to stimulation of Kupffer cells to produce pro-inflammatory cytokines like IL-6 and TNF-α which provide the ideal environment for immune cell infiltration, which prepare the ground for efficient regeneration process (Bohm et al. 2010; Taub 2004). The LSECs play a critical role in liver regeneration. (Ding et al. 2014), reported that the stromal derived factor-1 receptors CXCR7 are upregulated in LSECs upon acute liver injury. This leads to induction of the transcription factor Id1 and production of mitogenic factors such as Wnt2 and hepatocyte growth factor (HGF) which trigger hepatocyte proliferation. Moreover, Hoehme et al, 2010 showed that the newly formed hepatocytes align in the direction of the closest sinusoid; a mechanism which is essential for perfect regeneration. Although HSCs are dangerous in case of chronic liver injury, a transient activation is important for efficient liver regeneration (Shen et al. 2011). The production of ECM help to form a temporary scar at the site of injury which prevents the wound collapse. Moreover, activated HSCs produce HGF which stimulates hepatocytes proliferation (Forbes and Rosenthal 2014). It should also be considered that the hepatic cells also receive extra- hepatic support such as insulin from the pancreas and epidermal growth factor (EGF) from the duodenum and the salivary glands (Taub 2004).

Regeneration at the lobule level is influenced by the type of injury. After loss of pericentral hepatocytes (e.g. after APAP or CCl_4 intoxication) the remaining periportal hepatocytes proliferate and the dead cell area is restored within 6 days (Hoehme et al. 2010). In contrast, surgical removal of some liver lobules leads to a different scenario. The mass of the lost liver lobules is restored by increasing the size of the remaining ones

(Michalopoulos 2007; Taub 2004). At the organ scale, the liver body weight ratio serves as a control system that triggers the turn-off signals once the original mass of the liver is restored (Michalopoulos 2007).

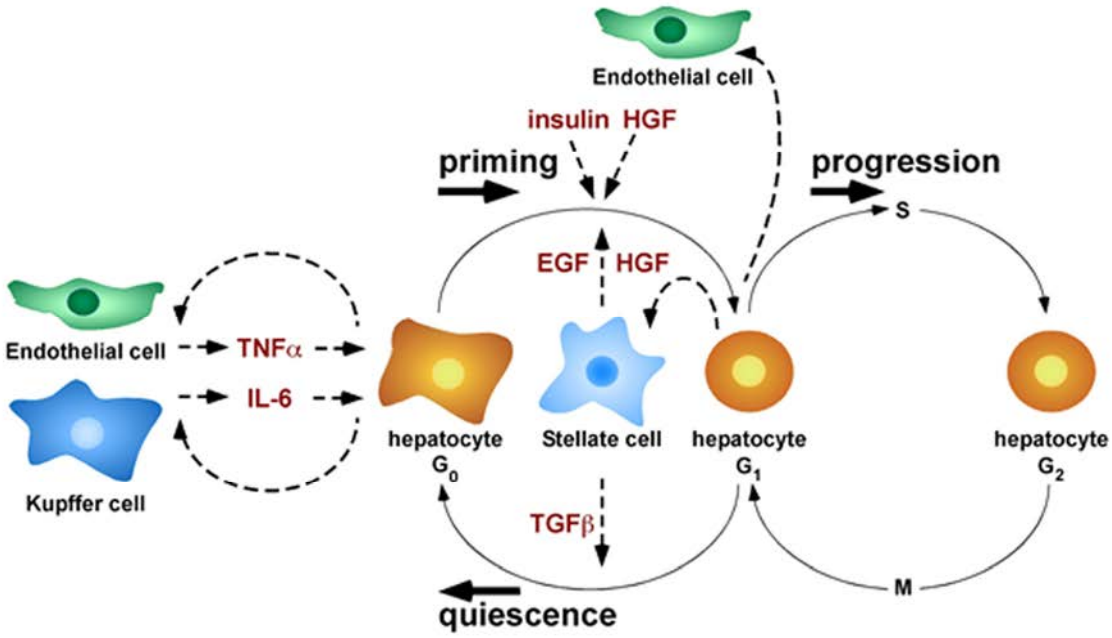

Figure 1. 6: Liver regeneration at the cellular level. Upon liver injury endothelial cells and Kupffer cells are activated to secrete pro-inflammatory cytokines like IL-6 and TNF-α which prime hepatocytes for proliferation. Subsequently, endothelial cells and stellate cells secrete HGF which is a potent hepatocyte mitogen. Once the dead cell area is restored stellate cells release TGF-β which terminate liver regeneration via suppression of the cell cycle (Source: https://www.dkfz.de/en/systembiologie/projekte.html).

1.3.2 Liver fibrosis

Liver fibrosis is a wound healing response in case of chronic liver injury (Pellicoro et al. 2014). It characterized by excessive accumulation of ECM particularly collagen type I and III. Activated HSCs are the major source of ECM (Mallat and Lotersztajn 2013; Ramachandran and Iredale 2012a). Following liver injury, cellular and molecular changes occur leading to trans-differentiation of the quiescent HSCs into myofibroblasts-like cells. Activated HSCs are highly proliferative and acquire the ability to migrate to the site of injury and to produce collagen (Bataller and Brenner 2005; Iredale 2007; Iredale et al. 1998; Kong et al. 2013). Activation of HSCs is orchestrated mainly by interaction with

immune cells (discussed in details below). The spatial expression of ECM in the liver lobule depends on the etiology of liver injury. In cholestatic liver disease [e.g. primary biliary cirrhosis (PBC) and primary sclerosing cirrhosis (PSC)] ECM deposition occurs originally in the periportal compartment of the liver lobule (Pollheimer et al. 2014). In contrast, repeated exposure to hepatotoxins, which target the pericentral hepatocytes (e.g. CCl_4) leads to collagen deposition originally in the pericentral area (Bataller and Brenner 2005; Henderson and Iredale 2007; Ramachandran and Iredale 2012a).

Depending on the duration of injury fibrosis can be reversible (figure 1.7). The reversibility of liver fibrosis is regulated by the balance between matrix metalloproteinases (MMPs) and their tissue inhibitors TIMPs (Liedtke et al. 2013). If the injury is sustained, this leads to permanent upregulation of TIMPs and excessive accumulation of ECM and further progression into cirrhosis and finally liver failure (Bataller and Brenner 2005; Forbes and Rosenthal 2014; Pellicoro et al. 2014). In contrast, when the causative agent is removed, this leads to activation of MMPs and fibrosis regression (Mallat and Lotersztajn 2013; Ramachandran and Iredale 2012a; Tacke and Trautwein 2015). Fibrosis regression occurs in two steps (figure 1.5): (1) elimination of activated HSCs, and (2) degradation of ECM. Elimination of activated HSCs occurs via three mechanisms: first, senescence of activated HSCs which leads to a phenotype with reduced fibrogenic properties and increased susceptibility to killing by immune cells (Kim et al. 2013; Krizhanovsky et al. 2008). Second, apoptosis which is mediated mainly by NK cells (Gur et al. 2012; Radaeva et al. 2006); third, reversion to the quiescent state, however, these cells remain in “a stand by position” and have the potential for rapid fibrogenesis if the injury is repeated (Friedman 2012; Kisseleva et al. 2012; Troeger et al. 2012). Degradation of ECM is mediated by MMPs which are mainly produced by the restorative macrophages (Fallowfield et al. 2007; Ramachandran and Iredale 2012b; Ramachandran et al. 2012). Dendritic cells and endothelial cells contribute also to MMPs production (Tacke and Trautwein 2015).

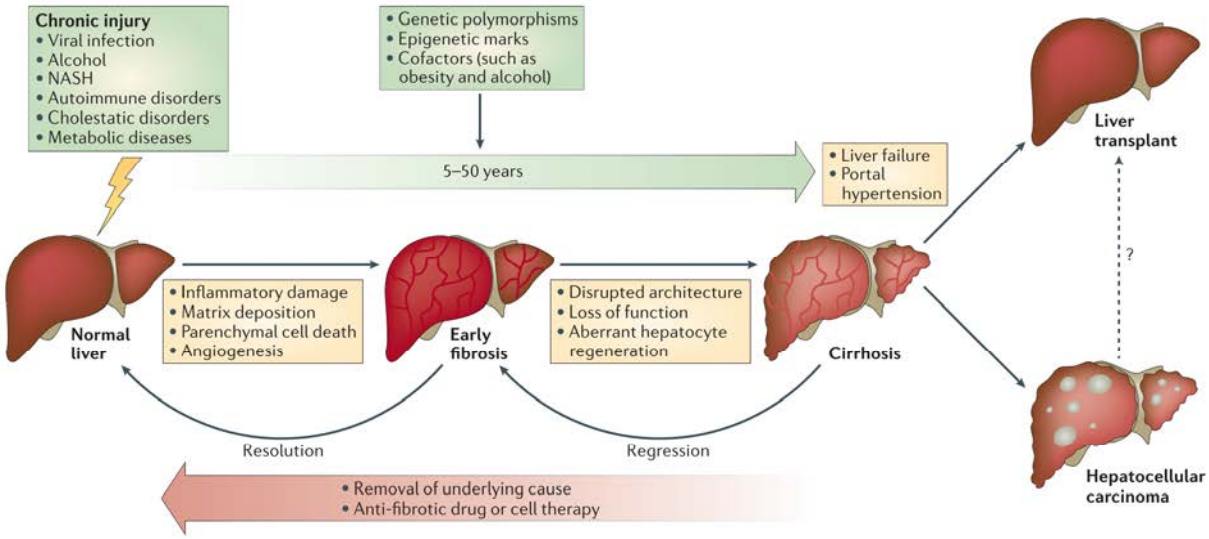

Figure 1. 7: Reversibility of the liver fibrosis. Liver fibrosis develops following chronic liver injury. Depending on the duration of injury it can progress into cirrhosis and finally liver failure. However, cessation of liver injury may allow fibrosis regression in early stages (Source: Pellicoro et al. 2014).

1.3.3 Interaction of immune cells with hepatic stellate cells

Immune cell infiltration is a typical feature to all kinds of liver injury. In addition to their role in liver injury and regeneration they can closely interact with HSCs. Several types of immune cells (figure 1.8) are critical for promoting activation or inactivation/ killing of HSCs, thereby controlling fibrogenesis and fibrosis regression processes.

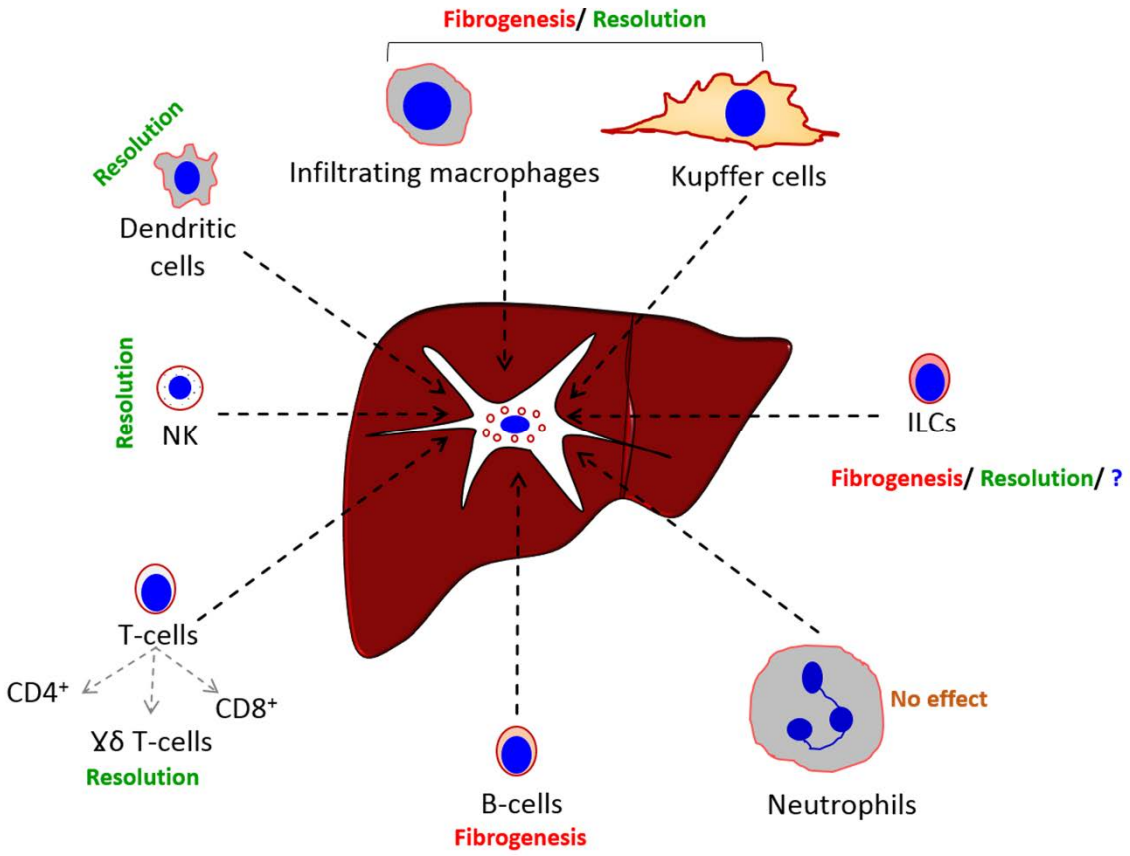

Figure 1. 8: Major cell types which interact with HSCs during fibrogenesis and fibrosis regression. Activation of HSCs is triggered mainly by pro-inflammatory macrophages, whereas, elimination of activated HSCs is induced mainly by restorative macrophages, natural-killer cells, gamma delta T-cells and dendritic cells.

1.3.3.1 Role of macrophages

Macrophages play a key role both during fibrogenesis and fibrosis resolution (Ramachandran and Iredale 2012b; Tacke and Zimmermann 2014) (figure 1.9). The infiltrating macrophages can be differentiated from the liver resident Kupffer cells by the high expression of CD11b ($CD11b^{hi}$) (Ramachandran et al. 2012). Kupffer cells are predominant in healthy liver and decrease upon injury. Based on expression of LY6C, the infiltrating macrophages can be further classified into two-distinct populations: (1) $CD11b^{hi}$ $Ly6C^{hi}$ (pro-inflammatory macrophages) which are predominant during fibrosis progression, and (2) $CD11b^{hi}$ $Ly6C^{lo}$ (restorative macrophages) which infiltrate during

fibrosis resolution (Ramachandran and Iredale 2012b; Ramachandran et al. 2012; Tacke and Zimmermann 2014). Similar macrophage phenotypes have been described during liver damage and regeneration after an acute challenge (Zigmond et al. 2014). Depletion of these macrophage populations in animal models of liver fibrosis reveals distinct opposing roles during fibrosis progression and resolution.

Role of pro-inflammatory macrophages

Depletion of CD11b^{hi} Ly6C^{hi} macrophages during fibrogenesis lead to reduced stellate cells activation (Baeck et al. 2014; Duffield et al. 2005). This is because pro-inflammatory macrophages produce the pro-inflammatory cytokine TGF-β which activate the quiescent HSCs into myofibroblasts-like cells (Duffield et al. 2005; Ramachandran and Iredale 2012b; Seki et al. 2007). In addition, the Ly6C^{hi} macrophages produce platelet-derived growth factor (PDGF) which promotes proliferation and migration of HSCs to the site of injury (Ramachandran and Iredale 2012b; Wang et al. 2016). Furthermore, the pro-inflammatory macrophages maintain the survival of activated stellate cells via production of the pro-inflammatory cytokines IL-1β and TNF-α which are potent stimulators for NF*k*-B pathway (Pradere et al. 2013) (figure 1.9).

Role of restorative macrophages

In contrast to Ly6C^{hi} macrophages, depletion of Ly6C^{lo} macrophages during fibrosis recovery leads to failure of ECM degradation (Duffield et al. 2005; Ramachandran et al. 2012). The restorative macrophages can induce killing of activated HSCs in a TRAIL dependent manner (Fischer et al. 2002). In addition, they are also a rich source of MMPs especially MMP9, MMP12 and MMP13 which induce ECM degradation (Ramachandran et al. 2012; Tacke and Zimmermann 2014) (figure 1.9).

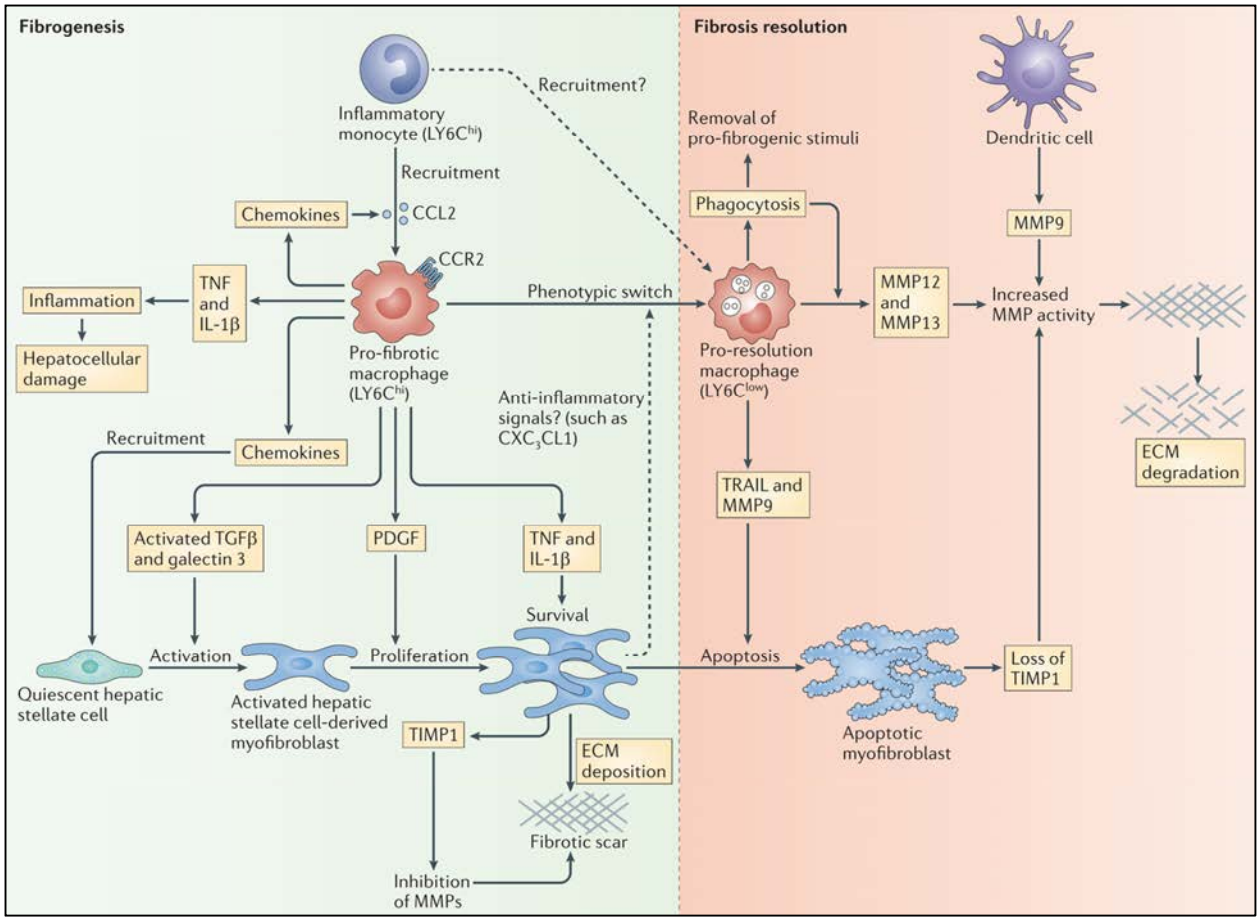

Figure 1. 9: Role of macrophages during fibrogenesis and fibrosis resolution. There are two-different macrophages phenotypes during fibrosis progression and resolution: (1) the pro-inflammatory macrophages, which are recruited during fibrosis progression and are critical for activation (by TGF-β secretion), proliferation (by PDGF secretion) and survival (by TNF-α and IL-β secretion) of hepatic stellate cells (HSCs). (2) The restorative macrophages, which are recruited during fibrosis recovery and are important for killing of activated HSCs (in a TRAIL dependent manner) and degradation of ECM (by production of MMPs) (Source: Pellicoro et al. 2014).

1.3.3.2 Role of dendritic cells

Depletion of dendritic cells (DCs) during fibrosis progression by injection of diphtheria toxins into transgenic mice carrying diphtheria toxins receptors under the direction of CD11C promoter revealed that DCs do not contribute to fibrosis development (Pradere et al. 2013). In contrast, removal of DCs during the fibrosis recovery phase lead to delayed fibrosis resolution (Jiao et al. 2012). This was supported by accelerated fibrosis resolution when the number of DCs was increased either by adoptive transfer or by injection of Fms-

related tyrosine kinase 3 ligand (FLT3LG) which is known to induce the expression of DCs (Masten et al. 2004). DCs enhance fibrosis regression either directly by production of MMP9 (figure 1.9) or indirectly via stimulation of NK cells by production of IFN-γ (Jiao et al. 2012; Lukacs-Kornek and Schuppan 2013).

1.3.3.3 Role of Natural killer cells

Natural killer (NK) cells belong to innate lymphoid cells group 1 and play a critical role in controlling viral hepatitis, tumorigenesis as well as liver fibrosis (Gao et al. 2009; Tian et al. 2013). The cytotoxic action of NK cells is controlled by the balance between inhibitory and stimulatory receptors expressed on its surface and the corresponding ligands expressed on the target cells (Fasbender et al. 2016; Tian et al. 2013) (figure 1.10). The stimulatory receptors are NKG2D, NKP46, NKP44 and NKP30. They interact with the activating ligands expressed on the target cells including MICA and retinoic acid early inducible 1 (RAE1) leading to NK cell activation. Inhibition of NK cells is mediated by the inhibitory receptors LY49A and NKG2 in mice which interact with the major histocompatibility complex class 1 (MHC-1) molecule expressed on the target cells leading to NK cells suppression. Additionally, NK cell cytotoxicity is also regulated by several cytokines. Examples for cytokines which induce NK cells activation are type-1 IFNs, IFN-γ, IL-2, IL-15, IL-12 and IL-18. In contrast, TGF-β and IL-10 are potent inhibitors for NK cell (Gao and Radaeva 2013; Tian et al. 2013).

Several studies showed that activation of NK cells ameliorate liver fibrosis (Gao et al. 2009; Radaeva et al. 2006). This was confirmed by enhanced liver fibrosis when NK cell is blocked by administration of specific antibodies. NK cells can kill HSCs either directly by expression of the death receptors ligands TRAIL or by production of cytokines particularly IFN-γ (Radaeva et al. 2006). It was reported that NK cells kill only the early activated and senescent stellate cells but not the quiescent and the fully activated HSCs (Gao et al. 2009). However, it should be considered that this was based on in vitro experiments.

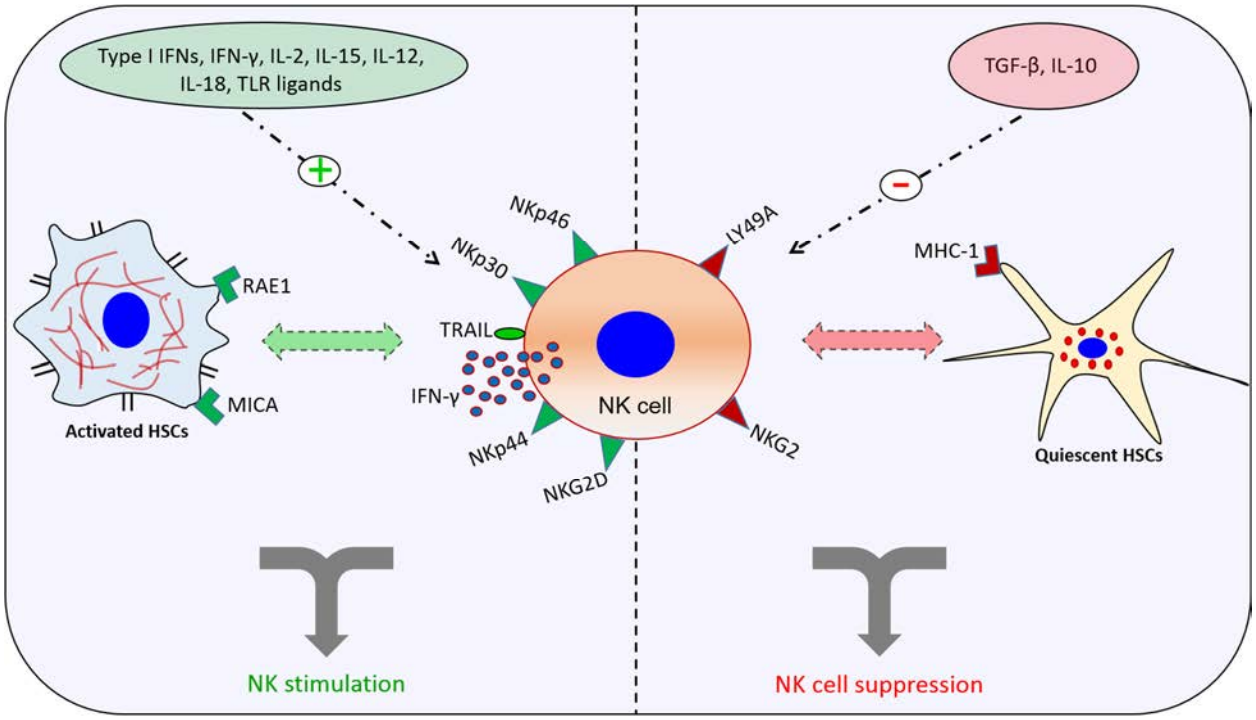

Figure 1. 10: Regulation of natural killer (NK) cells. NK cells are controlled by the balance between inhibitory (LY49A and NKG2) and stimulatory (NKp46, NKp30, NKp44 and NKG2D) receptors and the interaction with the corresponding ligands (RAE1, MICA or MHC1) expressed on the target cells. In addition, NK cells can be activated or suppressed by cytokines. The NK cells stimulatory cytokines are Type I IFNs, IFN-γ, IL-2, IL-15, IL-12, IL-18, TLR ligands. In contrast, TGF-β, IL-10 are potent NK cells inhibitors.

1.3.3.4 Role of Innate lymphoid cells

Innate lymphoid cells (ILCs) are a group of innate immune cells belongs to lymphocytes but lacks a B or T cell receptors (Zook and Kee 2016). Little is known about their role in liver fibrosis. Based on their products ILCs can be subdivided into three groups: group 1, which include NK cell, produce mainly IFN-γ and TNF-α. Group 2, produce mainly IL-4, IL-5, IL-9 and IL-13 (Artis and Spits 2015; Zook and Kee 2016). (McHedlidze et al. 2013), reported that this group is involved in fibrosis progression by activation of HSCs in IL-13 dependent manner. Group 3 ILCs are mainly present in the intestinal tract and produce TNF, IL-17A and IL-22 (Artis and Spits 2015).

1.3.3.5 Role of Neutrophils

It is well known that neutrophils play a critical role in amplification of liver damage (Marques et al. 2015). However, it has no role neither in the activation nor in the killing of HSCs (Moles et al. 2014). Induction of fibrosis in transgenic mice lacking the myeloid related proteins, which are important for recruitment of neutrophils to the site of injury, respond in a similar way as the wild type mice.

1.3.3.6 Role of the adaptive immune cells

The role of T cells in liver fibrosis was discussed controversially. Mice lacking T cells ($CD4^+$, $CD8^+$ and γδ-T cell) have unaltered fibrosis induced by repeated administration of hepatotoxins (Henderson and Iredale 2007; Novobrantseva et al. 2005; Seki and Schwabe 2015). However, a recent study (Hammerich et al. 2014) utilizing mice lacking γδ-T cell showed that they are important for fibrosis resolution. The anti-fibrotic action of γδ-T cell is mediated by killing of activated HSCs in a Fas-Ligand dependent.

B-cell represents 50% of intrahepatic lymphocytes (Seki and Schwabe 2015). Utilizing mice deficient in B cells, it was reported that they are important for fibrosis progression (Novobrantseva et al. 2005). B cells enhance fibrogenesis in an immunoglobulin and T cells independent manner. This is because using mice which have normal number of B cells but are deficient in immunoglobulins or T cells developed similar fibrosis as in the wild type mice.

1.4 Aim of the work

Fibrotic regeneration is a wound healing response in case of chronic liver injury. In contrast, perfect liver regeneration occurs following acute damage without deposition of any detectable extracellular matrix. Although the mechanisms of hepatic stellate cell (HSC) activation and elimination are extensively studied during liver fibrosis and fibrosis recovery, little is known about the role of HSC following acute liver injury. The overarching goal of this thesis is to investigate HSC dynamics during liver injury and regeneration following an acute challenge and to identify the mechanisms that protect against liver fibrosis. The work program on path to this goal is structured into the following tasks:

- Study liver injury and regeneration following intoxication with a single high dose of acetaminophen (APAP) as a model of acute liver injury.
- Identify the liver resident as well as infiltrating immune cells during liver injury and regeneration which might interact with HSC.
- Investigate HSC activation following liver injury and their fate during recovery.
- Study the impact of macrophage depletion during liver regeneration on HSC clearance.
- Identify the possible backup mechanisms that protect against liver fibrosis after macrophage removal.

2. Materials and methods

2.1 Materials

2.1.1 Chemicals

Chemical	Company
123 count eBeads	ebioscience, San Diego, California United States
2-Methylbutane	Sigma-Aldrich Corp., St. Louis, MO, USA
2-propanol	Carl Roth, Karlsruhe, Germany
5-Bromo-2-deoxyuridine (BrdU)	Sigma-Aldrich Corp., St. Louis, MO, USA
Acepromazine	Fatro, Ozzano Emilia (BO), Italy
Acetaminophen	Sigma-Aldrich Corp., St. Louis, MO, USA
Acetic acid	Carl Roth, Karlsruhe, Germany
Albumin bovine fraction V	Carl Roth, Karlsruhe, Germany
Aquatex mountig agent	Merk, Darmstadt, Germany
Carbon tetrachloride	Sigma-Aldrich Corp., St. Louis, MO, USA
Citric acid monohydrate	Carl Roth, Karlsruhe, Germany
DAPI, 4,6 diamidino 2 phenylindole	Invitrogen GmbH, Karlsruhe, Germany
Disodium hydrogen phosphate	Applichem GmbH, Darmstadt, Germany
DPBS (Ca/Mg-free)	Life Technologies (Thermo Scientific), Braunschweig, Germany
Entellan	Merk, Darmstadt, Germany
Eosin Y disodium salt	Sigma-Aldrich Corp., St. Louis, MO, USA
Ethanol, absolute	Carl Roth, Karlsruhe, Germany
Ethyline diamine tetra acetic acid disodium salt (EDTA)	Sigma-Aldrich Corp., St. Louis, MO, USA

FluorPreserve Reagent	EMD Millipore, Billerica, USA
Glucose	Sigma-Aldrich Corp., St. Louis, MO, USA
HI-FCS	PAN-Biotech, Aidenbach, Germany
Histo acryl	B\Braun, Tuttingen, Germany
Hydrochloric acid 4 mol/L	Carl Roth, Karlsruhe, Germany
Hydrogen peroxide 30%	Carl Roth, Karlsruhe, Germany
Ketamin-ratiopharm 50 mg	Ratio pharm, Ulm, Germany
Leica tissue freezing medium	Leica Microsystems, Wetzlar, Germany
Mayer´s Hemalum solution	Merk, Darmstadt, Germany
Methanol	Carl Roth, Karlsruhe, Germany
Methanol free formaldahyde	Carl Roth, Karlsruhe, Germany
NEG-50 tissue freezing medium	Thermo Scientific, Braunschweig, Germany
OneComp eBeads	ebioscience, San Diego, California United States
Paraffin histowax	Leica Microsystems, Wetzlar, Germany
Percoll	Sigma-Aldrich Corp., St. Louis, MO, USA
Potassium chloride	Sigma-Aldrich Corp., St. Louis, MO, USA
Potassium dihydrogen phosphate	Sigma-Aldrich Corp., St. Louis, MO, SA
Roti-histo-fix 4 %	Carl Roth, Karlsruhe, Germany
Roti-histol	Carl Roth, Karlsruhe, Germany
RPMI-1640 medium (RPMI)	PAN-Biotech, Aidenbach, Germany
Sodium acetate anhydrous	Carl Roth, Karlsruhe, Germany

Sodium chloride	Sigma-Aldrich Corp., St. Louis, MO, USA
Sodium hydroxide	Merk, Darmstadt, Germany
Tris	Carl Roth, Karlsruhe, Germany
Triton X-100	Carl Roth, Karlsruhe, Germany
Trizma Hydrochloride	Sigma-Aldrich Corp., St. Louis, MO, USA
Trypan blue working solution	Sigma-Aldrich Corp., St. Louis, MO, USA
Tween 20	Sigma-Aldrich Corp., St. Louis, MO, USA
Tween 80	Sigma-Aldrich Corp., St. Louis, MO, USA
UltraComp eBeads	ebioscience, San Diego, California United States
UltraPure 0.5M EDTA, pH 8.0	Thermo Scientific, Braunschweig, Germany
Xylazine 2%	Bayer health care, Leverkusen, Germany
Zombie Red	Biolegend, Koblenz, Germany

2.1.2 Consumables

Material	**Company**
Cover glass	Thermo Scientific, Braunschweig, Germany
Cell strainer 70um (50Stk)	VWR, Darmstadt, Germany
Cryomold tissue-Tek	Science services GmbH, Munchen, Germany
Dako pen	DakoCytomation, Glostrop, Denmark
Embedding cassettes	Carl Roth, Karlsruhe, Germany

Falcon tube	Sarstedt, Numbrecht, Germany
Filter paper	Carl Roth, Karlsruhe, Germany
Gentle MACS C Tubes	Miltenyi, Bergisch Gladbach, Germany
Inject – f	B\Braun, Wertheim, Germany
Microscopic slides	Thermo Scientific, Braunschweig, Germany
Pipette tip	Sarstedt, Numbrecht, Germany
Safe seal tubes	Sarstedt, Numbrecht, Germany
Serological pipettes	Sarstedt, Numbrecht, Germany
Sterican - 0,3 x 12 – 30 g x ½	B\Braun, Wertheim, Germany
24-well plate	Sarstedt, Numberecht, Germany
96-Well assay plate	Corning Incorporated, USA

2.1.3 Instruments

Instrument	**Company**
Balance BL150S	Sartorius AG, Göttingen, Germany
Confocal laser scanning microscope	Olympus BX61 microscope, Hamburg, Germany
Cool centrifuge	Thermo Scientific, Braunschweig, Germany
EC 350 – modular tissue embedding center	Microm, Walldorf, Germany

Fluorescence microscope BX41	Olympus, Hamburg, Germany
Gentle MACS Octo Dissociator	Miltenyi, Bergisch Gladbach, Germany
HM 450 sliding microtome	Microm, Walldorf, Germany
Incubator	Binder GmbH, Tuttlingen, Germany
Leica CM 3050s-cryostate	Leica Microsystems, Wetzlar, Germany
Micro plate reader, infinite M200 PRO	Tecan, Switzerland
Microwave	Sharp Electronics (Europe) GmbH, Hamburg, German
pH meter lab 850	S1 analytics GmbH, Mainz, Germany
Shaker	Rocking Platform, VWR
Spin tissue processor STP 120	Microm, Walldorf, Germany
Steam cooker	Braun, Germany
Stirrer	IKA RCT classic, Germany
Vibratome Leica VT 1000S	Leica Microsystems, Wetzlar, Germany
Vortex	Beyer GmbH, Dusseldorf, Germany
Water bath	GFL, Burgwedel, Germany

2.1.4 Buffers and solutions

1X Acetate buffer, pH 5.2	• 6.48 g of sodium acetate anhydrous • 1 L of distilled H_2O • 1.21 ml of 100% glacial acetic acid
0.01 M Citrate buffer, pH 6.0	• 2.1 g citric acid monohydrate • Filled up to 1 L with distilled H_2O • set to pH 6 with NaOH
0.1M Tris/ HCl, pH 7.6	• 15.76 g trizma hydrochloride • Filled up to 1 L with distilled H_2O • Set pH to 7.6 with NaOH
0.3% BSA in 3% tween 80 in PBS	• 300 mg BSA • 3 ml Tween 80 • Filled up to100 ml 1X PBS
10 mmol/L Tris buffer, 1 mmol/L EDTA (pH 9.0)	• 12.114 g Tris • 372.2 mg Na_2EDTA • Filled up to 1 L with distilled H_2O
10x TBS, pH 7.4	• 80 g NaCl • 2 g KCl • 30 g Tris • Filled up to 5 L with distilled H_2O
1X PBS/BSA	• 1 g BSA • 2.03 g NaCl • 100 ml of 1X PBS
1x TBS-T	• 1L 1X TBS, • 5 ml Tween 20
3% BSA in 3% tween 80 in PBS	• 3 g BSA • 3 ml Tween 80 • Filled up to 100 ml with 1X PBS

3%PFA: PBS	• 150 ml of roti-histo-fix 4 % • 50 ml 1X PBS
4% Paraformaldehyde methylene free	• 26.66 ml of 30% methylene free formaldehyde • 173.34 ml 1X PBS
4% PFA: 30% glucose (1:1)	• 30 g of glucose • filled up to 100 ml with 1X PBS • Add 100 ml roti-histo-fix 4%
Blocking buffer	• Fc block (CD16/32 antibody) 1:100 in FACS buffer
Blocking solution for endogenous peroxidases	• 667 µL of hydrogen peroxide (H_2O_2 30%) • 200 ml of methanol
EDTA (anti-coagulant)	• 32 mg Na_2EDTA • 1 ml distilled H_2O
Eosine 1%	• 1 g Eosin Y disodium salt • 100 ml distilled H_2O • 1 drop glacial acetic acid
FACS buffer	• 500 ml PBS • 10 ml FCS-HI • 2 ml 0,5 M EDTA • Set pH to 8
FC wash medium	• RPMI-1640 medium • 1% Pen/Strep
Full RPMI-1640 medium	• RPMI-1640 wash medium • 10% FCS (heat inactivated)
Lympholyte-M	• 72 mL original Percoll solution • 8 mL 10X sterile PBS • 120 mL wash medium

Mouse anesthesia	• 64 mg/kg ketamine 5% • 7.2 mg/kg xylazine 2% • 1.7 mg/kg acepromazine • Filled up to 1 ml with 1X PBS
NaCl 0.85%	• 8.5 g NaCl • Filled up to 1L with distilled H_2O
NaOH 10 M	• 40 g NaOH • 100 ml distilled H_2O
Normal donkey serum	Jackson Immuno-Research Laboratories, USA
Normal goat serum	Vecctor laboratories, Burlingame,USA
Normal swine serum	Vecctor laboratories, Burlingame,USA
PBS (10x)	• 10 g KCl • 10 g KH_2PO_4 • 400 g NaCl • 46 g Na_2HPO_4 • Filled up to 5 L with distilled H_2O • Set pH to 7.4

2.1.5 Commercial kits

Kit	Company
AEC^+ high sensitivity substrate chromogen	DakoCytomation, Glostrop, Denmark
Alanine aminotransferase assay kit	Sigma-Aldrich Corp., St. Louis, MO, USA
Aspartate aminotransferase assay kit	Sigma-Aldrich Corp., St. Louis, MO, USA
Avidin and biotin blocking kit	Vector laboratories, Burlingame, USA
Clodronate Liposomes and PBS Liposomes per 10ml	Clodronate Liposomes, Netherlands, Amsterdam

DAB substrate kit	Vector laboratories, Burlingame, USA
Dako envesion+system-HRP (AEC) mouse kit	DakoCytomation, Glostrop, Denmark
Dako envesion+system-HRP (AEC) rabbit kit	DakoCytomation, Glostrop, Denmark
DeadEnd colorimetric TUNEL kit	Promega, Mannheim, Germany
DeadEnd fluorometric TUNEL kit	Promega, Mannheim, Germany
Liver Dissociation Kit mouse	Miltenyi, Bergisch Gladbach, Germany
MaxFluor mouse on mouse immunofluorescence detection kit	MaxVision Biosciences, Dianova, Hamburg, Germany
Peroxidase-conjugated streptavidin	Jackson Immuno-Research Laboratories, Dianova, Hamburg, Germany
Picrosirius red stain kit	Polyscience Europe GmbH, Eppelheim, Germany
Red blood cell lysis ACK	Thermo Scientific, Braunschweig, Germany
RQ1 RNase-free DNase	Promega, Mannheim, Germany

2.1.6 Antibodies

2.1.6.1 Primary antibodies

2.1.6.1.1 Primary antibodies used in Immunohistochemistry staining

Antibody	Company	Catalog number
Polyclonal rabbit anti-human CD3	DakoCytomation, Glostrop, Denmark	A0452
DPPIV/CD26 ectodomain	R&D system, Minneapolis, MN, USA	AF954

Monoclonal mouse anti human smooth muscle action (clone 1A4)	DakoCytomation, Glostrop, Denmark	M0851
Mouse monoclonal anti-alpha smooth muscle actin (clone 1A4)	Abcam, Cambridge, UK	Ab7817
Rabbit polyclonal antibody anti-cytochrome P450 2E1	Enzo Life Sciences GmbH, Stressgen, Victoria, BC, Canada	ADI-MFO-100
Rabbit polyclonal anti-alpha smooth muscle actin	Abcam, Cambridge, UK	Ab5694
Rabbit polyclonal anti-desmin	Thermo Scientific, Braunschweig, Germany	RB-9014-P0
Rat anti-BrdU (clone BU1/75)	AbD Serotec, Bio-Rad, Puchheim, Germany	MCA2060
Rat anti-human/mouse CD45R (B220) purified (clone RA3-6B2)	eBioscince, Frankfurt am Main Germany	14-0452
Rat anti-mouse CD45 (clone 30-F11)	BD Bioscience, Heidelberg, Germany	550539
Rat anti-mouse F4/80 (clone Cl:A3-1)	AbD Serotec, Bio-Rad, Puchheim, Germany	MCA497
Rat anti-mouse LY6G (clone 1A8)	BD Bioscience, Heidelberg, Germany	551459

2.1.6.1.2 Primary antibodies used in flow cytometric staining

Antibody + Fluorophore	**Company**	**Catalog number**
CD11c - BV421	Biolegend, Koblenz, Germany	117329

CD11b - BV510	Biolegend, Koblenz, Germany	101245
CD45 - PerCP	Biolegend, Koblenz, Germany	103130
NK1.1 - BV421	Biolegend, Koblenz, Germany	108732
CD19 - BV510	Biolegend, Koblenz, Germany	115545
CD4 -FITC	Biolegend, Koblenz, Germany	100510
CD8 - PE	Biolegend, Koblenz, Germany	100708
CD3 - AF700	Biolegend, Koblenz, Germany	100216
Fc blocker (CD16/32 Antibody)	Biolegend, Koblenz, Germany	101302

2.1.6.2 Secondary antibodies

Antibody	Company	Catalog number
Alexa Fluor 647 affinipure F(ab)2 fragment donkey anti-rat IgG (H+L)	Jackson Immuno-Research Laboratories, Dianova, Hamburg, Germany	712-606-153
Biotinylated rabbit anti-rat IgG (H+L)	Vector laboratories, Burlingame, USA	BA-4001
Cy3 affiniPure F(ab)2 fragment donkey anti-rabbit IgG (H+L)	Jackson Immuno-Research Laboratories, Dianova, Hamburg, Germany	711-166-152
Donkey F(ab)2 anti-goat IgG (H+L)-alexa fluor 488	Jackson Immuno-Research Laboratories, Dianova, Hamburg, Germany	705-546-147
Polyclonal swine anti-rabbit immunoglobulin/HRP	DakoCytomation, Glostrop, Denmark.	P0217

2.2 Methods

2.2.1 Animal models of liver damage

2.2.1.1 Experimental animals

8-10 weeks old male C57Bl/6N mice, 20-25 g weight, were used (Janvier labs, France). The mice were fed ad libitum with Ssniff R/M-H, 10 mm standard diet (Ssniff, Soest, Germany) and housed at controlled ambient temperature of 25° C with 12 h day, 12 h night cycles. All experiments were approved by the local animal ethics committee.

2.2.1.2 Induction of acute liver damage by acetaminophen

In order to induce acute pericentral liver damage in mice, various doses of acetaminophen (50 up to 500 mg/kg as indicated in the results section) were dissolved in warm PBS and injected intraperitoneally (i.p.). The application volume was 20 ml/kg. The mice were either fed ad libitum or overnight fasted before APAP administration as indicated in the results section. Three to five mice were used for each dose and time point.

2.2.1.3 Induction of acute liver damage by CCl_4

For induction of liver damage in mice by CCl_4, a dose of 1.6 g/kg was injected i.p. in olive oil (1:4). The application volume was 4 ml/kg. The mice were fed ad libitum before and after CCl_4 administration. Three mice were used for each time point.

2.2.1.4 Induction of chronic liver damage by CCl_4

In order to induce liver fibrosis in mice, a dose of 1 g/kg CCl_4 dissolved in olive oil (1:4) was administered i.p. twice a week for two months. The mice were fed ad

libitum along the entire experimental period. Following the last CCl_4 dose, three mice were scarified time dependently up to day ten.

2.2.2 Macrophages depletion

Depletion of macrophages was done by intravenous tail vein injection of clodronate containing liposomes (50 mg/kg) (Clodronate liposomes.org) either before or after APAP injection as indicated in the results section. For long-term depletion of macrophages the injection was repeated every three days. The protocol is based on that liposomes can be easily phagocytosed by macrophages. Clodronate can then be released and accumulated within macrophages after disruption of the liposomal membranes by the influence of lysosomal phospholipases. After exceeding a threshold concentration, it induces macrophages killing by apoptosis (figure 2.1) (Wang et al. 2009).

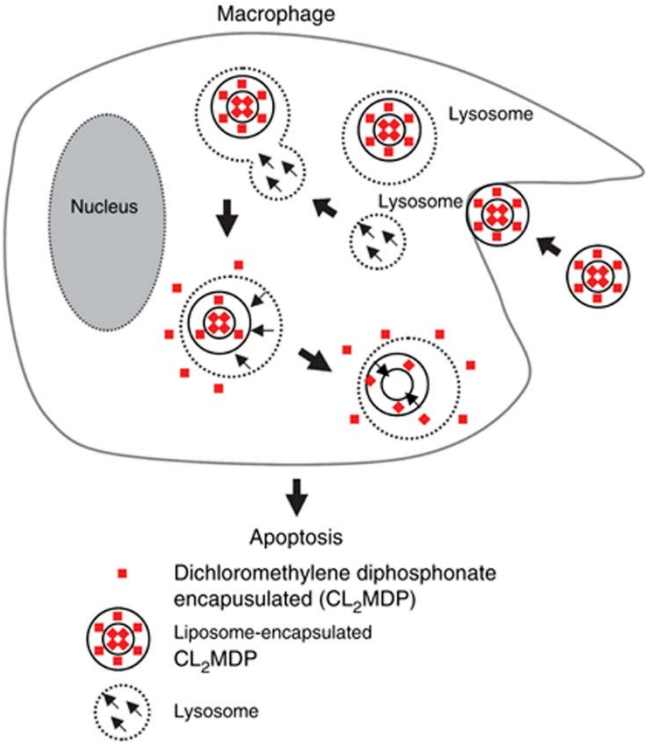

Figure 2. 1: Mechanism of clodronate-induced macrophages killing. After phagocytosis of liposomes by macrophages, their membrane is disrupted by the action of liposomal phospholipase. This lead to release and accumulation of clodronate within macrophages. When a certain concentration was reached, clodronate can induce macrophages apoptosis. (Source: Wang et al. 2009).

2.2.3. Mouse surgery and samples collection

At the indicated time points mice were anaesthetized by an i.p. injection of ketamine (64 mg/kg), xzylazine (7.2 mg/kg) and acepromazine (1.7 mg/kg). After loss of all mouse reflexes, the skin was dissected and a midline incision was made in the abdominal wall below the sternum.

Blood samples were collected from three positions in mice according to Ghallab et al. (2016): (1) the portal vein (representing 75% of the liver inflow), (2) the liver vein (representing the liver outflow), and (3) the right heart chamber (representing the mixed venous blood). For exposure of the liver vein the median liver lobe was reflected cranially, whereas the left liver lobe was pushed caudally. The tip of a 30 gauge needle was inserted in the vein and approximately 200 µl of blood were

collected. In order to expose the portal vein the abdominal viscera was genteelly pulled outside the abdominal cavity while the left as well as the median liver lobes were reflected cranially. The tip of a 30 gauge needle was directed against the direction of the blood flow and approximately 200 µl of blood were slowly collected. In order to collect heart blood a 26 gauge needle was passed through the diaphragm and the tip was inserted in the right heart chamber. All blood samples were collected in a syringe pre-coated with EDTA (50 µl/ml blood) to prevent blood coagulation. Subsequently, the blood was centrifuged in a cool centrifuge for 10 min at 13.000 rpm and plasma was separated and stored at -80° C until analysis.

Following blood collection the whole liver was excised. Samples were collected from defined anatomical positions (figure 2.2) as follow: (1) pieces of approximately 20 mg were collected from the median liver lobe and were snap-frozen in liquid nitrogen and stored at -80° C for later analysis. (2) A piece of 1-2 cm size was collected from the median liver lobe and fixed in 4% paraformaldehyde (PFA) for 48 h at 4° C. Subsequently, the samples were transferred to a solution of 30% glucose and 4% PFA (1:1) and stored at 4° C for later preparation of vibratome slices. (3) A piece from the left liver lobe was mounted with cryomold tissue-tek and rapidly frozen in isopentane. The samples were subsequently stored at -80° C until preparation of cryo sections. (4) A piece of 1-2 cm was collected from the left liver lobe and fixed in 4% PFA for 48 h at 4° C. Subsequently, the samples were washed with PBS and embedded in paraffin using a spin tissue processor STP 120 embedding automate (Microm, walldorf, Germany). The used embedding program is shown in table 2.1. In order to further prepare the samples for cutting, solid paraffin blocks were made using EC 350-modular tissue embedding center (Microm, walldorf, Germany).

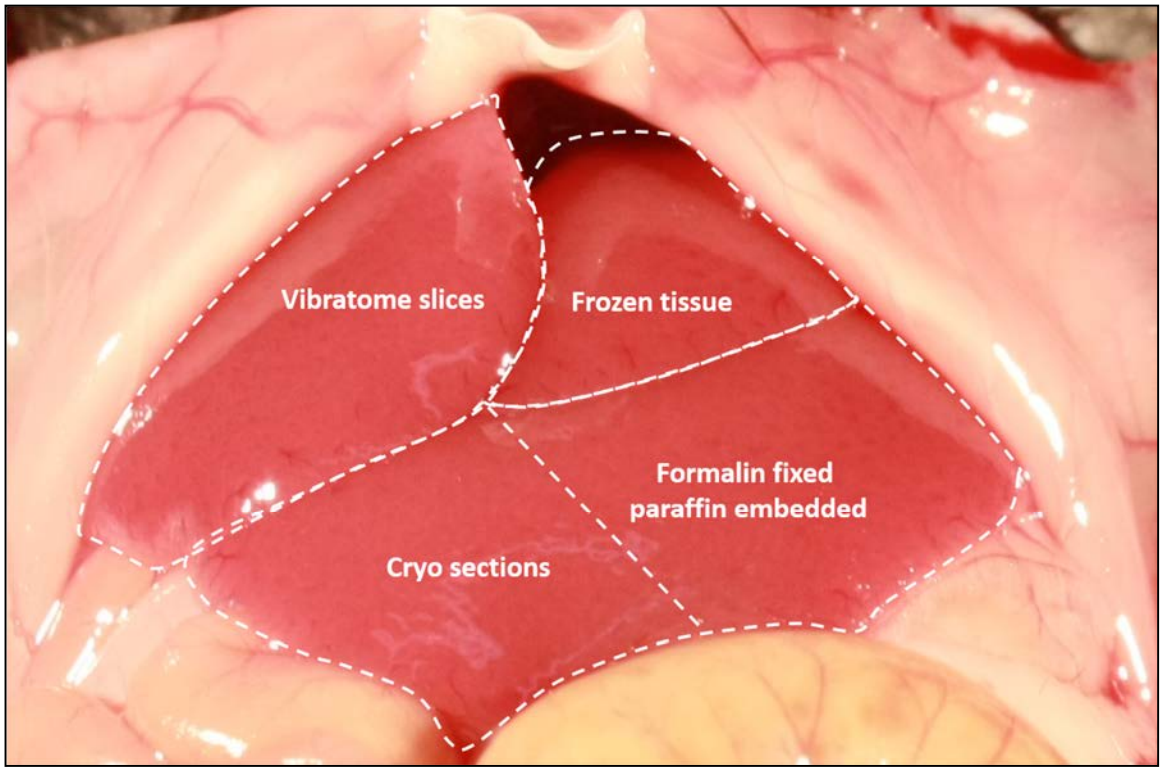

Figure 2. 2: Sites of samples collection from the liver lobes. A piece from the median liver lobe was used for preparation of vibratome slices. Another piece from the median lobe was snap frozen and stored at -80° C until used for glutathione analysis. The left liver lobe was divided into two pieces; one was used for preparation of cryo section and the other was used for preparation of paraffin sections.

Table 2. 1: Embedding program of the mouse liver tissue

Step	Treatment	Time (min)
1	70% Ethanol	30
2	70% Ethanol	60
3	90% Ethanol	30
4	90% Ethanol	30
5	99% Ethanol	30
6	99% Ethanol	35
7	99% Ethanol	60
8	Xylol	30
9	Xylol	35
10	Xylol	60
11	Paraffin histowax	80
12	Paraffin histowax	105

2.2.4 Transaminases assay

2.2.4.1 Alanine transaminase assay

Alanine transaminase (ALT) was measured colorimetrically in plasma separated from heart blood using a commercially available kit according to the manufacturer's instructions (Sigma-Aldrich Corp., St. Louis, MO, USA). ALT catalyzes the reversible transfer of an amino group from alanine to alpha-ketoglutarate producing pyruvate and glutamate. Pyruvate was detected in an enzymatic reaction that converts a colorless probe into a color that can be detected at 570 nm wavelength with the aid of a microplate reader. The intensity of color development was proportional to ALT activity. Utilizing a pyruvate standard curve (figure 2.3) the activity of ALT was calculated. To avoid false positive results a blank sample in which the substrates were omitted was run in parallel with the test samples. Subsequently, the background was corrected by subtracting the blank value from the test value.

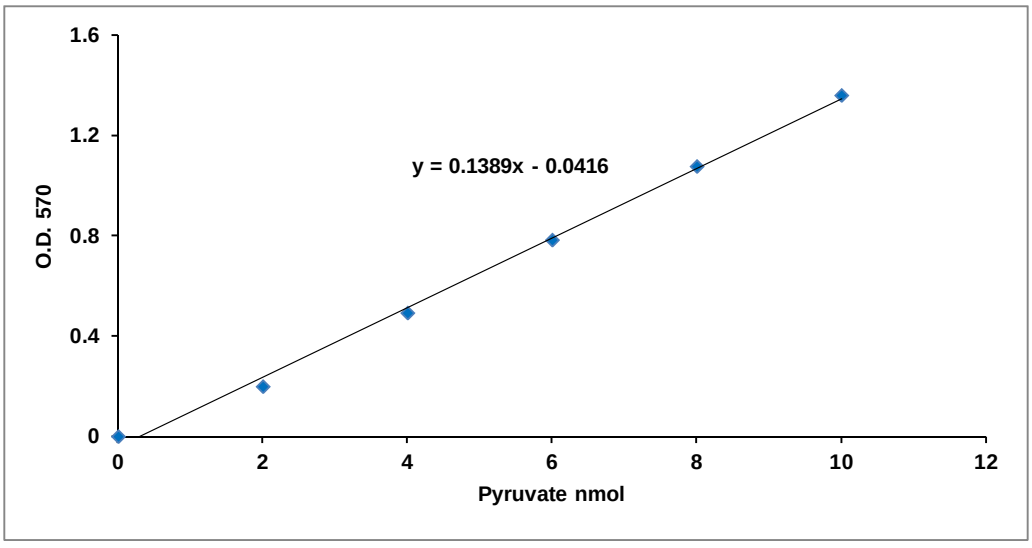

Figure 2. 3: Pyruvate standard curve which was used to measure the activity of alanine transaminase (ALT). ALT transfers an amino group from alanine to alpha-ketoglutarate producing pyruvate and glutamate. The concentration of pyruvate was measured colorimetrically at 570 nm wavelength using a microplate reader.

2.2.4.2 Aspartate transaminase assay

Aspartate transaminase (AST) was measured in plasma separated from heart blood in a colorimetric reaction using a commercially available kit according to the manufacturer's instructions (Sigma-Aldrich Corp., St. Louis, MO, USA). AST catalyzes the conversion of alpha-ketoglutarate plus aspartate to oxaloacetate and glutamate. Glutamate was detected enzymatically in a reaction that converts a colorless probe into a color. The developed color was measured using a microplate reader at 450 nm wavelength. To avoid false positive results, a blank was included in which the substrates were omitted. Subsequently, the results of the blank was subtracted from the test samples. The activity of AST was calculated with the aid of a standard curve (figure 2.4) prepared from glutamate.

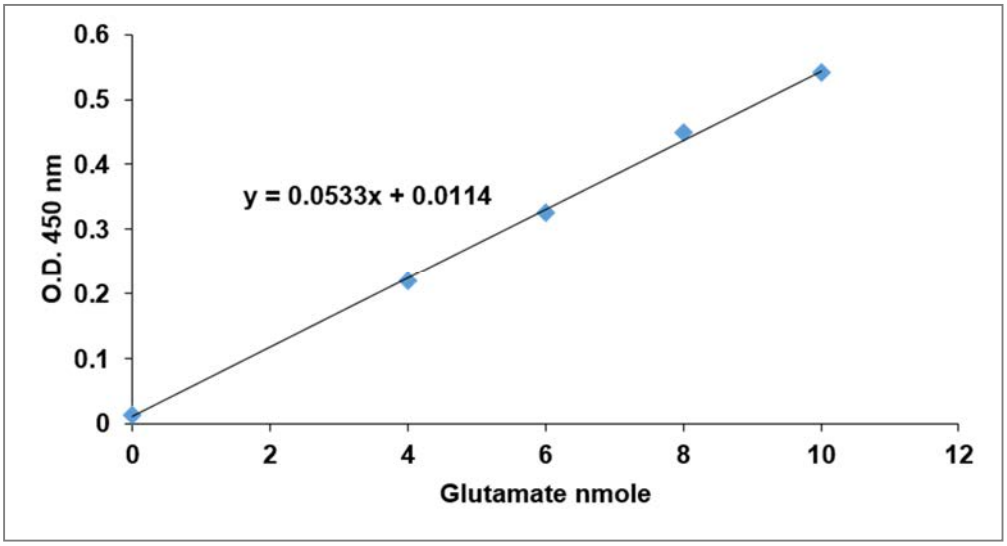

Figure 2. 4: Glutamate standard curve which was used to measure the activity of aspartate transaminase (AST). AST catalyzes the conversion of alpha-ketoglutarate plus aspartate to oxaloacetate and glutamate. The concentration of glutamate was measured in a colorimetric reaction at 450 nm wavelength using a microplate reader.

2.2.5 Histopathology

2.2.5.1 Hematoxylin and eosin staining

Hematoxylin and eosin (H&E) staining was performed in five µm thick tissue sections prepared using a microtome (Microm, Walldorf, Germany). In order to remove paraffin the sections were warmed up at 56-60° C for 30 min and then at 65-70° C until melting of paraffin. This was followed by incubation three times, 5 min each, in xylene. The sections were then rehydrated by incubation in a descending ethanol gradient (98%, 95%, 90%, 80% and 70%) for 5 min each. After washing for 5 min in distilled water the sections were incubated for 5 min in Mayer's hematoxylin (1:5) (Merk, Darmstadt, Germany). The excess hematoxylin was removed by washing under running tap water for 15 min. Subsequently, incubation in eosin (1%) was done for 3 min followed by a breif rinsing in distilled water. Afterward, the sections were dehydrated by incubation in an ascending ethanol series (70%, 80% and 90%) for 5 seconds each and then two-times in absolute ethanol 5 min each. Subsequently, the sections were incubated for 3 min in xylene and then mounted with entellan for preservation. Images were acquired with a brightfield microscope using Cell F software (Olympus, Hamburg, Germany).

2.2.5.2 Picrosirius red staining

In order to visualize collagen deposition in fibrosis picrosirius red staining was performed using a commercially available kit according to the manufacturer's instructions (Polyscience Europe GmbH, Eppelheim, Germany). The staining was performed in five µm thick paraffin embedded tissue sections. The sections were incubated in xylene two-times 5 min each. After deparaffinization, the sections were rehydrated in 100% and 95% ethanol 5 min each then in 70% and 50% ethanol 2 min each. Afterward, the tissue sections were rinsed breifly in distilled water for 2 min. Subsequently, the sections were immersed in solution A (phosphomolybdic acid) for 2 min followed by rinsing shortly in distilled water for 90 seconds. Afterward, the sections were immersed in solution B (picrosirius red

F3BA) for 1 hour followed by washing in distilled water for 2 min. Subsequently, the sections were placed in solution C (0.01% HCl) for 2 min. Afterward, the sections were dehydrated in a graded ethanol series (70%, 95% and 100%), 2 min each and then incubated in Roti-histol for 3 min. Finally, the sections were preserved by mounting with entellan. Images were acquired with a brightfield microscope using Cell F software (Olympus, Hamburg, Germany).

2.2.6 Glutathione assay

GSH and GSSG were measured based on the method of New and Chan 2008. GSH was derivatized with N-ethylmaleimide (NEM) to prevent oxidation of the sulfhydryl group and GSSG remained unchanged. For the GSH two isomers are formed. A buffered NEM solution was added immediately to the weighed liver sample. After homogenization the protein was precipitated by trichloroacetic acid. Lipophilic compounds were extracted by dichloromethane. The GSH-NEM derivatives and GSSG fraction was evaporated to dryness under a stream of nitrogen. The residue was reconstituted in water and then analyzed by LC-MS/MS. The analytes were separated on a PolarTec (125 x 3 mm, 3µm) column with a corresponding precolumn at 30 °C. The mobile phase was formed of formic acid in water (0.1 %) and formic acid in acetonitrile / water (0.1 %; 80 %/ 20 %) and was applied as gradient with a flow rate of 0.2 mL/min. The retention times were for GSSG 8.9 min and for the two GSH-NEM isomers 11.8 and 13.6 min. The detection was operated in the multiple reaction monitoring (MRM) mode with 433 -> 304 (quantifier) and 433 -> 201 (qualifier) for the GSH-NEM derivatives and 613 -> 355 (quantifier) and 613 -> 484 (qualifier) for the GSSG. The signals of the two GSH derivatives were added for the quantification.

2.2.7 Measurement of acetaminophen and its metabolites

Acetaminophen and its metabolites were measured in blood plasma collected from the portal vein, the liver vein as well as the mixed venous blood in the right heart chamber. The analysis was done using LC-MS/MS technique in cooperation with Dr. Martin Vonbergen, proteomics department, Helmholtz Centre For Environmental Research, Leipzig, Germany.

2.2.8 Immunohistochemistry

2.2.8.1 Immunoperoxidase staining

Immunoperoxidase staining was performed on five µm thick paraffin or frozen tissue sections. In order to prepare the paraffin sections for staining, deparaffinization and rehydration steps were done as described above. Subsequently, antigen retreival was performed by boiling three times, 5 min each, in either citrate (pH 6.0) or tris/EDTA (pH 9.0) buffer according to the type of antibody (table 2.2). The sections were allowed to cool down for 30 min and then washed in distilled water for 5 min before proceeding to the next step. Subsequently, the endogenous peroxidases were blocked by immersion of the sections in 0.3% hydrogen peroxide in methanol for 15 min. Afterward, the sections were washed briefly in distilled water and then two times, 10 min each, in TBS.

In order to prepare the frozen liver tissue for staining, five µm thick sections were performed using a Leica CM 3050s-cryostate (Leica Microsystems, Wetzlar, Germany). The sections were fixed in 3% PFA for 5 min at 4° C followed by washing in PBS for 5 min. Subsequantly, the sections were incubated in an ascending methanol series (50%, 70% and 90% for 1 min each). To avoid the possible interference of endogenous peroxidases, the sections were immersed in 0.3% hydrogen peroxide in methanol for 15 min. Subsequently, the sections were incubated in a descending methanol series (90%, 70% and 50% for 1 min each) and then washed in PBS for 5 min.

Afterward, the paraffin as well as th cryo sections were processed in the same way. In order to avoid the non-specific bindings of the antibodies, the sections were incubated in BSA/PBS solution for 2 h. Furthermore, the endogenous avidin and biotin were blocked using a commercially avilable kit according to the manufacturer's instructions (Vector laboratories, Burlingame, USA). Subsequently, the sections were incubated overnight with the primary antibody (table 2.2) in a humid chamber at 4° C. Subsequently, the sections were washed in TBST three times, 5 min each. The sections were further incubated in BSA/PBS solution for 2 h. Subsequently, the sections were incubated with an apropriate seconday antibody (table 2.2) for 2 h in a humid chamber at room teprature followed by washing in TBST for three times 5 min each. In case of using un conjugated secondary antibodies, the tissue sections were further incubated with streptavidine HRP for 1 h in a humid chamber at room teprature followed by washing three times in TBST 5 min each. Finally, the antibodies binding were visualized by incubation in either DAB or AEC substrate. In case of using DAB substrate, the sections were pre-immersed in tris-HCL solution for 5 min and then stained with DAB solution for 4-7 min according to the color development. In case of using AEC substrate, the sections were placed in citrate buffer for 5 min and then stained with AEC for 5-10 min according to the color development. Subsequently, the sections were washed in TBS for 2 min. In order to visualize the nucleus, a counter staining with Mayer's hematoxylin was done for 1 min followed by washing under running tap water for 10 min. The AEC stained sections were then preserved by mounting with an aqueous mounting media. The DAB stained sections were dehydrated by incubation in an ascending ethanol series (70%, 90%, 95% and 100%, for 30 seconds each). Furthermore, the sections were washed in rotihistol for 4 min. The sections were then preserved by mounting with entellan. Images from the stained sections were acquired with a fluorescence microscope BX41 using Cell F software (Olympus, Hamburg, Germany).

Table 2. 2: Used antibodies and staining conditions

Target	Tissue section	Retreival reagent	Primary antibody		Secondary antibody	
			Antibody	Concentation	Antibody	Concentration
B-cell	FFPE	Citrate	Rat anti-B220	1:1000	rabbit anti-rat IgG	1:1000
Proliferation	FFPE	Citrate	Rat anti-BrdU	1:25	rabbit anti-rat IgG	1:1000
T-cell	Frozen	-	Rabbit anti-CD3	1:50	HRP anti rabbit (envision rabbit kit)	
Leukocytes	FFPE	Citrate	Rat anti-CD45	1:400	rabbit anti-rat IgG	1:1000
CYP2E1	Frozen	-	Rabbit anti-CYP2E1	1:250	Swine anti-rabbit	1:20
HSCs	FFPE	Citrate	Rabbit anti-desmin	1:400	Swine anti-rabbit	1:20
HSCs	Frozen	-	Rabbit anti-desmin	1:400	donkey anti-rabbit Cy3	1:100
Macrophage	FFPE	Citrate	Rat anti-F4/80	1:50	rabbit anti-rat IgG	1:1000
Neutrophils	FFPE	Citrate	Rat anti-LY6G	1:5000	rabbit anti-rat IgG	1:1000

Activated HSCs	FFPE	Tris/EDTA	Mouse anti human α-SMA (Dako)	1:100	HRP anti mouse (envision mouse kit)	
Activated HSCs	FFPE	Citrate	Mouse anti α-SMA (Abcam)	1:50	MaxFluor 488 (mouse on mouse kit)	1:100
Activated HSCs	FFPE	Citrate	Rabbit anti α-SMA (Abcam)	1:50	donkey anti-rabbit Cy3	1:100

2.2.8.2 Immunofluorescence staining : co-staining of α-SMA and desmin

In order to visualize the acivated and quiescent HSCs, immunofluorescence staining was performed in formalin fixed paraffin embedded (FFPE) tissue sections using antibodies against α-SMA and desmin. The deparaffinization, the rehydration as well as the antigen retrieval steps were performed as described above. Since the used anti-α-SMA antibody was raised in mouse, a mouse on mouse kit (MaxVision Biosciences, Dianova, Hamburg, Germany) was used according to the manufacturer's instructions to avoid non-specific bindings. Breifly, the sections were incubated with a protein blocking solution for 10 min to prevent the non-specific background. Subsequently, a blocking reagent was applied for 1 h in order to bind the endogenous immunoglobulins. After a brief rinsing in PBS, the sections were incubated overnight with mouse monoclonal anti-α-SMA antibody, 1:50 (Abcam, Cambridge, UK) (table 2.2) in a humid chamber at 4° C. The sections were then washed three times in PBS for 2 min each. Subsequantly, the sections were incubated with a secondary antibody conjugated to MaxFlour 488 (MaxVision Biosciences, Dianova, Hamburg, Germany) for 1 h in a dark humid chamber followed by three times washing in PBS.

Before proceeding to the next step, the sections were incubated for 1 h in 3% BSA, 3% tween 80 in PBS in order to block the non-specific bindings. Subsequently, the sections were incubated with anti-desmin antibody, 1:400 (Thermo Scientific, Braunschweig, Germany) in a humid chamber overnight at 4° C. After washing three times in PBS, a secondary antibody was added: Cy3 affinipure F(ab)2 fragment donkey anti-rabbit IgG (H+L), 1:100 for 2 h in a dark humid chamber at room temprature. In order to remove the excess antibody, the sections were washed three times, 5 min each, in PBS. Subsequently, nuclear visualization was done by counter staining with DAPI for 4-5 min followed by rinsing three times, 5 min each, in PBS and washing in distilled water for 10 min. Finally, the slides were mounted with anti-fading mounting media. The staining was visualized by using a confocal laser scanning microscope (Olympus BX61 microscope, Hamburg, Germany) using Olympus Fluoview version 4.0 b software.

2.2.8.3 Co-staining of liver macrophages and activated stellate cells

Co-staining of liver micro-architecture and macrohages as well as activated HSCs was done in 75 µm thick liver slices prepared using a vibratome (Leica Microsystems, Wetzlar, Germany). The prepared slices were placed in 24 well plates and washed for three times, 10 min each, in PBS. Subsequently, antigen demasking was performed by addition of 2 ml citrate buffer and cooking for 11 min in a steam cooker. After washing three times in PBS, the slices were immersed in a blocking serum (3% BSA, 3% tween 80 in PBS) for 2 h at room temperature on a shaker. Afterward, the slices were incubated with the primary antibodies: rabbit anti-α-SMA (1:100, Abcam, Cambridge, UK) and rat anti-F4/80 (1:25, AbD Serotec, Bio-Rad, Puchheim, Germany). The incubation was done at 4° C overnight with shaking. Subsequently, the excess antibodies were removed by washing three times, 10 min each, in PBS with shaking. The slices were then further immersed in the blocking serum (3% BSA, 3% tween 80 in PBS) for 1 h at room temperature on a shaker. Subsequently, the slices were incubated with the secondary antibodies: alexa fluor 647 affinipure F(ab)2 fragment donkey anti-rat

IgG (H+L) (1:50, Dianova, Hamburg, Germany), and Cy3 affinipure F(ab)2 fragment donkey anti-rabbit IgG (H+L) (1:100, Dianova, Hamburg, Germany); the incubation was done for overnight at 4° C on a shaker. Following washing steps, the slices were again incubated with the blocking serum for 2 h at room temperature with shaking. Subsequently, the tissue slices were incubated with goat anti-mouse DPPIV/CD26 ectodomain (1:100, R&D system, Minneapolis, MN, USA) for overnight at 4° C with shaking. Afterward, the slices were then washed three times, 10 min each, in PBS with shaking. The slices were then incubated with donkey F(ab)2 anti-goat IgG (H+L)-alexa fluor 488 antibody (1:100, Dianova, Hamburg, Germany) overnight at 4° C with shaking. After washing three times in PBS, the slices were counter stained with DAPI for 90 min in order to visualize the nucleus. Subsequently, the slices were washed three times, 10 min each, on PBS and one time for 10 min in distilled water. Finally, the slices were mounted on microscopic slides using fluor-preserve reagent and allowed to dry in dark. Images were acquired using a confocal microscope.

2.2.9 TUNEL staining

2.2.9.1 Colorimetric TUNEL staining

In order to visualize DNA breaks and cell death, TUNEL staining was performed using a commercially available kit according to the manufacturer's instructions (Promega, Mannheim, Germany). The staining was done in five µm FFPE tissue sections. Following deparaffinization and rehydration, the sections were immersed in 4% PFA for 15 min and then washed twice in PBS for 5 min. Subsequently, the tissue was permeabilized by covering with proteinase K solution (20 µg/ml) for 10 min at room temperature. After washing in PBS for 5 min, samples fixation was repeated by immersion in 4% PFA for 5 min. The sections were washed twice in PBS, 5 min each, and then covered with equilibration buffer for 8 min at room temperature. Subsequently, the sections were incubated with TdT reaction mix (equilibration buffer 98 µl, biotinylated nucleotide mix 1 µl and rTdT enzyme 1 µl

for each individual section) and covered with a plastic cover slips for 1 h at 37° C in a humid chamber. The reaction was stopped by washing in 2X SSC buffer for 15 min. Subsequently, the sections were immersed three times, 5 min each, in 0.5% BSA, 0.1 triton X-100 in PBS on a shaker followed by washing in PBS for 5 min. The endogenous peroxidases were blocked by immersion in 0.3% hydrogen peroxide for 3-5 min. After washing three times in PBS. The sections were incubated with streptavidin HRP (1:500) for 30 min at room temperature in a humid chamber followed by washing three times in PBS. TUNEL positive signal was visualized by covering the sections with DAB solution for 3-5 min followed by washing in distilled water for 5 min. Subsequently, the sections were immersed in Mayer's hematoxylin for 60-90 seconds. The excess hematoxylin was removed by washing under running tap water for 10 min. Finally, the tissue sections were dehydrated and preserved by mounting with entellan. Images were acquired with a brightfield microscope using Cell F software (Olympus, Hamburg, Germany).

2.2.9.2 Combined staining of TUNEL, α-SMA and F4/80

Co-staining of TUNEL, α-SMA and F4/80 was done in four µm FFPE tissue sections. Initially, the sections were stained with TUNEL as described above with three exceptions: (1) a fluorometric TUNEL kit was used (Promega, Mannheim, Germany), (2) the permeabilization step using proteinase K was omitted as it interfere with the follow up staining, and (3) the 4% PFA should be methanol free. As a positive control for DNA fragmentation, DNase I was added to an APAP treated liver tissue sections on day three directly before adding equilibration buffer according to the manufacturer's instructions (Promega, Mannheim, Germany) and processed in the same way as the test tissue sections. After TUNEL staining the sections were further prepared for immunostaining. First, antigen retrieval was done by immersion in citrate buffer for 15 min in a water bath at 70° C. The tissue sections were allowed to cool down for 20 min and then washed 3 times in PBS. To avoid non-specific staining, the tissue sections were incubated with 3% BSA, 3% tween 80 in PBS for 1 h at room temperature in a humid chamber.

Subsequently, the sections were incubated with the primary antibodies: rabbit anti-α-SMA (1:50, Abcam, Cambridge, UK) and rat anti-F4/80 (1:25, AbD Serotec, Bio-Rad, Puchheim, Germany), overnight at 4 C° in a humid chamber. After washing in PBS, the sections were immersed in a blocking serum (5% donkey serum, 3% tween 80 in PBS) for 1 h at room temperature. Subsequently, the tissue sections were incubated with the secondary antibodies: alexa fluor 647 affinipure F(ab)2 fragment donkey anti-rat IgG (H+L) (1:100, Dianova, Hamburg, Germany) and Cy3 affinipure F(ab)2 fragment donkey anti-rabbit IgG (H+L) (1:100, Dianova, Hamburg, Germany) for 1 h at room temperature in a humid chamber. After washing in PBS, counter staining with DAPI was performed followed by washing three times in PBS and one time in distilled water for 10 min. The tissue sections were preserved by mounting with fluor-preserve reagent. The staining was visualized by a confocal laser scanning microscope (Olympus BX61 microscope, Hamburg, Germany) using Olympus Fluoview version 4.0 b software.

2.2.9.3 Combined staining of TUNEL and desmin

Combination of TUNEL and desmin was perofrmed in 4 or 30 µm frozen tissue sections as indicated in the results section. First, TUNEL staining was performed using a commercially available fluorometric TUNEL kit (Promega, Mannheim, Germany) according to the manufacturer's instructions with the exception of omitting the permeabilization with proteinase K step. Subsequently, the sections were prepared for desmin immunostaining by immersion in a blocking serum (3% BSA, 3% tween 80) in PBS for 1 h at room temperature. Afterward, the tissue sections were incubated with rabbit anti-desmin antibody (1:400, Thermo Scientific, Braunschweig, Germany) overnight at 4° C in a humid chamber. After washing three times in PBS, the sections were incubated with Cy3 affinipure F(ab)2 fragment donkey anti-rabbit IgG (H+L) (1:100, Dianova, Hamburg, Germany) for 2 h at room temperature in a humid chamber. Subsequently, the tissue sections were washed three times in PBS. In order to visualize the nucleus, counter staining with DAPI was performed followed by washing three times in PBS

and one time in distilled water for 10 min. Finally, the tissue sections were mounted with fluor-preserve reagent and allowed to dry at room temperature. The staining was imaged with a confocal laser scanning microscope.

2.2.10 Intravital imaging

In vivo imaging of intact mice livers was done using a custom modified inverted LSM-MP7 (Zeiss, Jena, Germany) according to the method of Reif et al. (2017). Briefly, at the indicated time period, fluorescently labelled antibodies and fluorescent markers were administered via the tail vein (table 3.2). Subsequently, the mice were anesthetized with an i.p. injection of ketamine (64 mg/kg), xzylazine (7.2 mg/kg) and acepromazine (1.7 mg/kg). In order to expose the liver for intravital imaging, a small window was made below the xiphoid process. After cutting of the falciform ligament, the left liver lobe was exposed by gently pushing of the abdomen and placed on 0.17 mm thick cover slip (Ocon 159, Logitech, Glasgow, UK) and the mouse placed on a lateral position. The exposed liver was then placed at the microscope stage using a custom-made platform and covered with saline soaked gauze. The quality of mouse preparation was controlled by the regular blood flow at the observed region.

Table 2. 3: Fluorescent marker dyes and antibodies used for in vivo imaging.

Marker	Indicated structure	Source	Dose	Application volume
Rhodamine 123	Mitochondrial membrane potential and liver morphology	Thermo Scientific, MA, USA	0.8 mg/kg	20 µl in PBS/methanol
Hoechst 33258	Nuclei	Thermo Scientific, MA, USA	5 mg/kg	20 µl in PBS
PE-labelled CD11b	Infiltrating macrophages	eBioscience, CA, USA	60 µg/kg	100 µl in PBS
PE-labelled NK1.1	NK cells and innate lymphoid cells	eBioscience, CA, USA	60 µg/kg	100 µl in PBS
PE-labelled F4/80	Resident and infiltrating macrophages	eBioscience, CA, USA	60 µg/kg	100 µl in PBS

2.2.11 Flow cytometric analysis of intrahepatic leukocytes

Livers of untreated, APAP plus saline and APAP plus clodronate treated mice were perfused *in vivo* via the portal vein with 10 ml 1x PBS and excised. Homogenization of liver tissue was performed using liver disassociation kit (Miltenyi Biotec, Bergisch Gladbach, Germany) and gentle MACS Octo Dissociator according to the manufacturer's instructions. Digested and minced livers were subsequently passed through a meshed screen and washed in DPBS. After centrifugation, the supernatant was removed and the remaining pellet was resuspended in 36% Percoll solution and subjected to density gradient centrifugation at 1,000 x g for 15 minutes at 20°C. Pelleted leukocyte-solution was washed, subsequently red cells were lysed with Red Cell Lysing Buffer (ACK) for 5 minutes at room temperature. Lysis was neutralized by addition of 1x PBS and centrifuged. After centrifugation, the resulting liver leukocyte-enriched pellet was

resuspended in full medium and counted with tryptan blue in Neubauer chamber hemocytometer. In the next step, cells were Fc-blocked followed by a surface staining 10 minutes at room temperature with the following battery of antibodies (all from BioLegend) raised against: CD45 (1:400), CD11c (1:25), NK1.1 (1:25), CD3 (1:50), CD4 (1:800), CD8 (1:800), CD19 (1:50) including also markers for dead cells (Zombie Dye Red, BioLegend). After debris and doublets are excluded, isolated liver leukocytes were detected as viable (Zombie red negative) CD45-positive cells and further sub-gated where dendritic cells, NK cells, NKT cells, T helper, cytotoxic T as well as B cells can be differentiated. By inclusion of counting beads (123 count eBeads, eBioscences) into the analyzed cell suspension besides percentages of the individual cell fractions also the total numbers of cells were determined. Flow cytometric analysis was performed on a LSR Fortessa (BD) and analyzed with FlowJo (Tree Star).

2.2.12 Statistical analysis

Statistical analysis was done using SPSS software, version 22, with one-way ANOVA pairwise comparisons by Turkey's test. In case of unequal variances, Independent-samples T-test was performed. $P<0.05$ was considered statistically significant.

3. Results

3.1 Acetaminophen-induced liver injury

3.1.1 Factors influencing acetaminophen-induced hepatotoxicity

In order to identify the ideal settings for the follow up experiments some basic parameters had to be tested. The goal of these experiments was to understand modifying factors of acetaminophen (APAP)-induced liver injury. First, the influence of fasting was studied. For this purpose, a single high dose of APAP (450 mg/kg) was injected i.p. to a group of either ad libitum fed or overnight fasted mice. Blood as well as liver tissue samples were collected on day 1 after APAP administration (figure 3.1A). Fasted mice showed marked elevation of transaminase enzymes compared to fed mice (figure 3.1B). In order to visualize APAP-induced hepatic damage, formalin fixed paraffin embedded liver tissue sections were stained with hematoxylin and eosin (H&E). Microscopically, pericentral liver damage was observed in the fasted mice, whereas individual sporadic dead hepatocytes were detected in the pericentral compartment of the liver lobule of the fed mice (figure 3.1C). Together, these data show that fasted mice are more sensitive to APAP-induced liver injury.

In order to find the reasons why fasted mice are more sensitive to APAP, liver tissue sections were immunostained using antibodies against CYP2E1, the main enzyme catalyzes the metabolic activation of APAP to the toxic metabolite N-acetyl-p-benzoquinone imine (NAPQI). In addition, pieces of frozen liver tissues were analyzed for glutathione (GSH) content which is a scavenger for NAPQI. CYP2E1 staining showed no difference between fasted and fed mice (figure 3.2A). In contrast, fasted mice showed decreased levels of both reduced (GSH) as well as oxidized (GSSG) glutathione (figure 3.2B). In conclusion, fasted mice are more sensitive to APAP toxicity perhaps due to depletion of GSH.

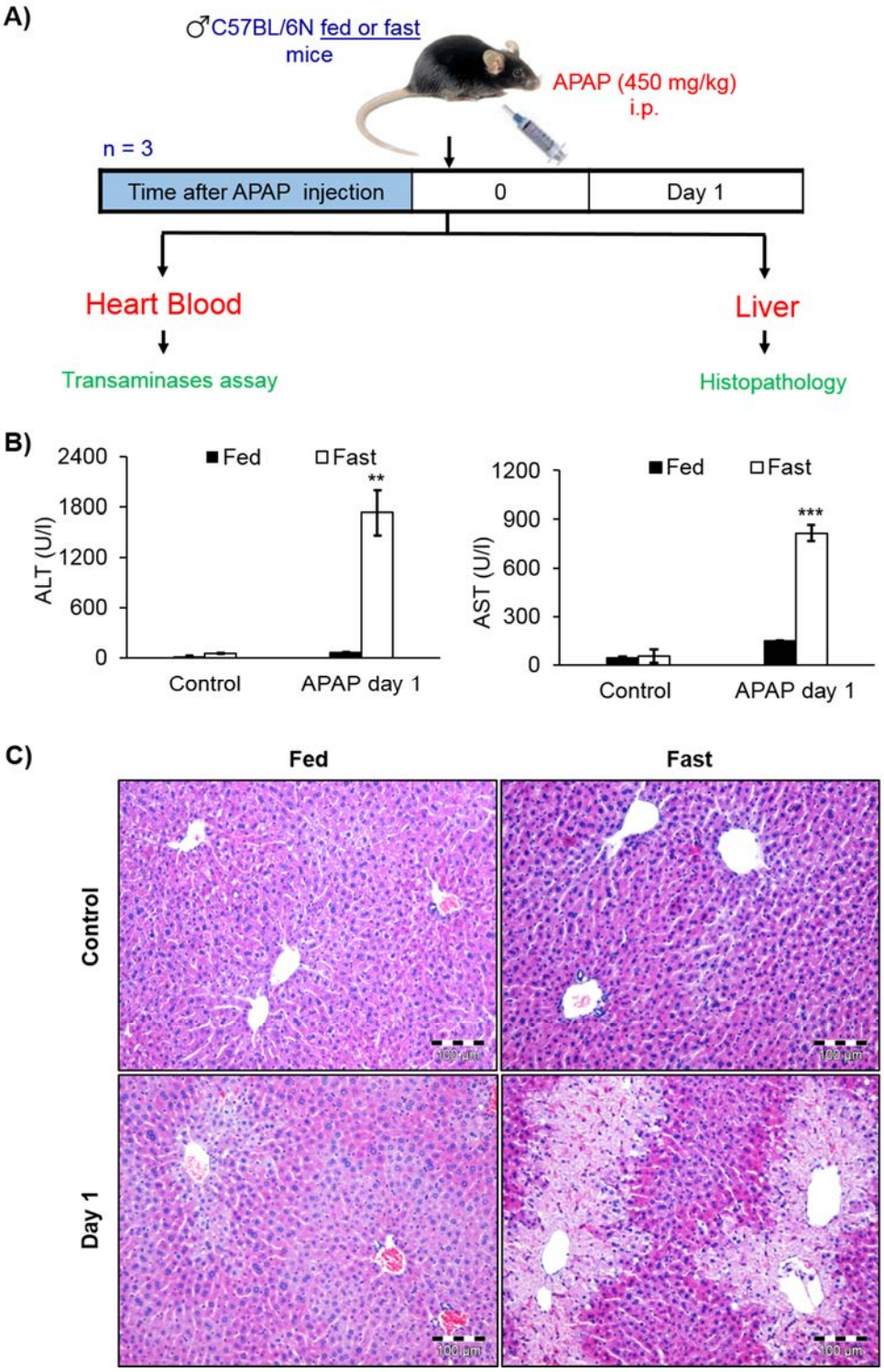

Figure 3. 1: Fasted mice are more sensitive to acetaminophen (APAP) than fed mice. (A) Experimental design: overnight fasted or ad libitum fed mice received a single dose of 450 mg/kg APAP. 24 h later, heart blood as well as liver tissue samples were collected. (B) Higher transaminases [alanine transaminase (ALT) and aspartate transaminase (AST)] activity in fasted compared to fed mice after APAP treatment. (C) Hematoxylin and eosin (H&E) staining showing pericentral liver injury in fasted mice on day one after APAP intoxication. Scale bars: 100 µm. ***p<0.001, **p<0.01 when compared to the fed mice group.

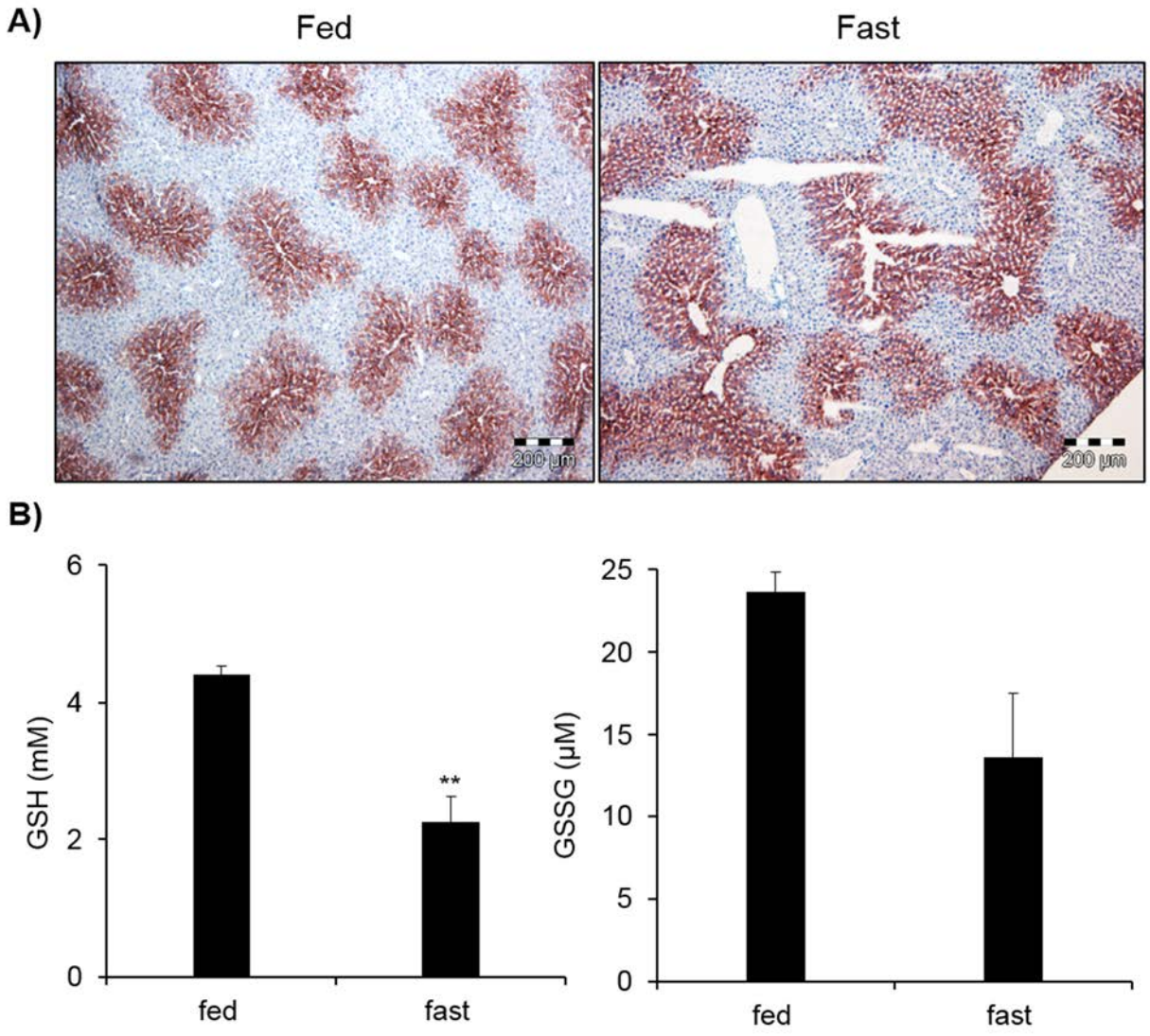

Figure 3. 2: Lower levels of glutathione in the liver tissue of fasted mice. (A) Immunostaining of liver tissue sections using antibodies against CYP2E1 showing normal pericentral zonation of CYP2E1 both in fed as well as fasted mice. Scale bars: 200 µm. (B) Lower levels of reduced (GSH) as well as oxidized (GSSG) glutathione in the liver tissue of fasted mice compared to ad libitum fed mice. **p<0.01 when compared to the fed mice group.

3.1.2 Pharmacokinetics of acetaminophen overdose

In order to get a deeper insights about APAP pharmacokinetics, a kinetic experiment was performed in which a single dose of 450 mg/kg APAP was injected i.p. Blood as well as liver tissue samples were collected as early as 5 min up to 8h after APAP administration (figure 3.3). Blood samples were collected from the portal vein (representing liver inflow), the hepatic vein (representing liver outflow) and from the right heart chamber (representing mixed venous blood) and analyzed for the presence of APAP and its metabolites. The peak blood concentration of APAP was reached within 15 min after administration. This was associated with production of phase II products; glucuronide and sulfate metabolites, as well as glutathione and cysteine adducts (figure 3.4). The peak of metabolite formation occurred between 15 min and 1h after APAP injection. The blood became almost completely free from both APAP and its metabolites at the time between 2 and 4h after APAP administration (figure 3.4).

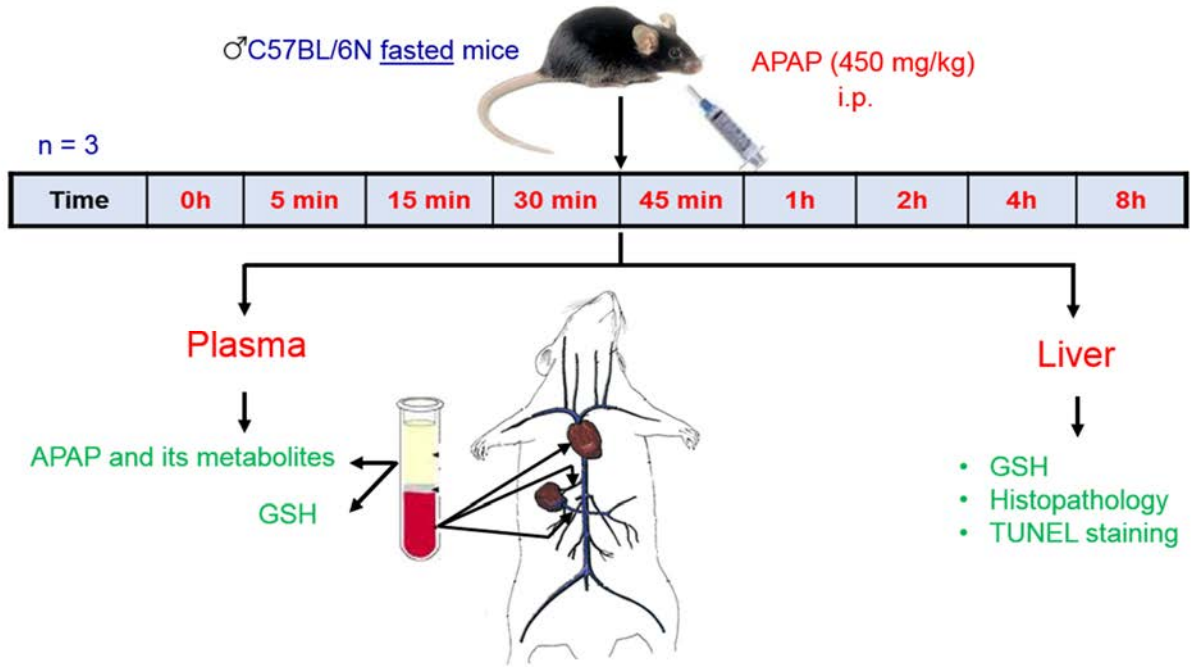

Figure 3. 3: Pharmacokinetics of acetaminophen (APAP). Experimental design: male C57BL/6N mice received a single dose of APAP (450 mg/kg) intraperitoneally. Liver tissue samples as well as blood from the portal vein, the hepatic vein and the right heart chamber were collected in a time dependent manner after APAP administration. Three mice were scarified at each time point.

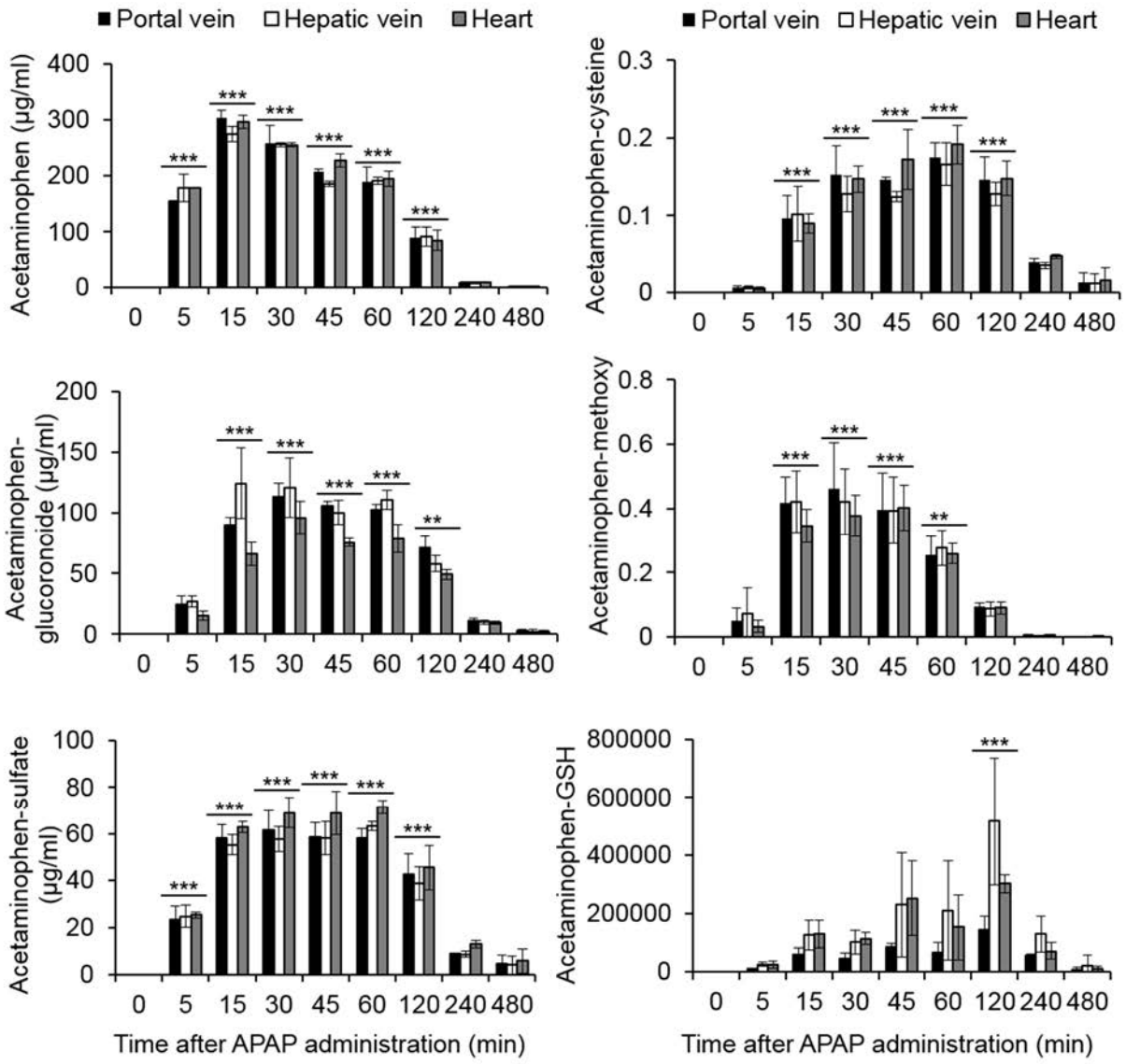

Figure 3. 4: Pharmacokinetics of acetaminophen (APAP). Blood concentrations of APAP and its metabolites in mice at different time intervals after administration of 450 mg/kg APAP. In cases of APAP, APAP glucuronide and APAP sulfate absolute concentrations were calculated, while in cases of glutathione and cysteine adducts a relative quantification was done. Data are means ± SE of three mice per time point. ***p<0.001, **p<0.01 when compared to the control (0) group.

In the next step, the impact of acetaminophen intoxication on GSH levels was studied. For this purpose, GSH concentrations were measured in liver tissue as well as in blood collected from the kinetic experiment (figure 3.3). APAP administration lead to time-dependent depletion of glutathione both in blood as well as in liver tissue (figure 3.5). The

lowest concentrations in the liver tissue were detected at the time between 1 and 4h after APAP injection and started to recover at 8h. In the next step, the influence of formation of the toxic metabolites of APAP and the depletion of glutathione on liver tissue morphology was studied. For this purpose, liver tissue sections were stained with TUNEL, as a marker of DNA breaks, and H&E. TUNEL positive staining was detected on the nuclei of the pericentral hepatocytes between 4 and 8h, especially at the inner pericentral hepatocytes (figure 3.6A). H&E staining showed pericentral liver damage at 4 and 8 h after injection of APAP (figure 3.6B).

In conclusion, these results show that the metabolism of APAP occurs within the first 2h after injection which lead to depletion of glutathione and as a consequence pericentral liver injury develops within 4 till 8h after intoxication.

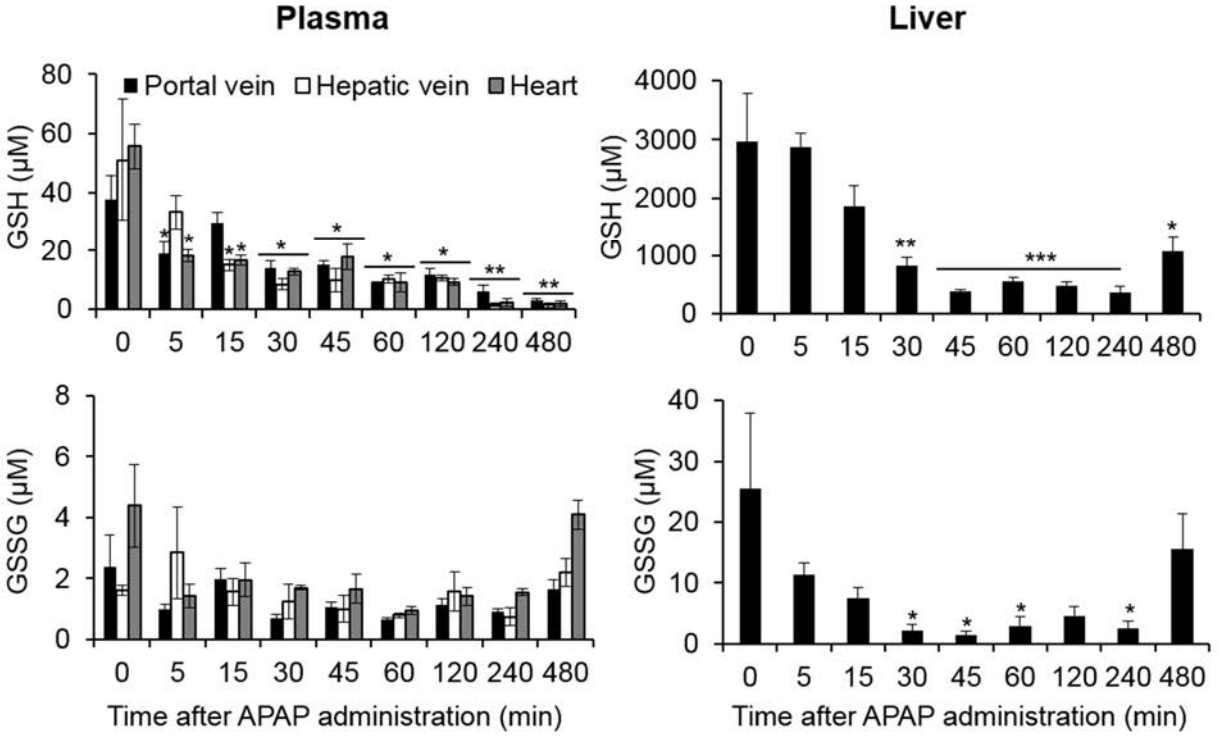

Figure 3. 5: Impact of acetaminophen intoxication on liver and blood glutathione concentrations. Time dependent depletion of GSH and GSSG in liver tissue and blood collected from the portal vein, the hepatic vein and the right heart chamber. Data are means ± SE of three mice per time point. ***p<0.001, **p<0.01, *p<0.05 when compared to the corresponding control (0) group.

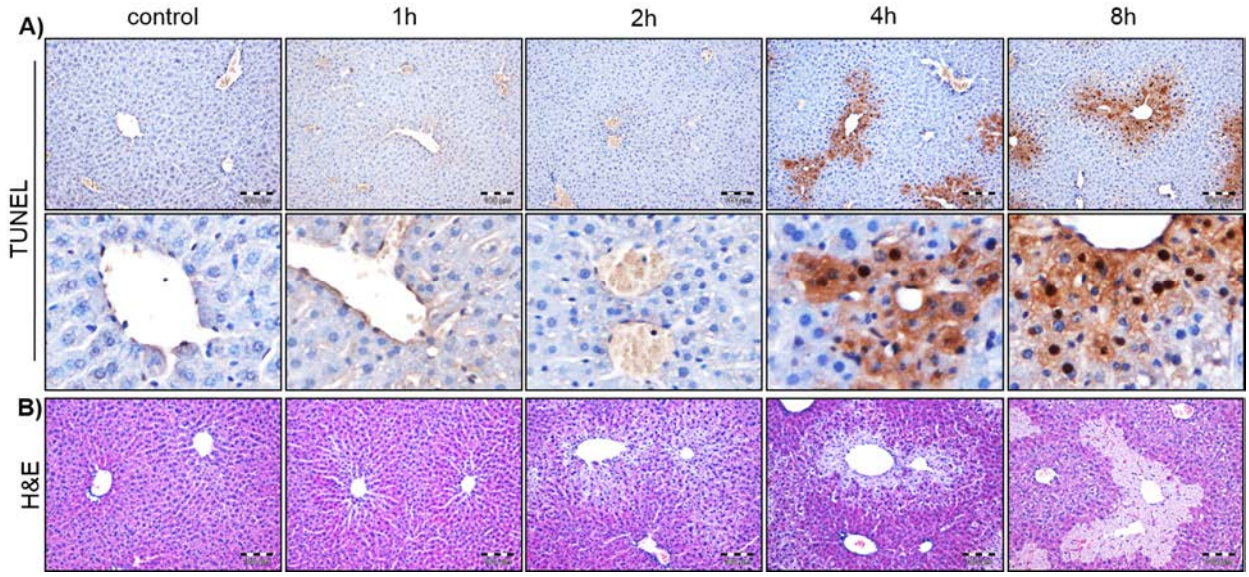

Figure 3. 6: Development of pericentral liver damage after acetaminophen intoxication (450 mg/kg). (A) TUNEL staining showing positive signals in the nuclei of the pericentral hepatocytes at 4 and 8h after injection. (B) H&E staining showing pericentral liver injury at 4 and 8h after APAP administration. Scale bars: 100 µm.

3.1.3 Dose-dependent liver injury after APAP intoxication

In order to find the ideal dose of APAP that can be later used to study liver injury and regeneration, a dose-dependent experiment was performed. For this purpose, various doses of APAP (between 50 and 500 mg/kg) were intraperitoneally injected to overnight fasted mice. 24h later, liver tissue samples were collected and prepared for H&E as well as CYP2E1 staining. Doses up to 89 mg/kg, failed to induce any detectable liver lesion (figure 3.7). In contrast, administration of 158 mg/kg lead to liver injury but only of a central fraction of the CYP2E1 positive area (figure 3.7). Whereas, after administration of 281 mg/kg the entire CYP2E1 positive region of the liver lobule was destroyed. At doses higher than 375 mg/kg not only the CYP2E1 positive area was killed but also a fraction of the CYP2E1 negative region was damaged (figure 3.7). Moreover, severe liver hemorrhage was observed particularly after injection of 500 mg/kg (figure 3.8). In conclusion, doses between 200 and 300 mg/kg are sufficient to kill the pericentral hepatocytes and to study liver injury and regeneration after APAP intoxication.

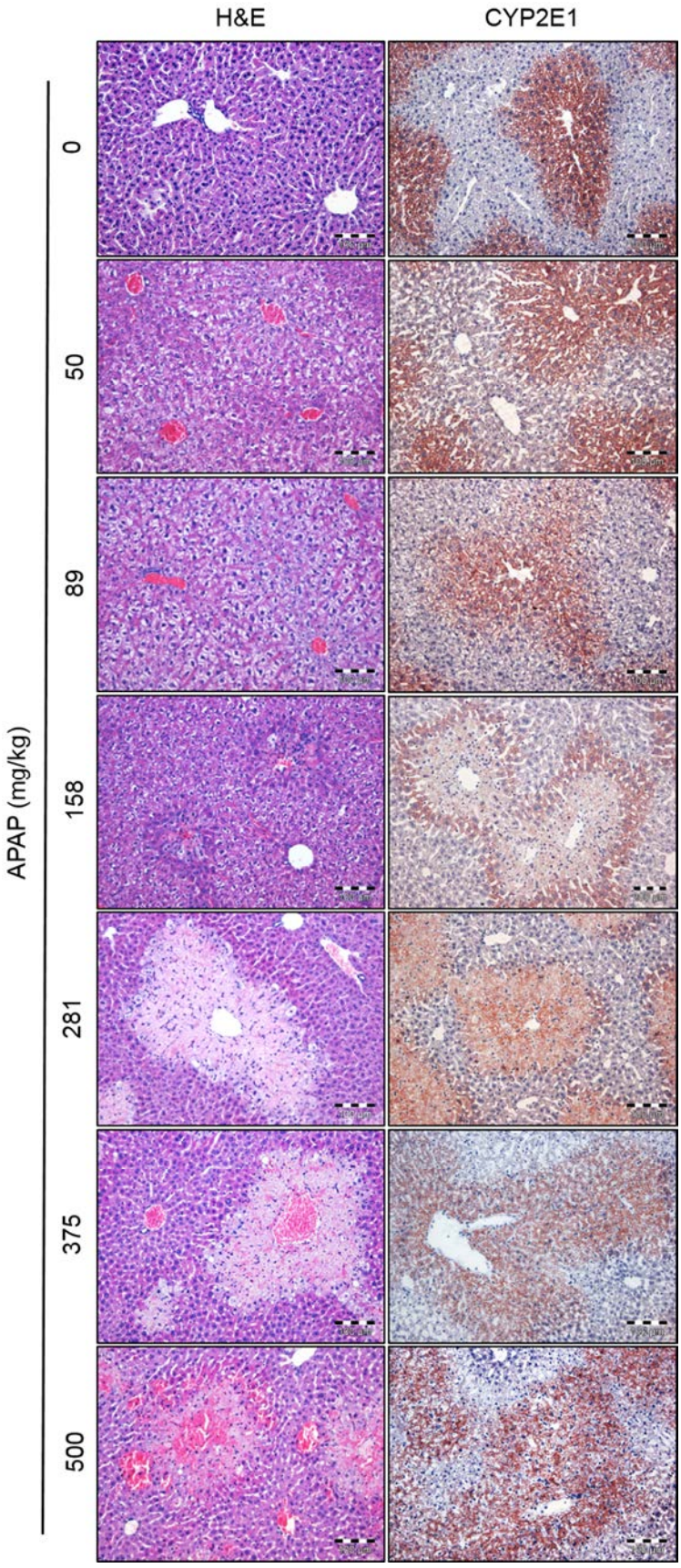

Figure 3. 7: Relationship of CYP2E1 expression and APAP-induced liver injury. H&E staining showing dose dependent centrilobular liver damage. At very high doses (500 mg/kg) severe liver hemorrhage is also visible. CYP2E1 immunostaining showing the typical pericentral zonation of CYP2E1 in control liver. Administration of 158 mg/kg APAP leads to killing of the central fraction of the CYP2E1 positive hepatocytes. Whereas, administration of 281 mg/kg destroys the entire CYP2E1 positive hepatocytes. At higher doses, additionally a fraction of the CYP2E1 negative area is also killed. Scale bars: 100 µm.

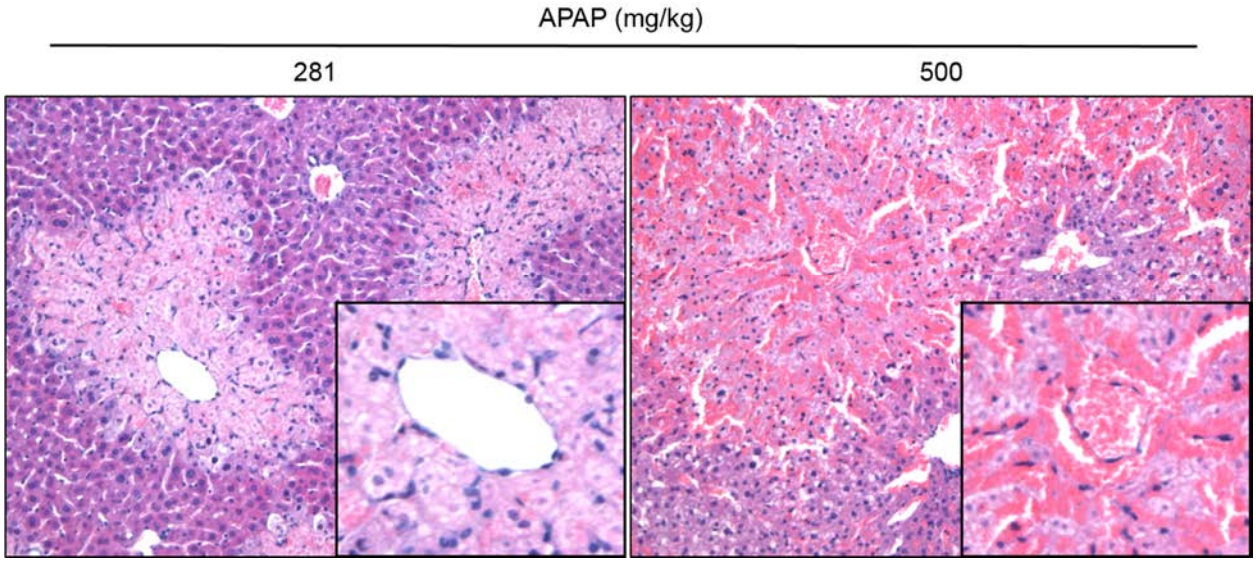

Figure 3. 8: Liver lesion on day 1 after administration of very high doses of APAP. Injection of 281 mg/kg APAP leads to killing of the pericentral hepatocytes. Whereas, administration of higher doses (500 mg/kg) leads to additionally killing of a fraction of the periportal hepatocytes and severe liver hemorrhage. H&E staining, scale bars: 100 µm.

3.1.4 Liver injury and regeneration after acetaminophen intoxication

In order to study liver injury and regeneration after APAP intoxication, a dose of 300 mg/kg was selected. Liver enzymes, histopathology as well as liver cell proliferation were analyzed in a time-resolved manner after APAP administration (figure 3.9A). Macroscopically, white spotted pattern of the liver was obvious as early as 6h after APAP administration and continued until day 2 (figure 3.9B). After day 4, the liver looked similar to controls. Microscopically, by H&E staining a restricted pericentral liver lobule damage was detected at the time between 6h and day 2 after intoxication (figure 3.10A). This was confirmed by elevation of transaminases (ALT and AST) at the same time period (figure 3.10B). After day 4 the liver looked similar to controls and also enzyme activity returned to the basal level (figure 3.10). In the next step, 5-bromo-2'-deoxyuridine (BrdU) staining was performed in order to investigate, whether such efficient regeneration was a result of replacement proliferation of the surviving hepatocytes. For this purpose, a dose of 80 mg/kg BrdU was administered i.p. 1h before liver collection (figure 3.9A). Subsequently, formalin fixed paraffin embedded liver tissue sections were immunostained using antibodies against BrdU. As expected, proliferation in healthy livers was rarely detected. In contrast, two days after APAP administration massive hepatocytes proliferation was visible. The proliferating cells were homogenously distributed in the liver lobule with a slight preference to the border of the dead cell area (figure 3.11). In addition, small size BrdU positive nuclei were detected within the dead cell area which might be for non-parenchymal cells. On day 4, less hepatocyte proliferation was detected, preferentially at the border of the remaining dead cell area (figure 3.11). In conclusion, intoxication with 300 mg/kg APAP leads to pericentral liver injury with a maximum damage on day one. This stimulates replacement proliferation leading to full recovery of the dead cell area within a week after intoxication.

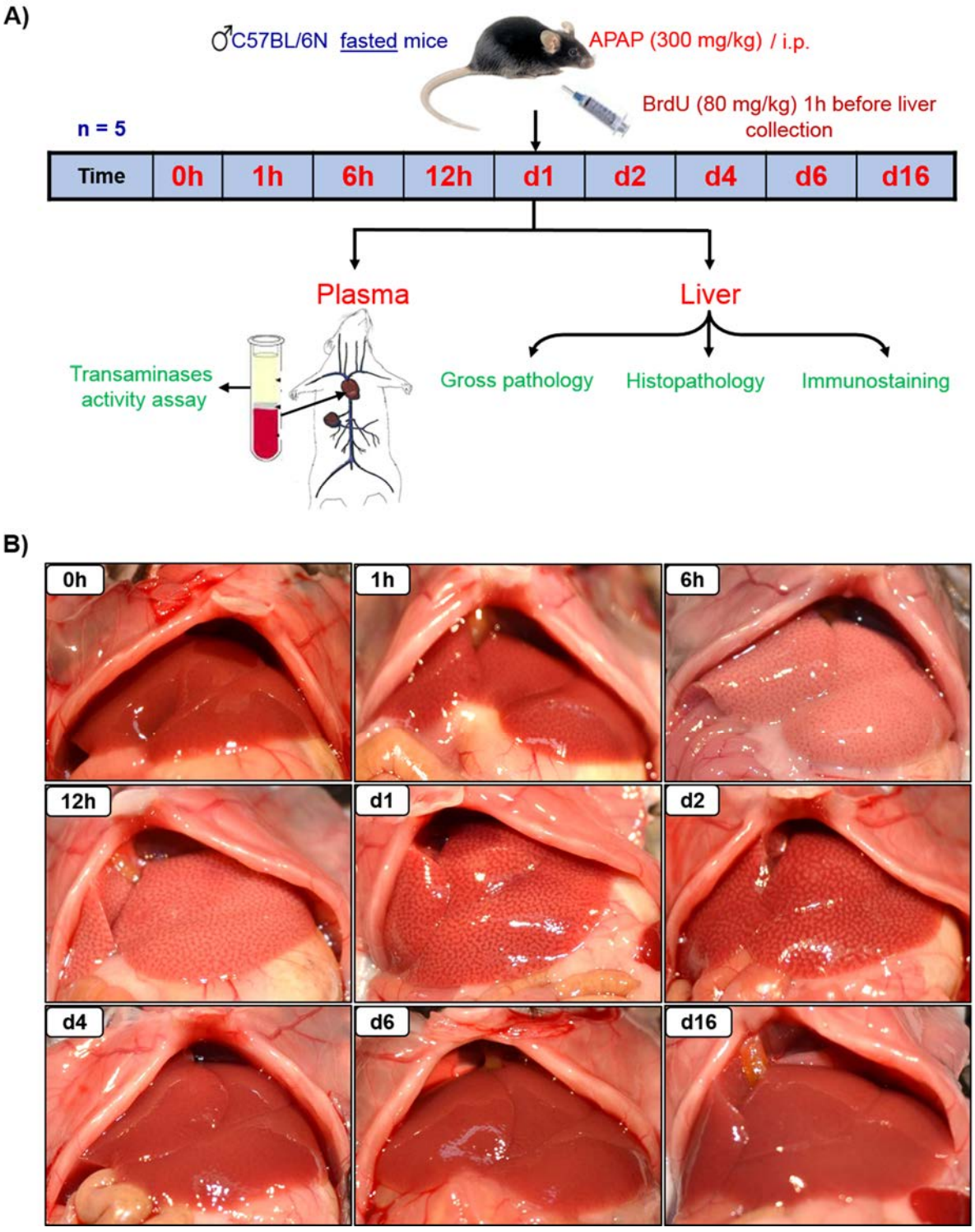

Figure 3. 9: Liver injury and regeneration after APAP intoxication. (A) Experimental design: male C57BL/6N mice were intoxicated with APAP (300 mg/kg i.p) after overnight fasting. Heart blood as well as liver tissue samples were collected in a time-resolved manner after APAP injection. One hour before liver collection the mice received 80 mg/kg BrdU i.p. Five mice were scarified at each time point. (B) Gross appearance of the liver after APAP intoxication. The liver shows white spotted pattern at the time between 6h and day 2 after APAP injection. After day 4 the liver looks similar to controls.

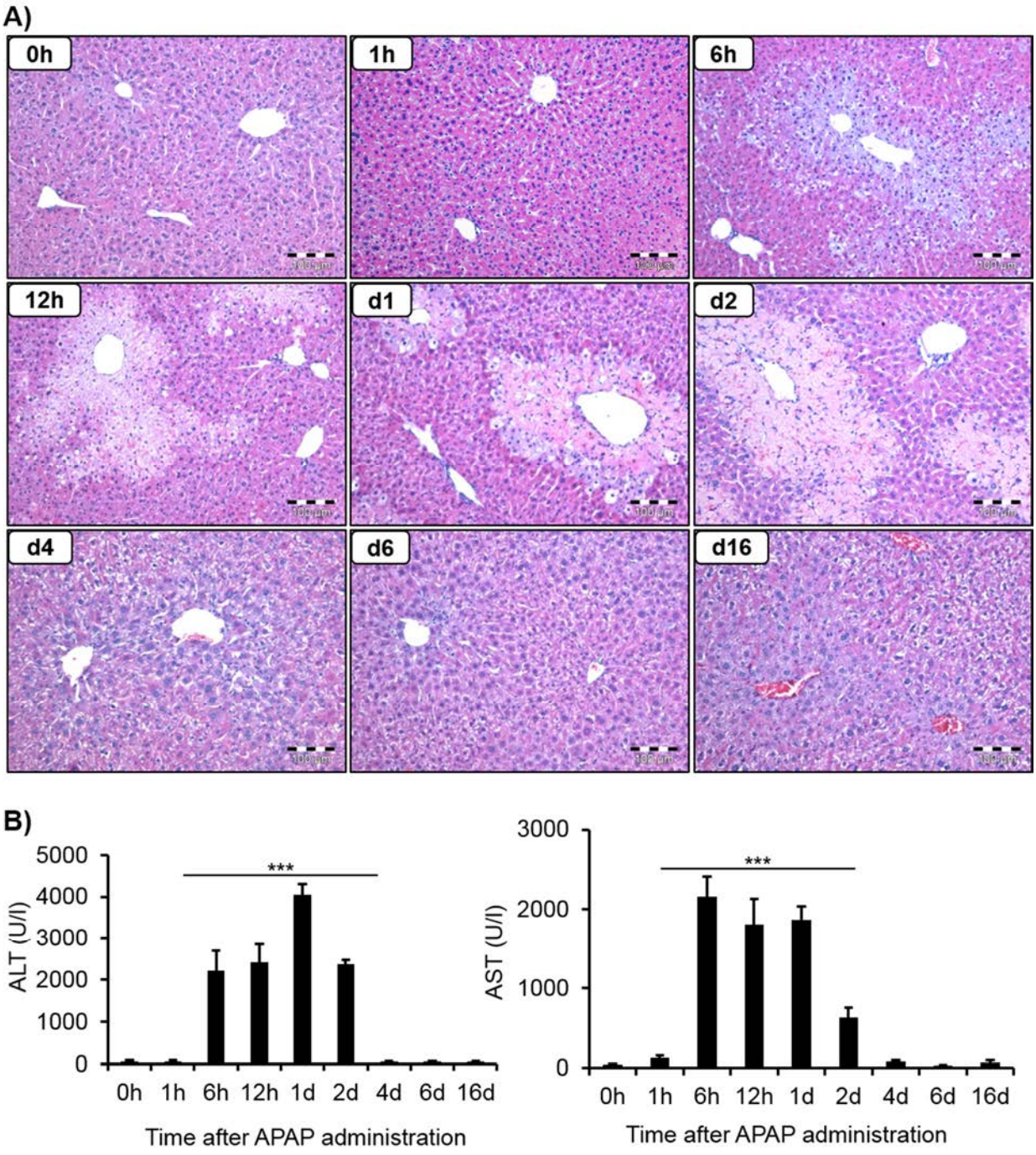

Figure 3. 10: Liver injury and regeneration after APAP intoxication. (A) H&E staining showing pericentral liver lobule damage at the time between 6h and day 2 after APAP administration. Scale bars: 100 µm. (B) Marked elevation of alanine (ALT) and aspartate (AST) transaminases activity, at the time between 6h and day 2 after APAP administration. The data are means ± SE of five mice. ***p<0.001 when compared to the control (0h) group.

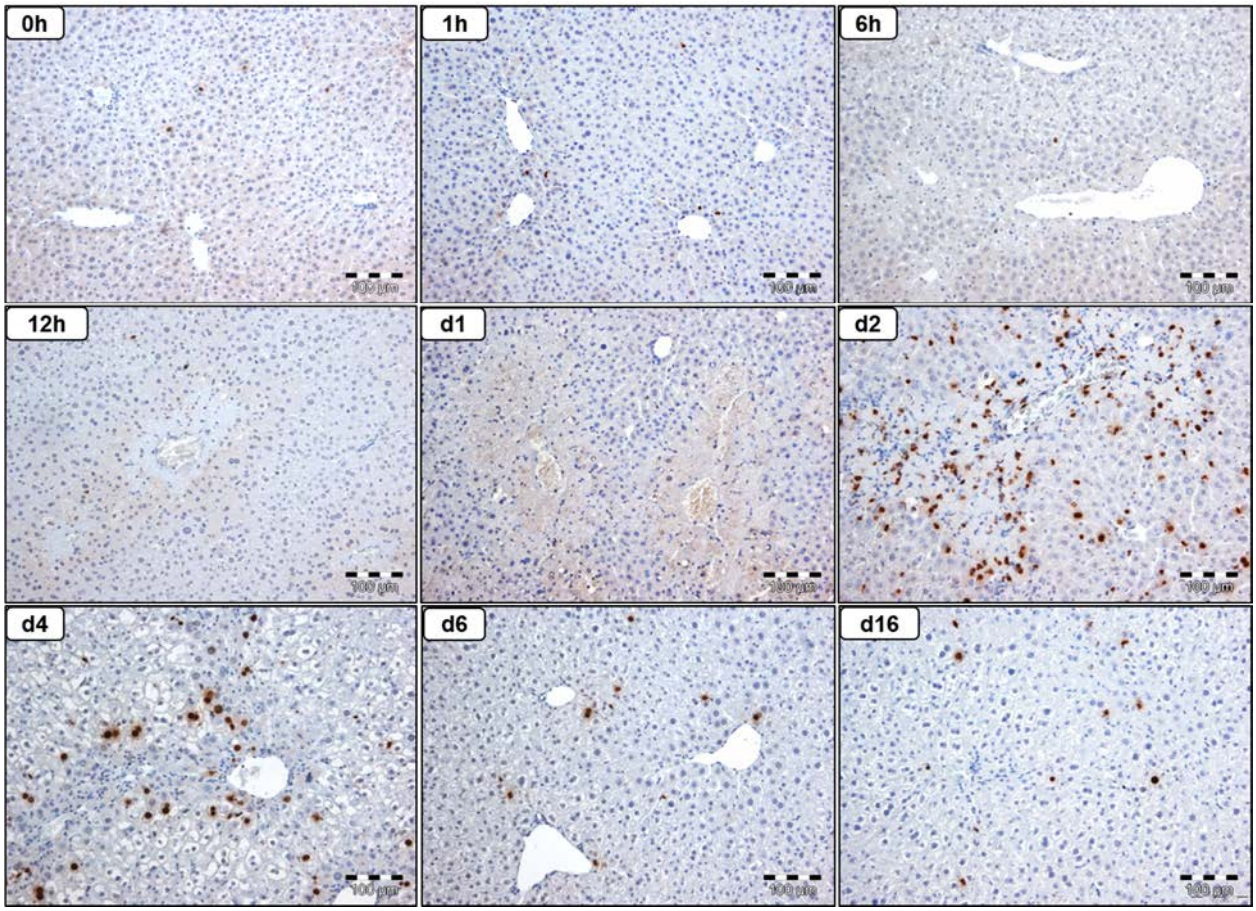

Figure 3. 11: 5-Bromo-2-deoxyuridine (BrdU) staining showing proliferation of liver cells (brown) at different time intervals after intoxication with 300 mg/kg APAP. The peak of proliferation can be seen on day 2 after APAP administration. Scale bars: 100 µm.

3.1.5 Compromised liver regeneration after intoxication with very high doses of acetaminophen

In order to investigate whether the regeneration process will be compromised after intoxication with very high doses of APAP, a dose of 450 mg/kg was injected i.p. using the same experimental setup shown in figure 3.9A. Approximately 60% of the mice died between days 2 and 3 after administration of such a high dose. Grossly, the liver of the dead mice showed obvious bleeding (figure 3.12A). By H&E staining, the livers showed severe haemorrhage (figure 3.12B). In addition, the dead cell area was not only restricted to the pericentral compartment of the liver lobule but also extended to the midzonal and fractions of the periportal area (figure 3.12B, C). The survivor mice showed compromised liver regeneration. Grossly, white spotted pattern of the liver was evident at the time between 6h and day 4 after intoxication (figure 3.13A). After day 6 most of the liver lobes looked similar to controls. However, some parts failed to regenerate and form scars (figure 3.13C). By H&E staining, the cetrilobular damage was visible at the time between 6h and day 4 (figure 3.13B). This was confirmed by elevation of the transaminases enzymes activity in this time frame (figure 3.14). In addition, haemorrhage was also evident especially on day 2 after intoxication. After day 6, the liver looked similar to controls with the exception of some parts which failed to regenerate (figure 3.13C).

In order to check whether hepatocytes proliferation was altered upon intoxication with such a high dose, BrdU staining was performed. The results showed compromised proliferation both from the spatial as well as the temporal point of view in comparison to proliferation after intoxication with 300 mg/kg. First, proliferation was delayed, started on day 4 after APAP administration (figure 3.15). Second, proliferation was mostly restricted to the pericentral compartment of the liver lobule. Furthermore, some proliferating hepatocytes were detached and appeared within the dead cell area (figure 3.15). In conclusion, intoxication with very high doses of APAP leads to high mortality rate and compromised liver regeneration for the survivors.

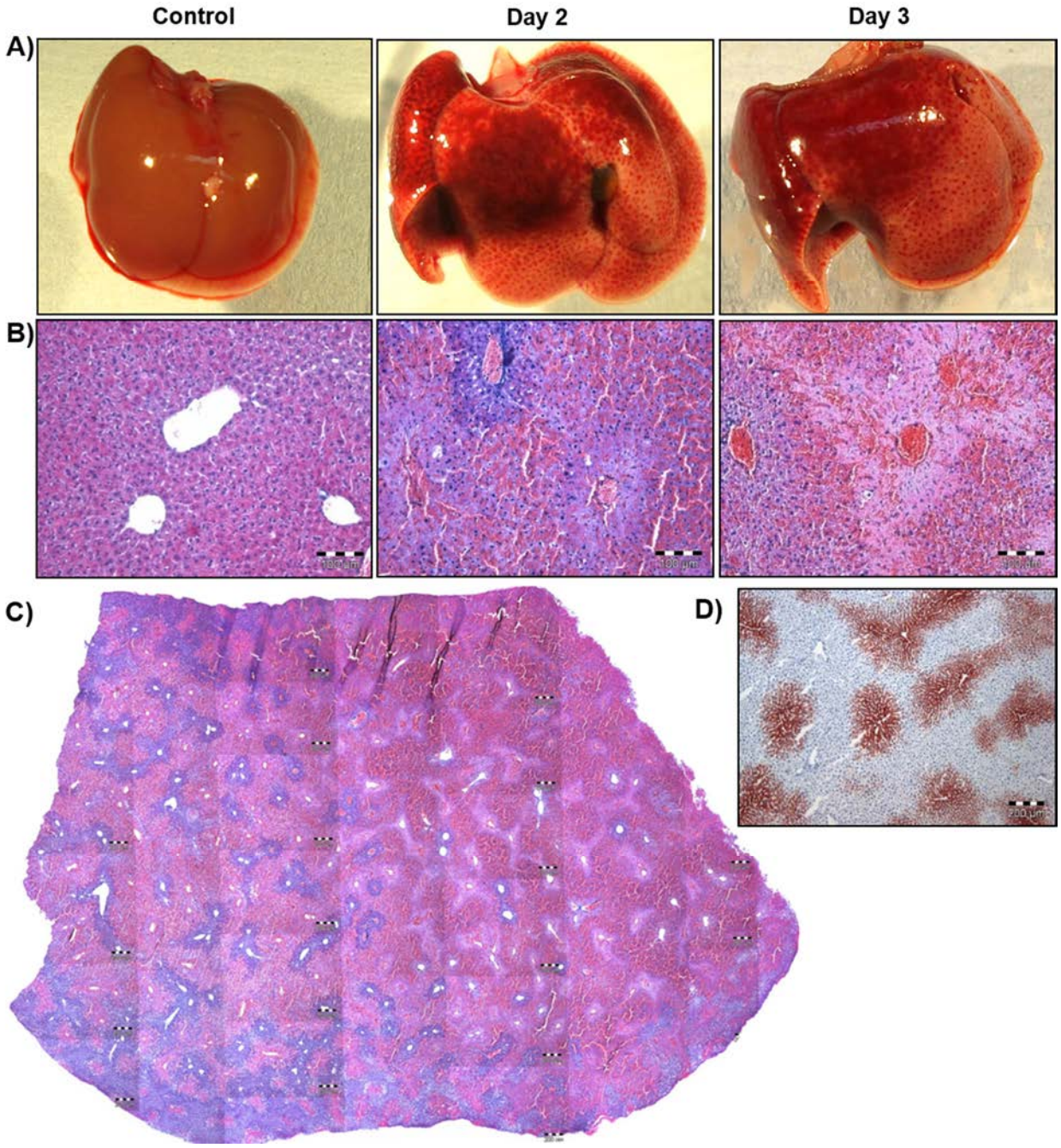

Figure 3. 12: Severe liver haemorrhage in mice died from acetaminophen overdose (450 mg/kg). (A) Gross pathology, (B) H&E staining. Scale bars: 100 µm. (C) Whole slide scan showing damage of approximately 80% of the liver parenchyma, which exceeds the territory of CYP2E1 positive area (D).

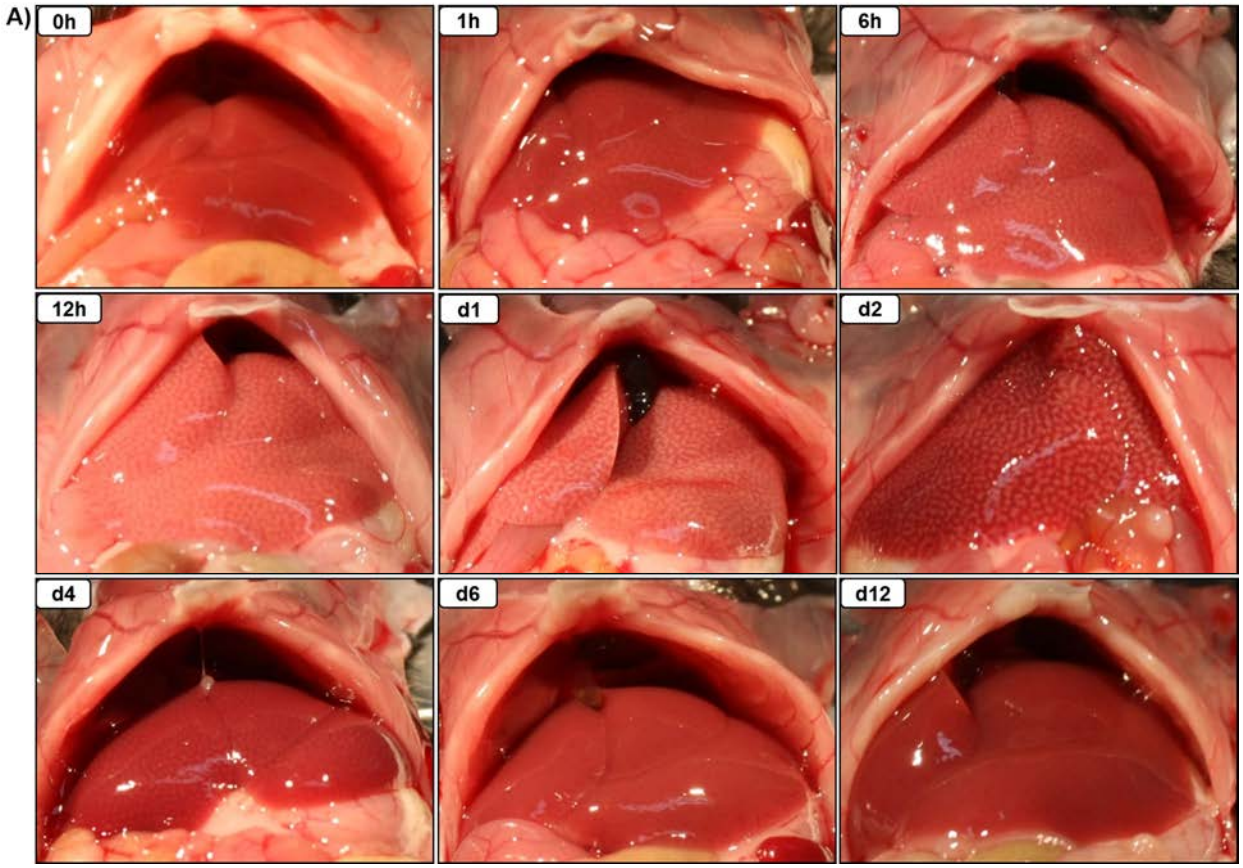

Figure 3. 13: Liver injury and regeneration after intoxication with 450 mg/kg APAP. (A) Gross pathology showing white spotted pattern started as early as 6h after APAP injection and remained evident up to day 4.

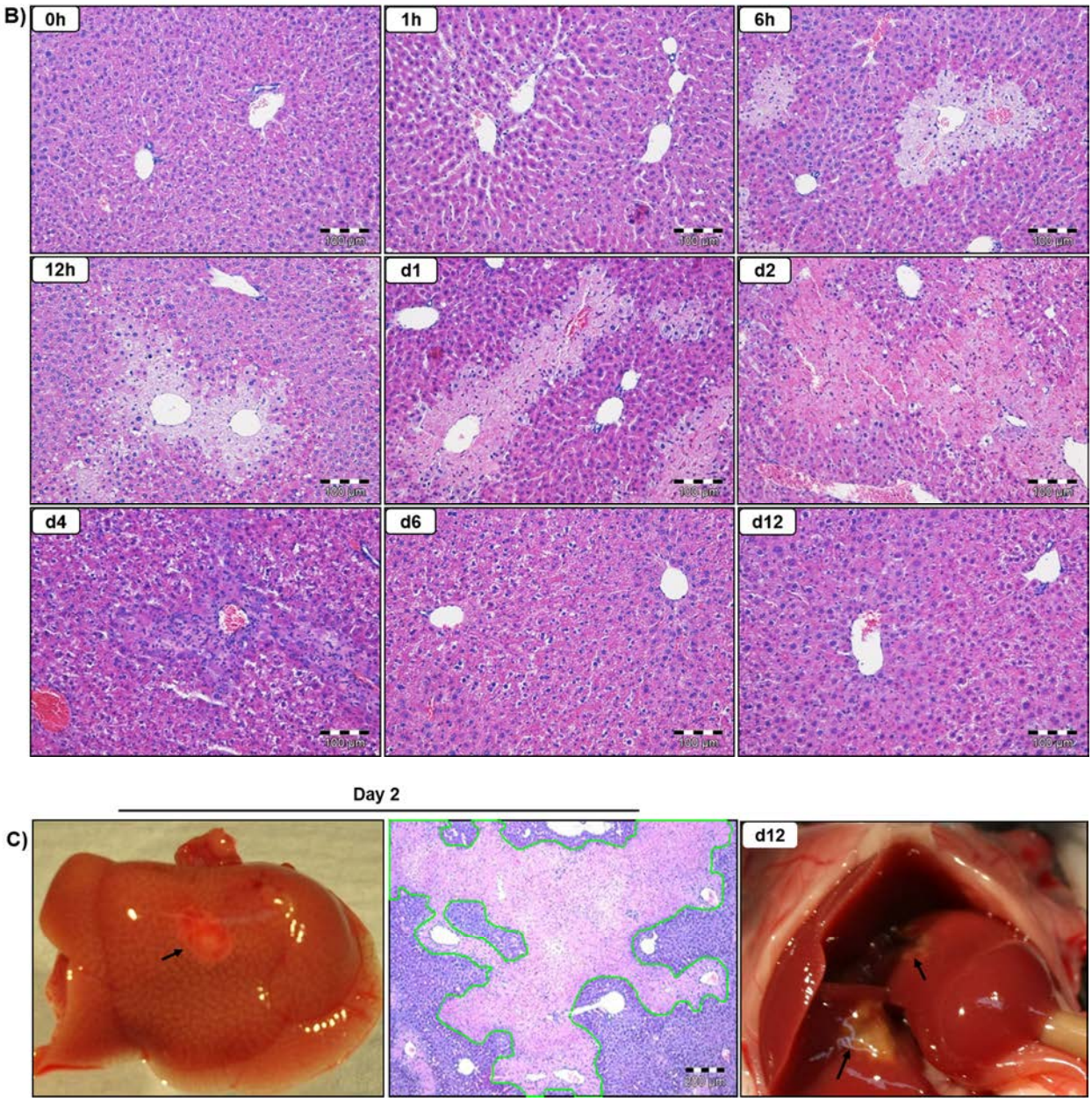

Figure 3.13 B, C: (B) H&E staining showing pericentral liver damage between 6h and day 4, and hemorrhage particularly on day 2 after APAP administration. Scale bars: 100 µm. After day 6, the liver looked normal with the exception of some parts which failed to regenerate and form scars (C). Scale bar: 200 µm.

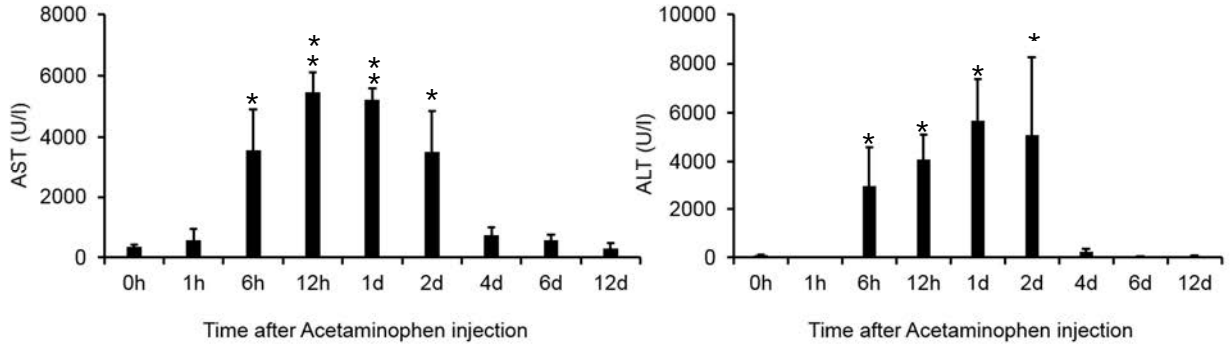

Figure 3. 14: Aspartate (AST) and alanine (ALT) transaminases activity in heart blood at different time periods after intoxication with 450 mg/kg APAP. The activity of both enzymes was markedly elevated at the time between 6h and day 2 after APAP administration. Data are means ± SE of three mice. **p<0.01, *p<0.05 when compared to the control (0h) group.

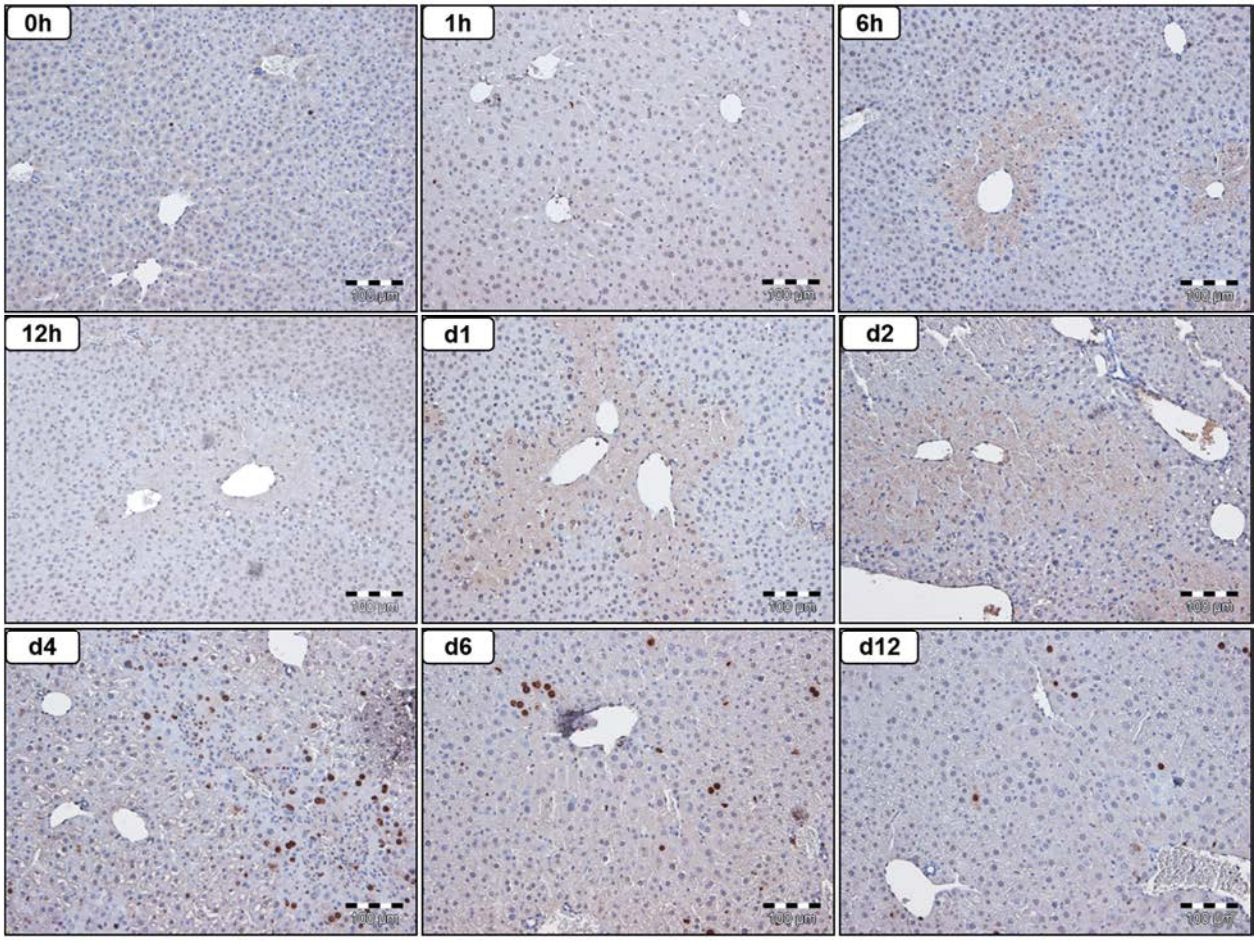

Figure 3. 15: 5-Bromo-2-deoxyuridine (BrdU) immunostaining in mice liver tissue sections at different time intervals after intoxication with APAP (450 mg/kg). Hepatocytes proliferation (brown) can be seen on day 4 and mostly restricted to the pericentral compartment of the liver lobule. Scale bars: 100 µm.

3.2 Immune cells infiltration following acetaminophen intoxication

The goal of the next step was to identify infiltrating immune cells during the destruction and regeneration processes following APAP intoxication. For this purpose, immunostaining was performed in liver tissue sections collected at different time periods after administration of 300 mg/kg APAP using antibodies against CD45 (pan leukocytes marker), LY6G (neutrophil marker), B220 (B cell marker), CD3 (T cell marker), and F4/80 (macrophage marker). The healthy livers showed few CD45 positive cells distributed homogeneously in the liver lobule, perhaps representing the liver resident Kupffer cells (figure 3.16). In contrast, upon APAP intoxication massive immune cell infiltration into the pericentral area of the liver lobule was observed at the time between 6h and day 4 (figure 3.16). After day 6 the liver appeared similar to the controls. In order to identify these infiltrating leukocytes, cell type specific antibodies were used. LY6G immunostaining revealed that the healthy liver were almost free from neutrophils. In contrast, neutrophils swarms were detected after APAP injection. The infiltration was mostly predominant during the destruction process between 6h and day 1 after APAP intoxication (figure 3.17). During the regeneration process (between days 2 and 4), neutrophils were also present but to a relatively low extent. After day 6, neutrophils were rarely detected. B220 and CD3 staining in healthy livers showed few scattered B and T cells, respectively. Following APAP intoxication, few infiltrating B and T cells were detected in the dead cell area during the destruction as well as the regeneration processes (figures 3.18 and 3.19). After day 4 the basal levels of B and T cells were visible in the liver similar as in controls. F4/80 staining showed the liver resident macrophages (Kupffer cells) distributed in the liver lobule with a slight preference to the midzonal area in controls (figure 3.20A). During the destruction process (6h till day 1 after APAP administration) more infiltrating macrophages were detected at the border of the dead cell area. Whereas, on day 4 after APAP injection, massive macrophages infiltration was detected at the pericentral compartment of the liver lobule (figure 3.20A). In order to differentiate between the resident kupffer cells and the infiltrating macrophages, a fluorescently labeled anti CD11b antiboby (expressed on the surface of infiltrating monocytes) was i.v. injected in healthy mice as well as on day 4 after APAP intoxication followed by intravital imaging of the liver

using two-photon microscopy. The liver resident macrophages (kupffer cells) showed F4/80 high CD11b low staining (figure 3.20B). In contrast, the infiltrating macrophages showed F4/80 high, CD11b high staining and massively present in the pericentral compartment of the liver lobule on day 4 after APAP challenge (figure 3.20B).

In conclusion, immune cells present in the liver are highly altered after APAP intoxication with particularly high neutrophils infiltration during the destruction process and massive macrophages infiltration during the regeneration process.

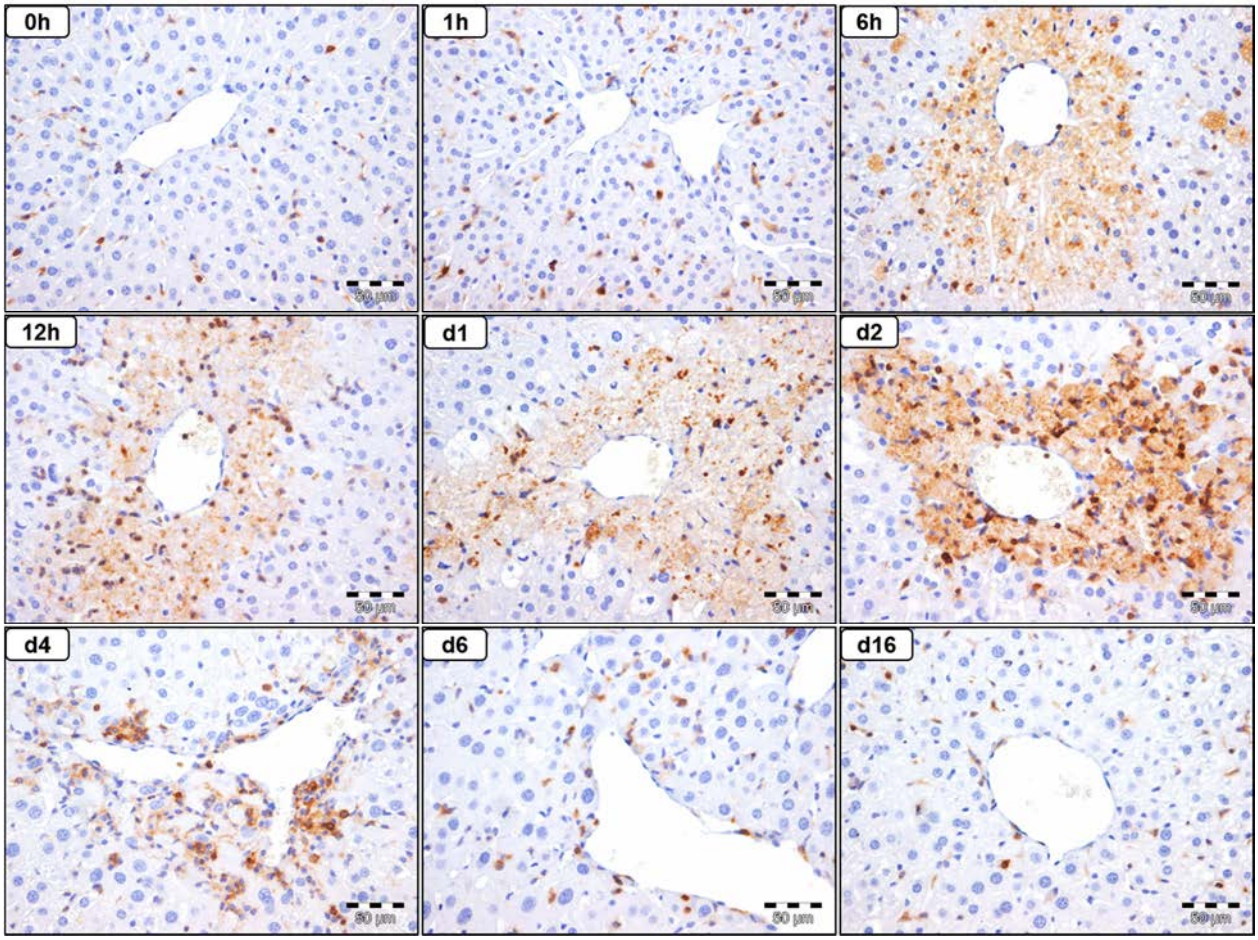

Figure 3. 16: CD45 immunostaining in mice livers showing leukocytes infiltration at different time intervals after injection of 300 mg/kg APAP. Scale bars: 50 µm.

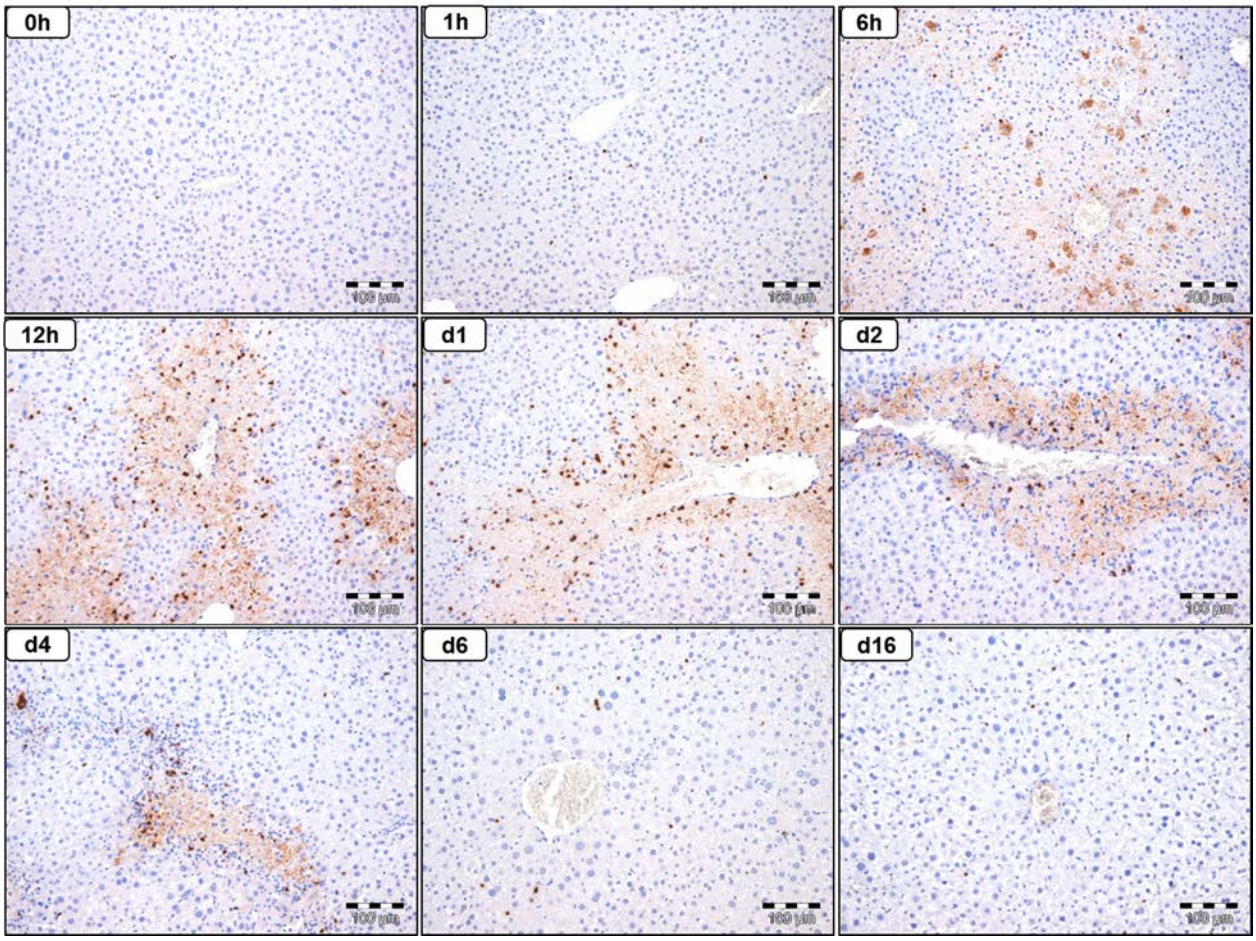

Figure 3. 17: Immunostaining of liver tissue sections using antibodies against LY6G showing infiltration of neutrophils at different time intervals after administration of APAP (300 mg/kg). The peak of neutrophils infiltration appears between 12h and day 1 after APAP injection. Scale bars: 100 µm.

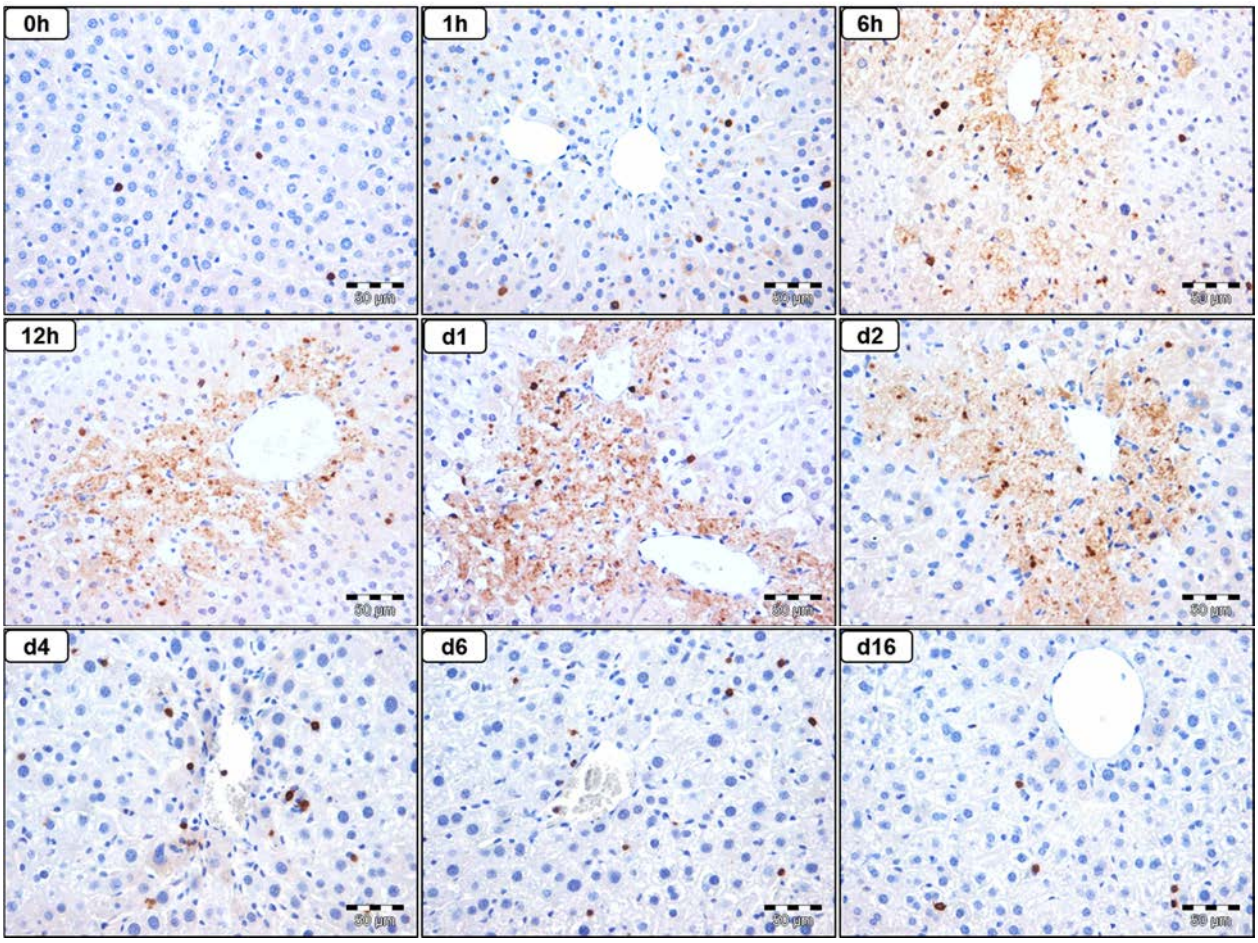

Figure 3. 18: B220 immunostaining in mice liver tissue sections at different time intervals after APAP intoxication (300 mg/kg). The staining shows very few infiltrating B cells into the dead cell area during liver injury and regeneration. Scale bars: 50 µm.

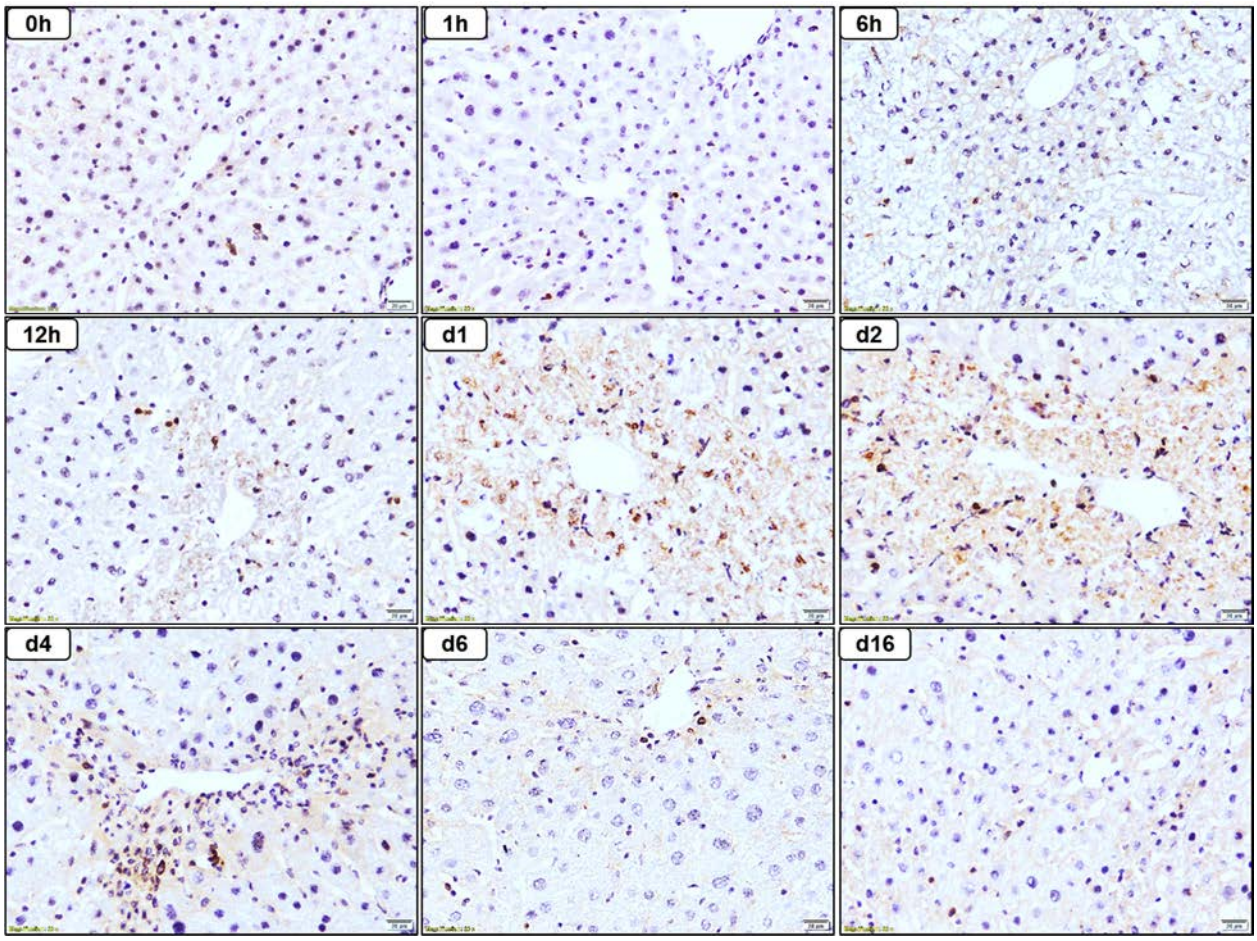

Figure 3. 19: CD3 immunostaining in mice liver tissue sections at different time intervals after APAP intoxication (300 mg/kg). The staining shows few infiltrating T cells into the dead cell area during liver injury and regeneration. Scale bars: 50 µm.

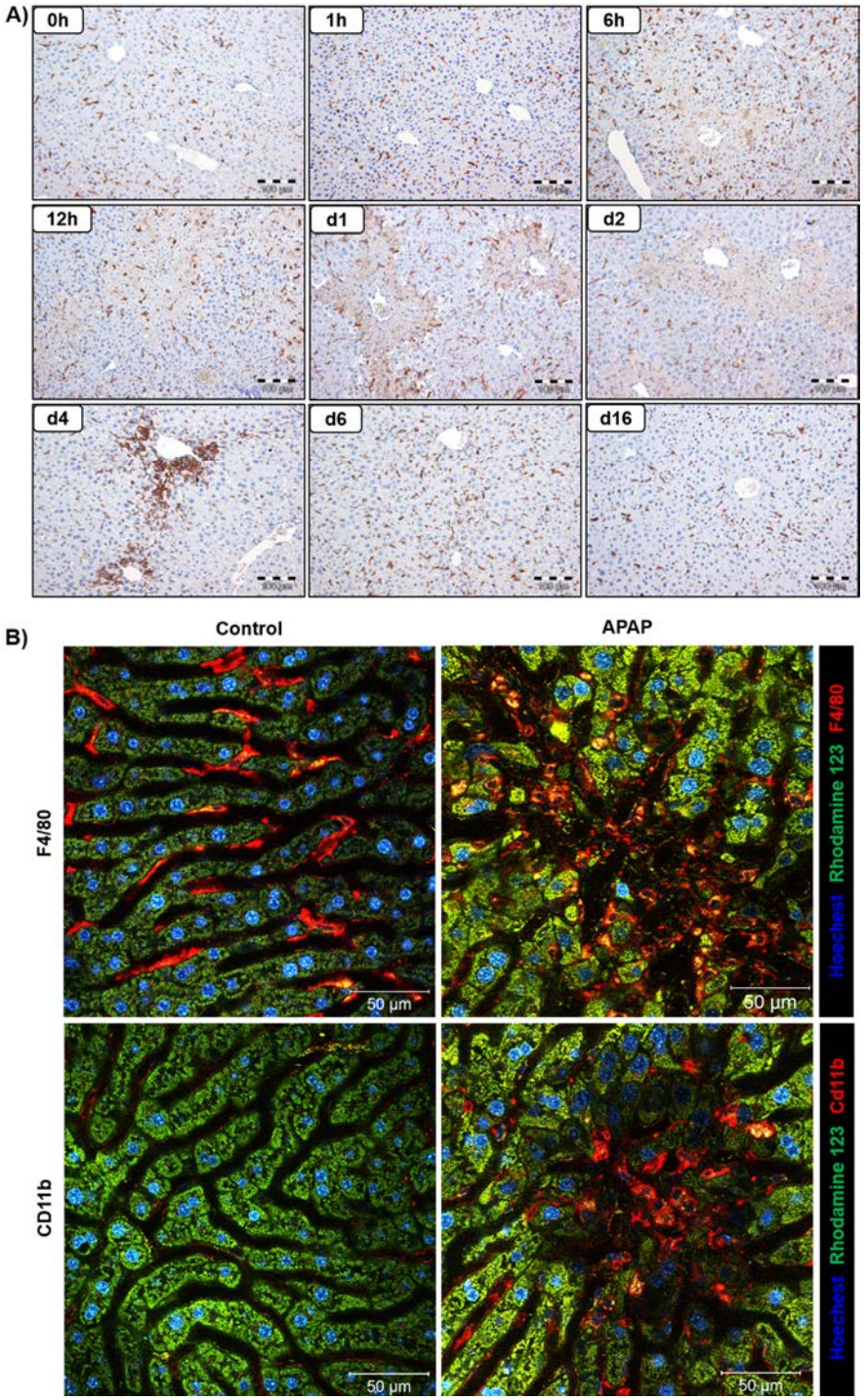

Figure 3. 20: Macrophages infiltration after APAP intoxication. (A) F4/80 immunostaining showing resident as well as infiltrating macrophages at different time intervals after APAP injection (300 mg/kg). The staining shows massive macrophages infiltration into the pericentral compartment of the liver lobule during liver regeneration (day 4). Scale bars: 100 µm. (B) Intravital imaging of macrophages in healthy liver as well as on day 4 after APAP intoxication stained by fluorescently labeled anti-F4/80 (pan macrophages marker) or anti-CD11b (infiltrating macrophages marker) antibodies. The resident kupffer cells show F4/80 high, CD11b low staining. Whereas, the infiltrating macrophages show both high F4/80 as well as CD11b staining. Scale bars: 50 µm.

3.3 Hepatic stellate cells dynamics during liver injury and regeneration

Due to the significant changes in the immune system of the liver which is known to interact with the non-parenchymal cells, the next chapter will focus on the state of HSCs during liver injury and regeneration. In order to distinguish activated and quiescent HSCs, liver tissue sections were collected at different time intervals after APAP intoxication (300 mg/kg; see experimental design in figure 3.9A) and immunostained using antibodies against desmin (a marker of quiescent as well as activated HSCs) and alpha-smooth muscle actin (α-SMA; a marker of activated HSCs). As expected, HSCs are quiescent in healthy livers as indicated by desmin positive and α-SMA negative staining (figure 3.21). Whereas, the quiescent HSCs infiltrate the dead cell area on day one after APAP administration and get activated on day two as evidenced by α-SMA positive staining (figure 3.21). However, the number of activated HSCs was reduced by day four after APAP intoxication and completely cleared out by day six. Despite of massive killing of hepatocytes and HSCs activation this did not lead to liver fibrosis as evidenced by sirius red negative staining (figure 3.21). In order to confirm these interesting findings, similar experiments were performed using another model of liver injury in which a single dose of the hepatotoxic agent CCl_4 (1.6 g/kg) was injected. Similar to APAP, CCl_4 intoxication lead to massive killing of the pericentral hepatocytes (figure 3.22). This was followed by massive activation of HSCs particularly on day 2 which were completely eliminated by day 6 after CCl_4 administration without fibrogenesis (figure 3.22). In conclusion, acute liver injury leads to transient massive activation of HSCs without fibrosis development.

Since HSCs activation is known to be associated with fibrogenesis which contradicts with the current results, we decided to check HSCs activation in liver fibrosis under our experimental setup. For this purpose, C57BL/6N mice were treated repeatedly with CCl_4 (1 g/kg) twice a week for two months. Subsequently, liver tissue samples were collected in a time-resolved manner after the last injection (figure 3.23A) and analyzed for HSCs activation and fibrosis development. Repeated CCl_4 administration lead to pericentral liver damage but less than that observed after an acute challenge (figure 3.23B, H&E). This was associated with moderate activation of HSCs (figure 3.23B, desmin and α-SMA), which also disappeared after day 6. However, in contrast to the acute situation, this

scenario lead to liver fibrosis as evidenced by positive sirius red staining (figure 3.23B) which persist upto day 10 after the last CCl_4 injection. In conclusion, the data show that the presence of cell damage and the extent of stellate cells activation does not necessarily correlate with the degree of liver fibrosis.

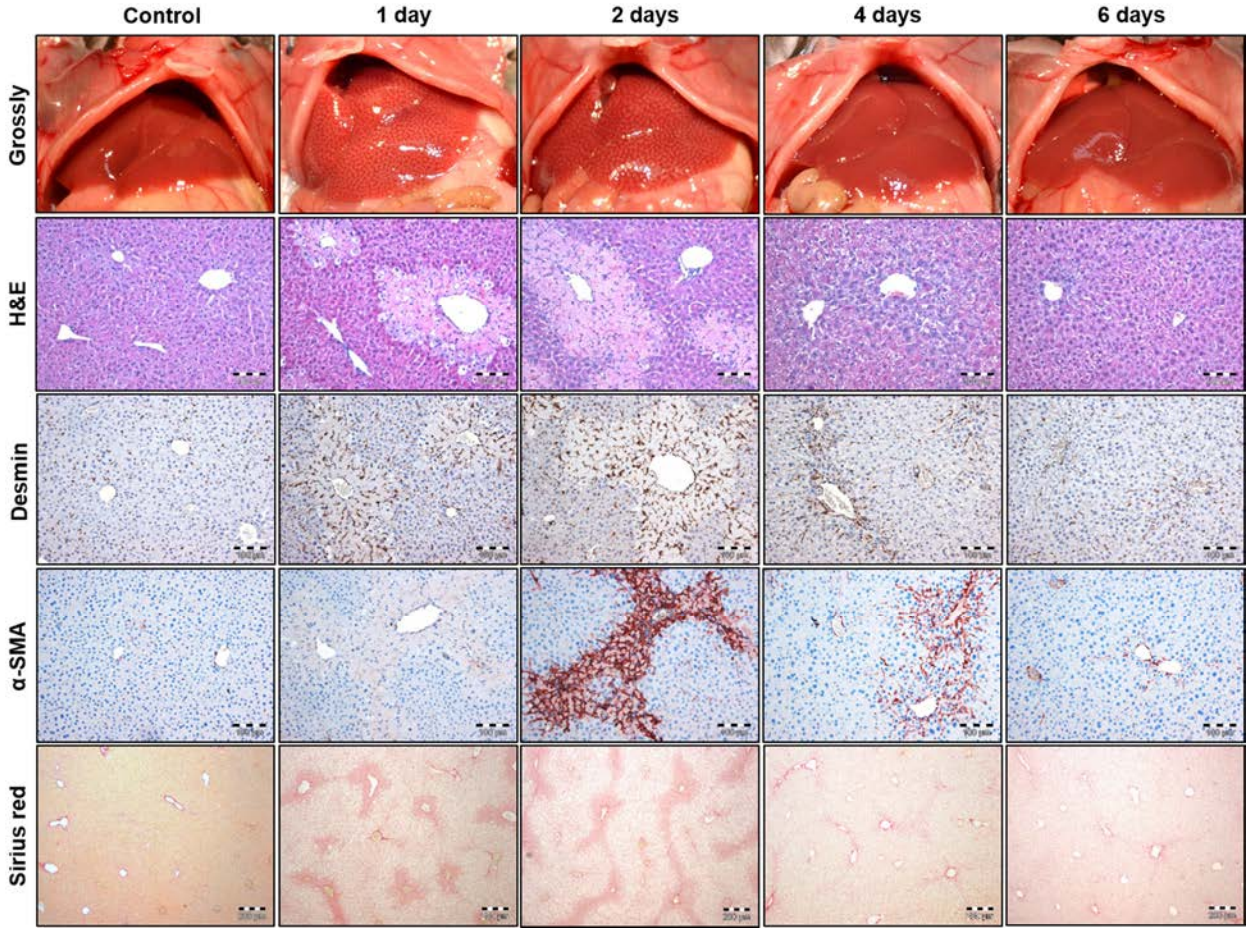

Figure 3. 21: No liver fibrosis despite of massive cell death and stellate cells activation after acute APAP challenge. The images show mice livers at different time intervals after intoxication with 300 mg/kg APAP. The panels show macroscopic appearance (grossly), microscopic appearance by hematoxylin and eosin staining (H&E), hepatic stellate cells (desmin), activated stellate cells (alpha-smooth muscle, α-SMA); scale bars: 100 µm, and sirius red staining as a marker of fibrosis; scale bars: 200 µm.

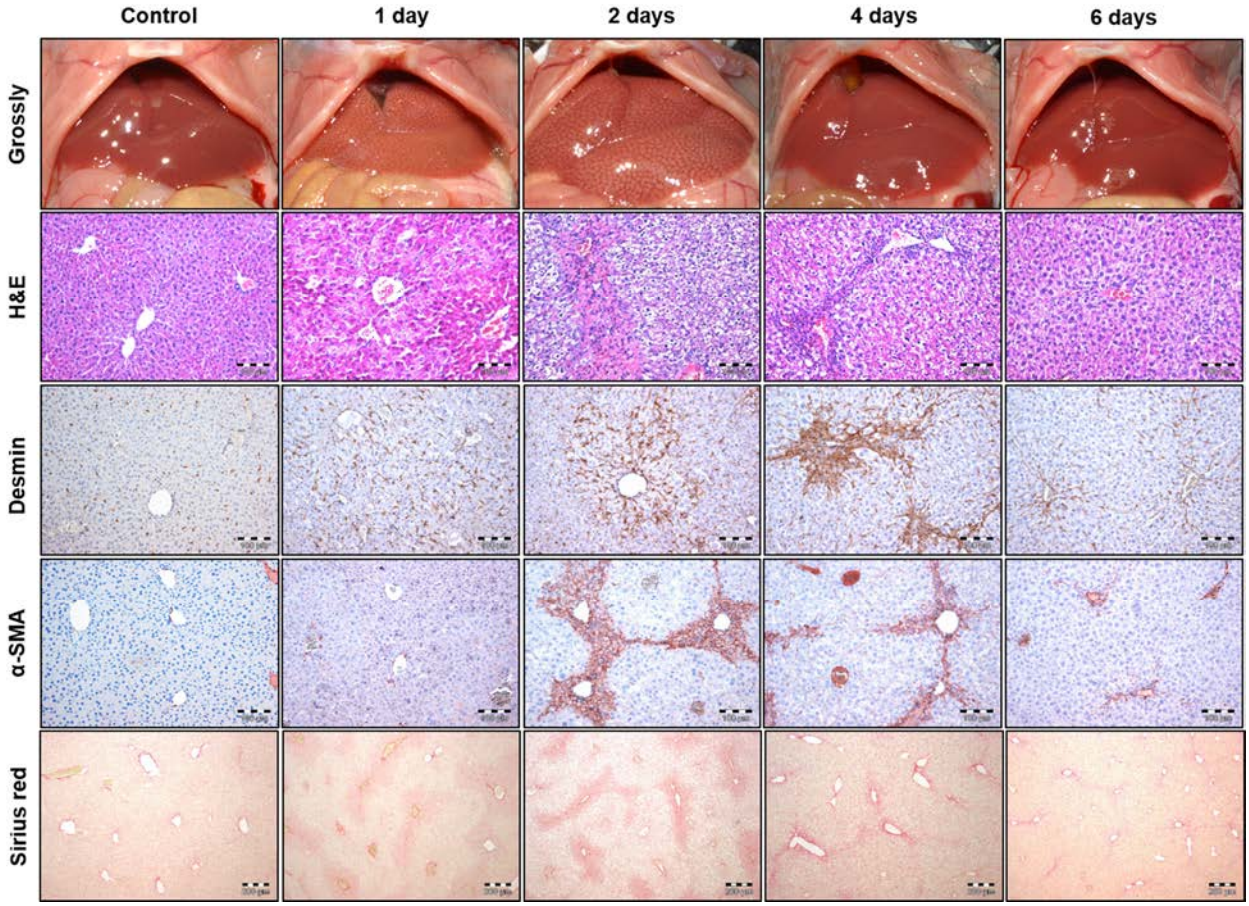

Figure 3. 22: No liver fibrosis despite of massive cell death and stellate cells activation after acute CCl_4 challenge. The images show mice livers at different time intervals after intoxication with 1.6 g/kg CCl_4. The panels show macroscopic appearance (grossly), microscopic appearance by hematoxylin and eosin staining (H&E), hepatic stellate cells (desmin), activated stellate cells (alpha-smooth muscle, α-SMA); scale bars: 100 µm, and sirius red staining as a marker of fibrosis; scale bars: 200 µm.

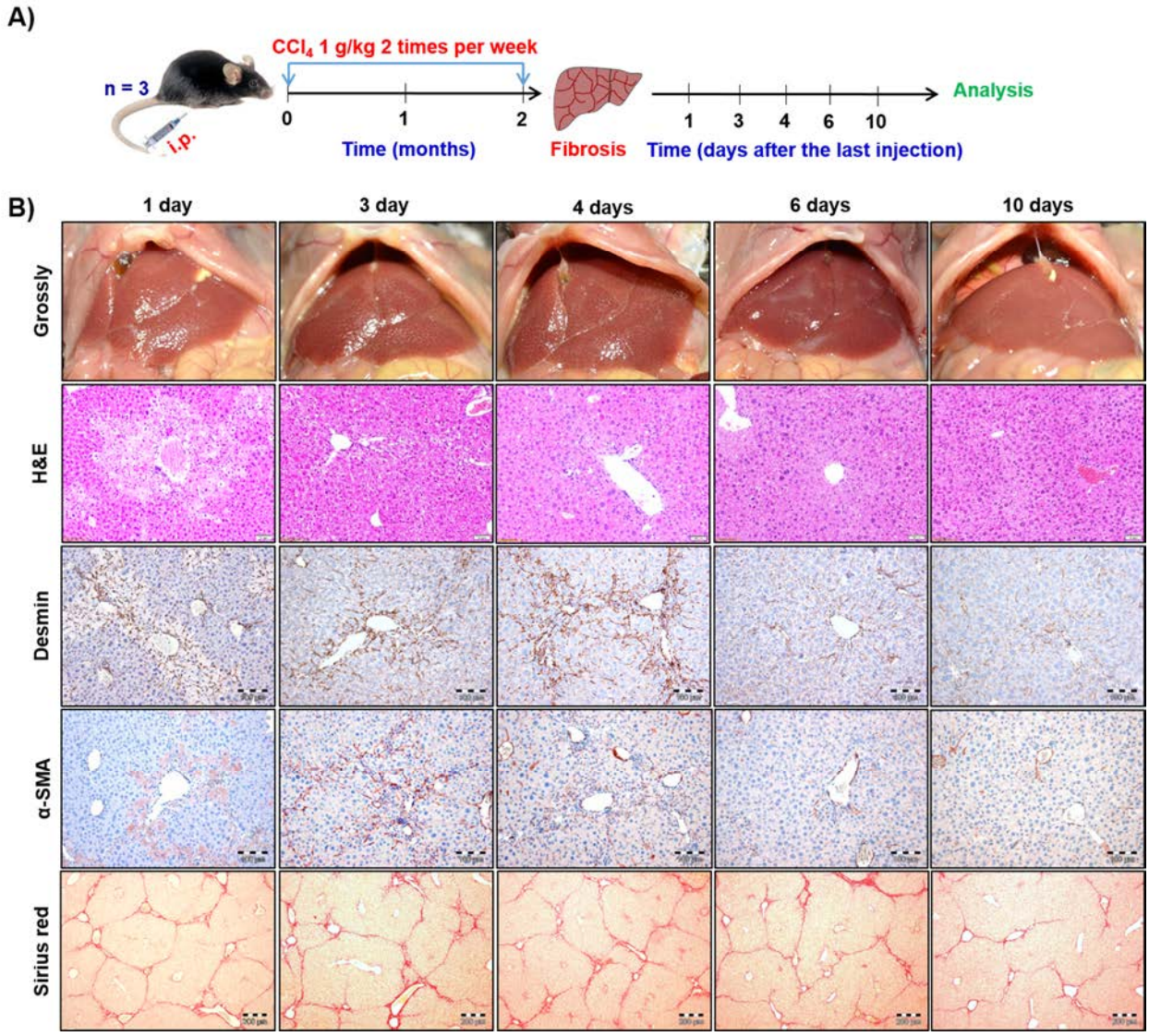

Figure 3. 23: Moderate cell killing and activation of HSCs leads to liver fibrosis. (A) Experimental design of a fibrosis mouse model: male C57BL/6N mice were injected repeatedly with CCl_4 (1g/kg, i.p.), twice a week for 2 months. Following the last dose of CCl_4, the liver was harvested at different time periods (days 1, 3, 4, 6 and 10). Three mice were scarified at each time period. (B) Mice livers at different time intervals after the last dose CCl_4.The panels show macroscopic appearance (grossly), microscopic appearance by hematoxylin and eosin staining (H&E), hepatic stellate cells (desmin), activated stellate cells (alpha-smooth muscle, α-SMA); Scale bars: 100 µm, and sirius red staining as a marker of fibrosis; scale bars: 200 µm.

3.4 Mechanisms of activated HSCs elimination

For a deeper understanding of the fate of activated HSCs following acute and chronic liver injury, the mechanisms of elimination were studied in both damage scenarios. First, I checked whether the activated HSCs revert to the quiescent state. For this purpose, liver tissue sections were co-stained using antibodies against desmin and α-SMA. After repeated CCl_4 administration, co-localization of desmin and α-SMA signals was visible on day 3 following the last dose of CCl_4. In contrast, on day four, the signal of α-SMA markedly decreased despite of accumulation of HSCs on the pericentral area of the liver lobule as indicated by the positive desmin staining (figure 3.24A). Following an acute challenge with APAP, co-localization of desmin and α-SMA signals was also detected in the dead cell area at the time between days 2 and 4 after APAP administration (figure 3.24B). However, after day 4 the signals of both α-SMA and desmin disappeared from the pericentral compartment and only the basal desmin positive HSCs appeared homogenously distributed in the liver lobule (figure 3.24B). These results show that reversion of activated HSCs to a quiescent phenotype could be a way of elimination of activated HSCs during fibrosis recovery but not during regeneration from an acute challenge.

Second, the role of apoptosis in elimination of activated HSCs was studied. For this purpose, liver tissue sections were stained with TUNEL as a marker of DNA breaks. Significant TUNEL positive signal was detected in the fibrosis scenario, particularly on day 4 after the last CCl_4 injection (figure 3.25A). The signals were mostly in HSCs as indicated by co-localization with desmin staining (figure 3.25A). In contrast, in case of APAP induced-acute liver injury TUNEL signal was not detectable during the regeneration phase (figure 3.25B). In order to confirm the negative results, a positive control sample was treated with DNase I on day 3 after APAP intoxication; the time when α-SMA signal reached to the peak. In addition, an early time point (8h after APAP injection) was also included; the time when killing of hepatocytes was active. Both conditions showed that the TUNEL staining worked properly also in activated hepatic stellate cells (figure 3.25 C, D). These results show that also apoptosis is not a relevant pathway for elimination of activated HSCs following acute liver injury.

Third, the presence of macrophages and natural killer cells (NK) as main players involved in elimination of activated HSCs via induction of apoptosis (Radaeva et al. 2006; Tacke and Trautwein 2015; Tian et al. 2013) was investigated in both damage scenarios. In order to check the interaction of macrophages with HSCs, co-staining of liver tissue sections using antibodies against α-SMA and F4/80 was performed. The results showed massive macrophages infiltration during liver regeneration after acute as well as chronic injury (figure 3.26 A, B). To get a deeper insight after the acute damage scenario, confocal z-stacks imaging and 3-D reconstructions were performed at different time intervals following APAP intoxication. The results revealed massive infiltration of macrophages into the pericentral compartment and co-localization with HSCs on day 4 after APAP administration, the time when activated HSCs disappeared (figure 26 C).

NK cells were visualized *in vivo* by two-photon microscopy after tail vein injection of NK1.1 antibody. In contrast to macrophages, NK cell infiltration was observed only after repeated CCl_4 intoxication (figure 3.26 D). In conclusion, although activated HSCs are eliminated both after acute and chronic liver damage scenarios, the responsible mechanisms seem to be different.

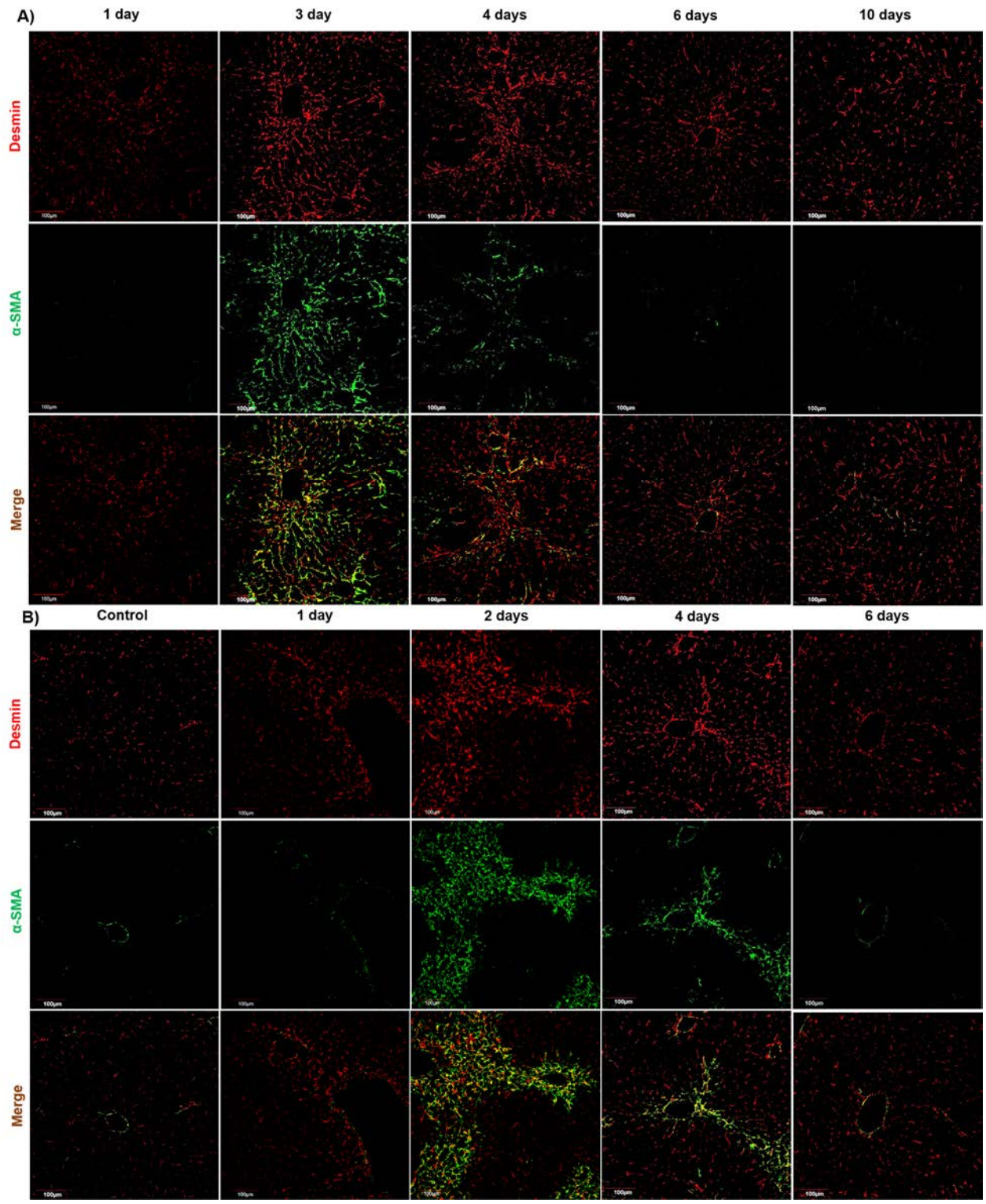

Figure 3. 24: Activated HSCs are eliminated by reversion to a quiescent phenotype during fibrosis recovery but not during regeneration from an acute challenge. Mice liver tissue sections were co-stained using fluorescently labeled antibodies against α-SMA and desmin at different time periods after intoxication with either: (A) repeated CCl_4 injection (1 g/kg); twice a week for 2 months, or (B) a single dose of APAP (300 mg/kg). The images show massive accumulation of desmin positive quiescent HSCs (α-SMA negative) in the pericentral compartment of the liver lobule during fibrosis recovery (day 4) but not during regeneration from an acute APAP challenge. Scale bars: 100 µm.

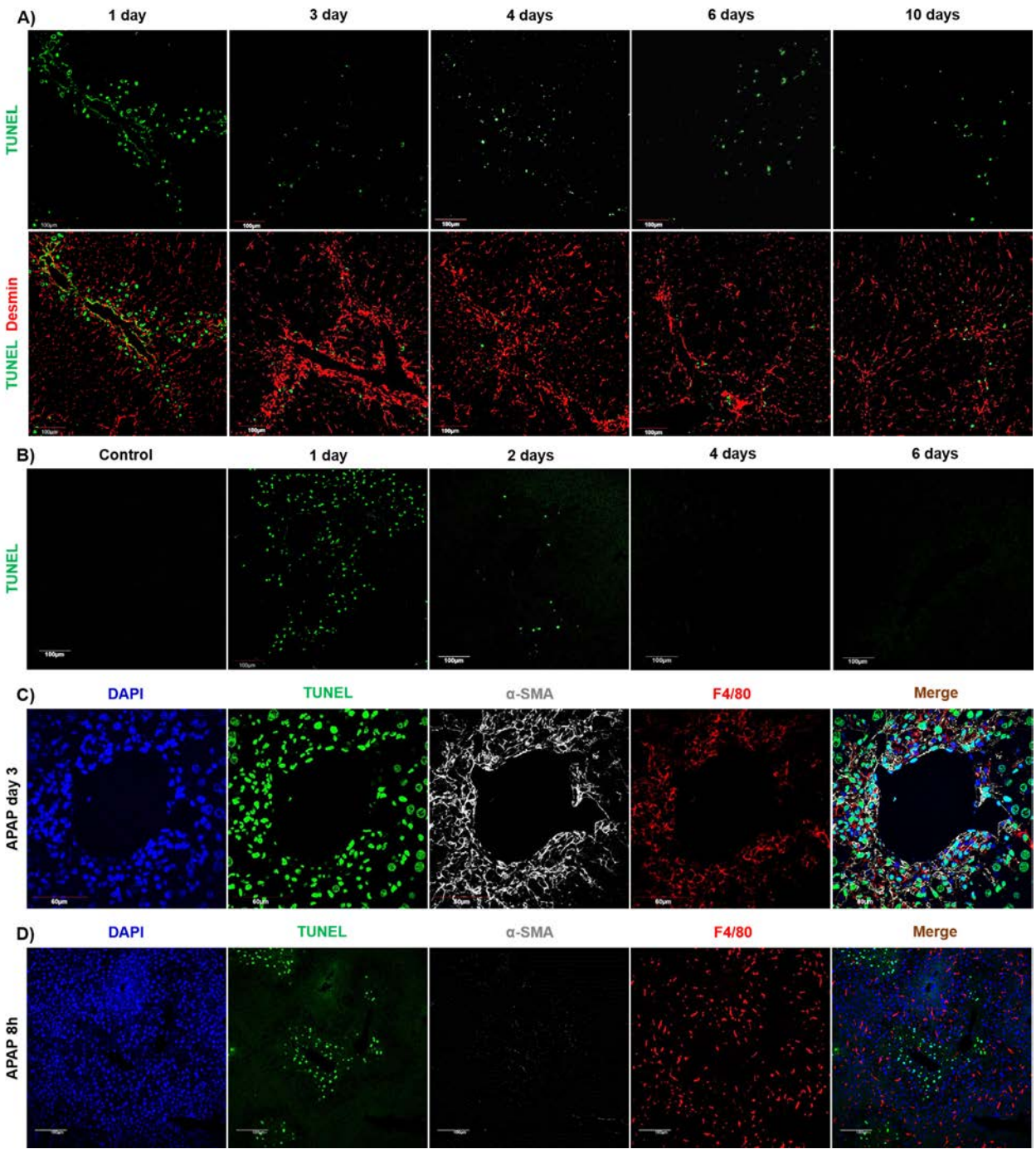

Figure 3. 25: Apoptosis is a relevant pathway for removal of activated HSCs during fibrosis recovery but not during regeneration from an acute challenge. (A) Positive TUNEL signal in activated HSCs during fibrosis recovery following repeated CCl_4 intoxication (1 g/kg, twice a week for 2 months). Scale bars: 100 µm. (B) TUNEL staining at different time intervals after administration of a single dose of APAP 300 mg/kg. The images show no apoptosis at the time when activated HSCs are eliminated (day 4). Scale bars: 100 µm. (C) Positive TUNEL signal in all liver cells after DNase I pre-treatment on day 3 after APAP intoxication. Scale bars: 50 µm. (D) Positive TUNEL signals in the pericentral hepatocytes at 8h after APAP intoxication (300 mg/kg). Scale bars: 100 µm.

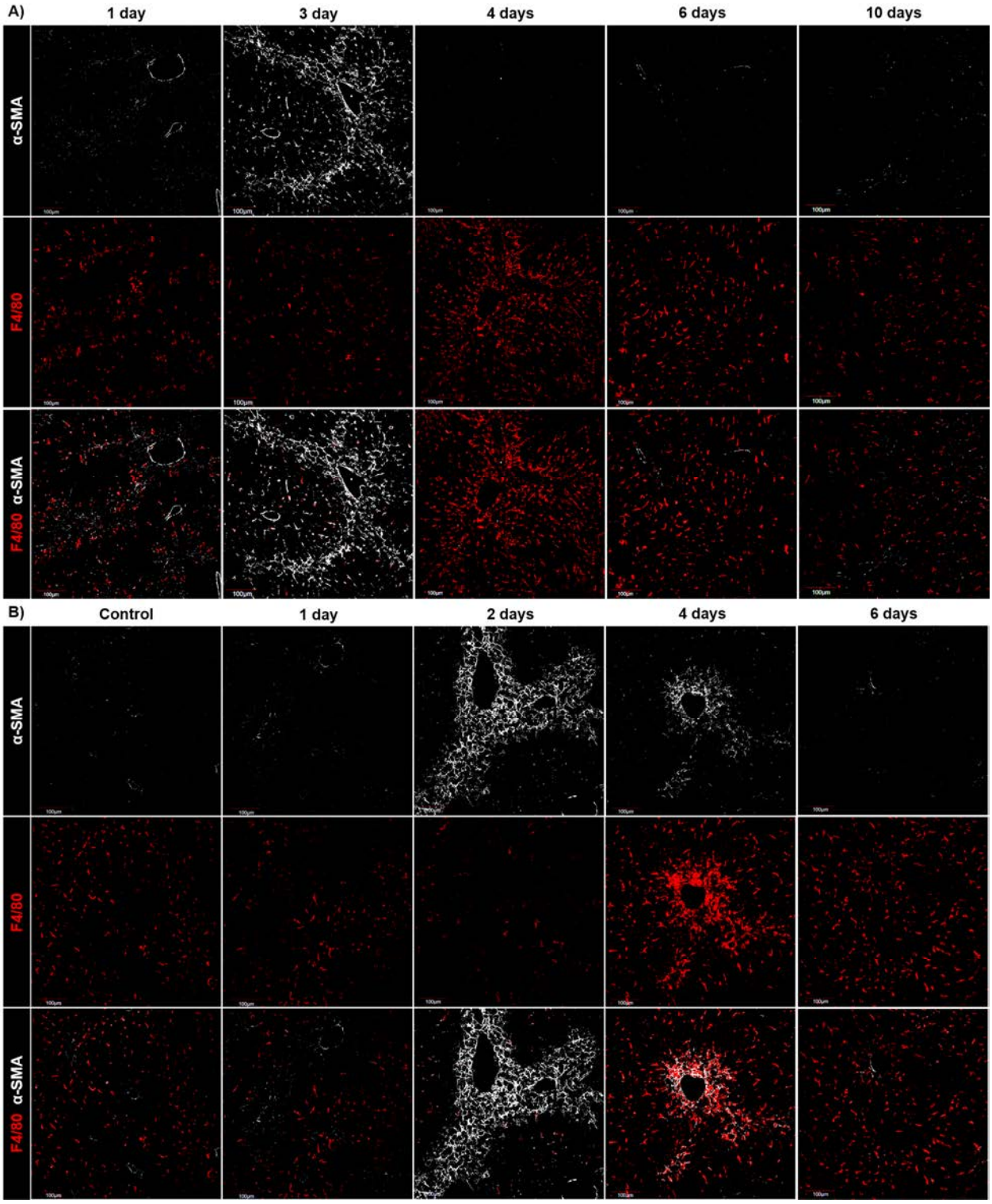

Figure 3. 26: Macrophages and natural killer (NK) cells infiltration during liver recovery following an acute or chronic challenges. Alpha smooth actin (α-SMA) and F4/80 co-staining in mice livers at different time intervals after either: (A) repeated CCl_4 (1 g/kg, twice a week for 2 months) or (B) single APAP (300 mg/kg) administration. The images show massive macrophages infiltration at the time when activated stellate cells are eliminated. Scale bars: 100 µm.

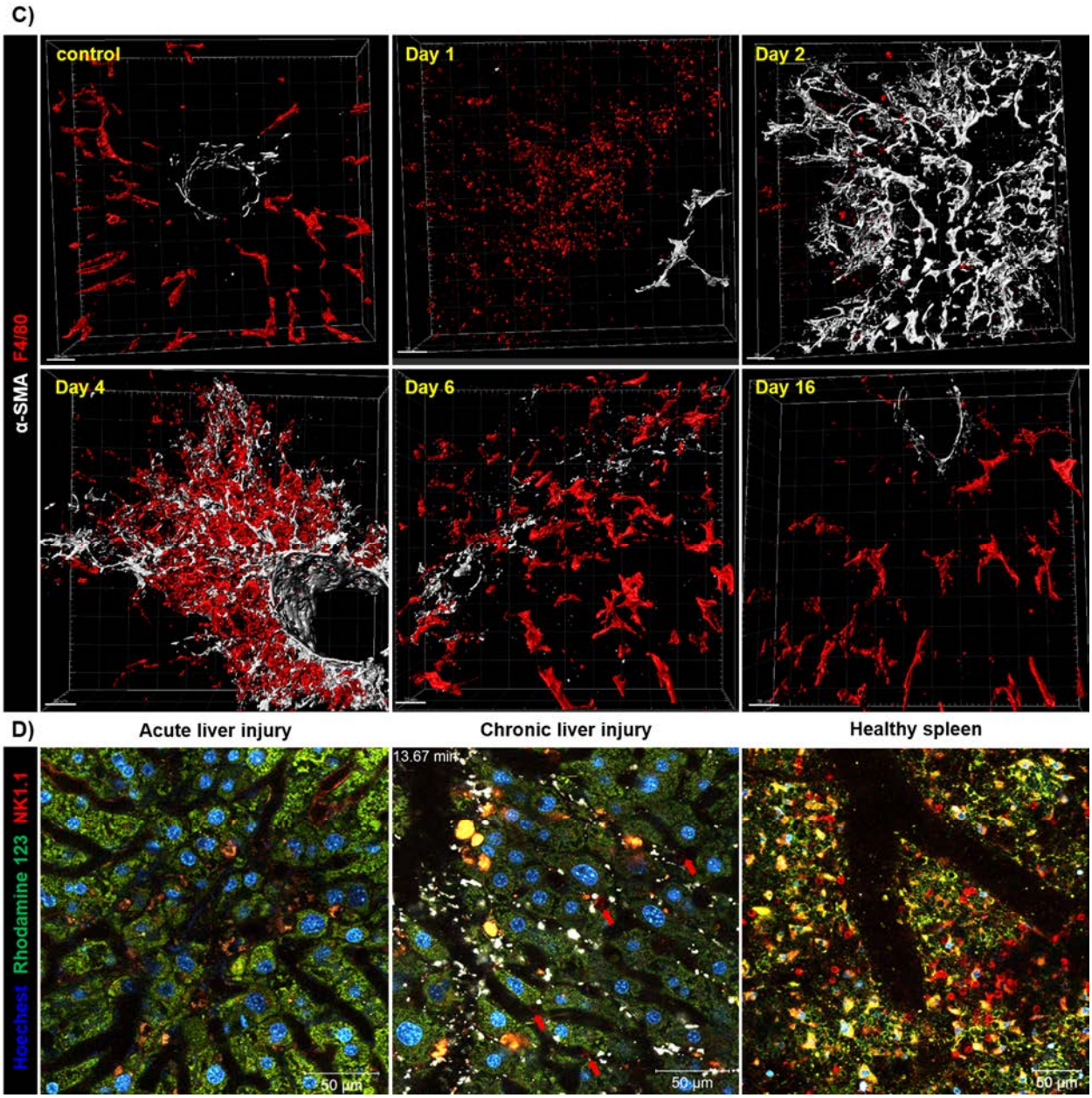

Figure 3.26 C, D: (C) 3D reconstructions of confocal micrographs of liver tissue slices co-stained with antibodies against α-SMA (white) and F4/80 (red) at different time intervals after APAP intoxication. The images show activation of HSCs on day 2 after APAP administration. On day 4, massive infiltration of macrophages into the pericentral compartment of the liver lobule can be seen which frequently co-localize with α-SMA signal. Scale bars: 20 µm. (D) *In vivo* imaging of NK cells after i.v. injection of NK1.1 antibody in mice on day 4 following single APAP injection (300 mg/kg) or repeated CCl_4 intoxication (1 g/kg, twice a week for 2 months). The liver morphology is visualized by i.v. injection of rhodamine 123 and the nuclei are visualized by i.v. injection of Hoechst 33258. The images show NK cells infiltration during fibrosis recovery (arrows) but not during regeneration from an acute challenge. The spleen of a healthy mouse serves as a positive control. Scale bars: 50 µm.

3.5 Role of macrophages in elimination of activated HSCs during liver regeneration

From the results presented in the previous chapter, it seems that infiltrating macrophages are the main players in removal of activated HSCs following acute liver injury. To get a deeper insights about the role of macrophages in HSCs removal, a mouse system in which macrophages were depleted by administration of clodronate containing liposomes was used. In order to select the ideal time for macrophage depletion a preliminary experiment was performed in which clodronate was injected i.v. either before (one day), simultaneously with or after (day 1, 2 or 3) APAP administration (figure 3.27A). The liver tissue was collected on day 6 after APAP injection. The dead cell area was recovered in all treated groups as shown by H&E staining (figure 3.27B). The efficiency of clodronate in removal of macrophages was confirmed by the negative F4/80 staining (figure 3.27C). All clodronate treated mice showed a strong α-SMA signal compared to the saline treated group (figure 3.27D). However, removal of macrophages on day 2 after APAP injection lead to the highest α-SMA signal on day 6. In order to check whether macrophages are also important for activation of HSCs, an experiment was performed in which the mice were treated with clodronate one day before APAP administration and the activation state of HSCs was checked on day 2 after APAP injection (figure 3.28A). Clodronate treatment successfully removed all macrophages as evidenced by F4/80 negative staining (figure 3.28B). Interestingly, the diameter of the dead cell area was less in clodronate treated mice (figure 3.28B). Moreover, the number of activated HSCs was strongly reduced following macrophage depletion (figure 3.28B). In conclusion, blocking of macrophages by clodronate affects both activation as well as removal of HSCs. Furthermore, administration of clodronate two days after APAP treatment is the most critical time for elimination of activated HSCs.

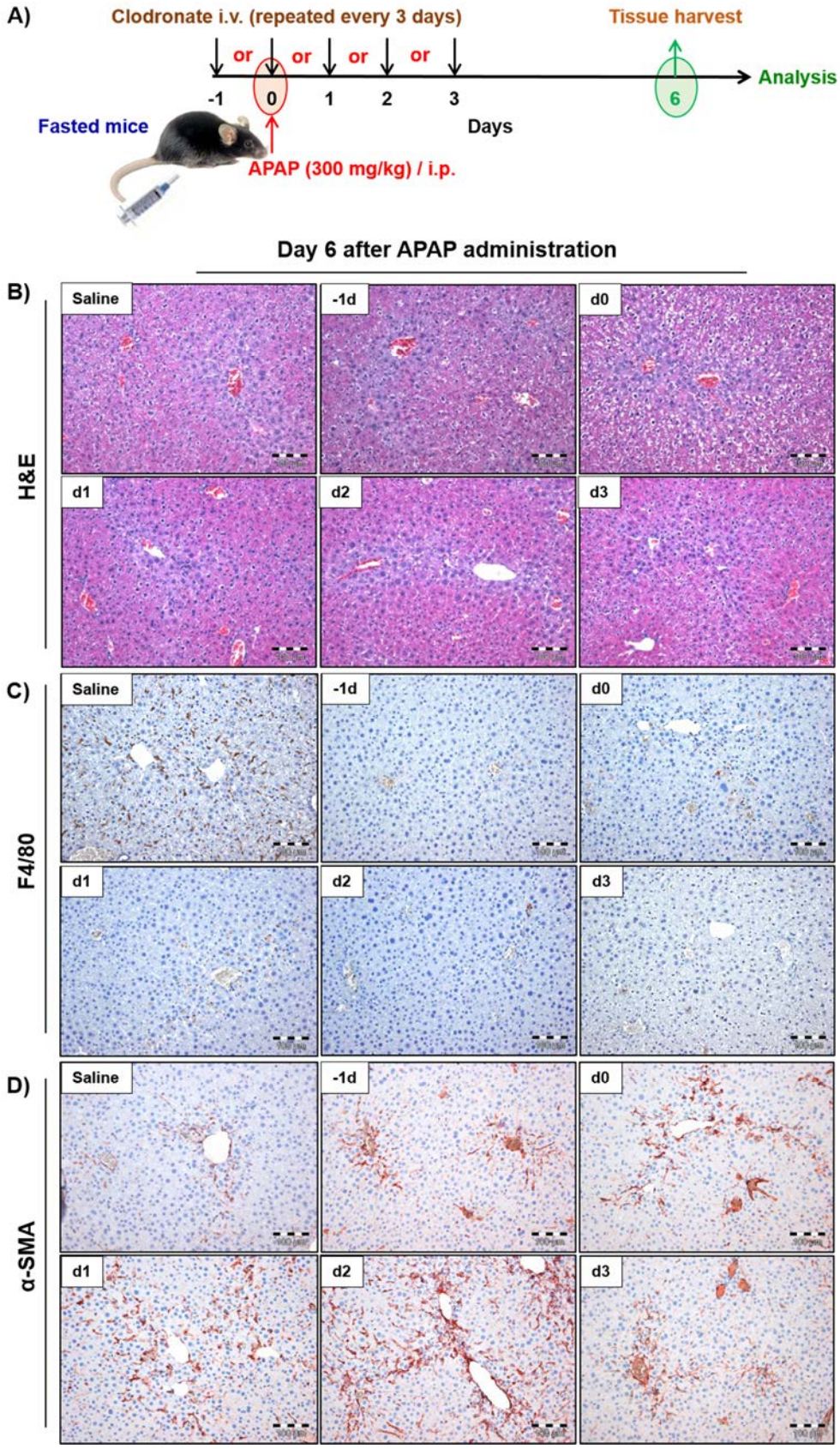

Figure 3. 27: Removal of macrophages is critical for elimination of activated HSCs. (A) Experimental design: mice received i.v. bolus injection of saline or clodronate containing liposomes (50 mg/kg) either before, with or after APAP (300 mg/kg) injection. (B) H&E staining on day 6 after APAP injection showing that the dead cell area is recovered in all treated groups. (C) F4/80 staining showing that clodronate treatment lead to efficient elimination of macrophages. (D) α-SMA staining on day 6 after APAP injection showing massive presence of HSCs after macrophages depletion particularly if clodronate is given on day 2 after APAP administration. Scale bars: 100 µm.

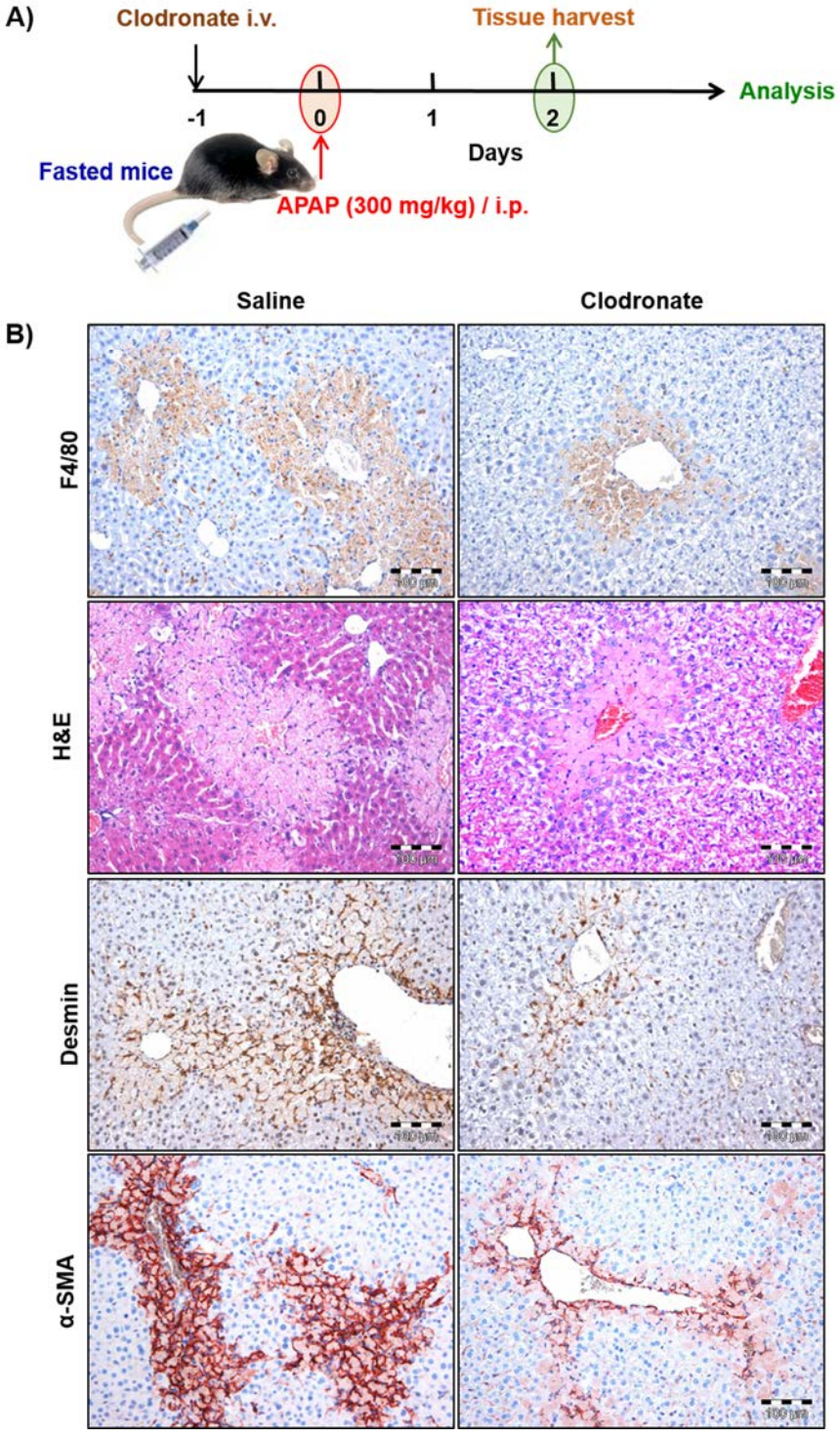

Figure 3. 28: Role of macrophages during the destruction process after APAP injury. (A) Mice were injected i.v. with clodronate (50 mg/kg) or saline one day before APAP treatment (300 mg/kg) followed by liver collection on day 2 after APAP intoxication. (B) The images show that clodronate injection results in macrophages depletion (F4/80) which leads to less liver injury (H&E) and less stellate cells activation (desmin and α-SMA). Scale bars: 100 µm.

Before proceeding to the next step, another control experiment was performed in order to check whether clodronate treatment has a direct effect on HSCs. For this purpose a group of healthy mice were repeatedly injected with clodronate every 3 days followed by liver collection on day 8 (figure 3.29A). As expected, only quiescent HSCs homogenously distributed in the liver lobule were delectable as evidenced by desmin positive and α-SMA negative staining (figure 3.29B). F4/80 staining showed that clodronate treatment successfully depleted macrophages (figure 3.29B).

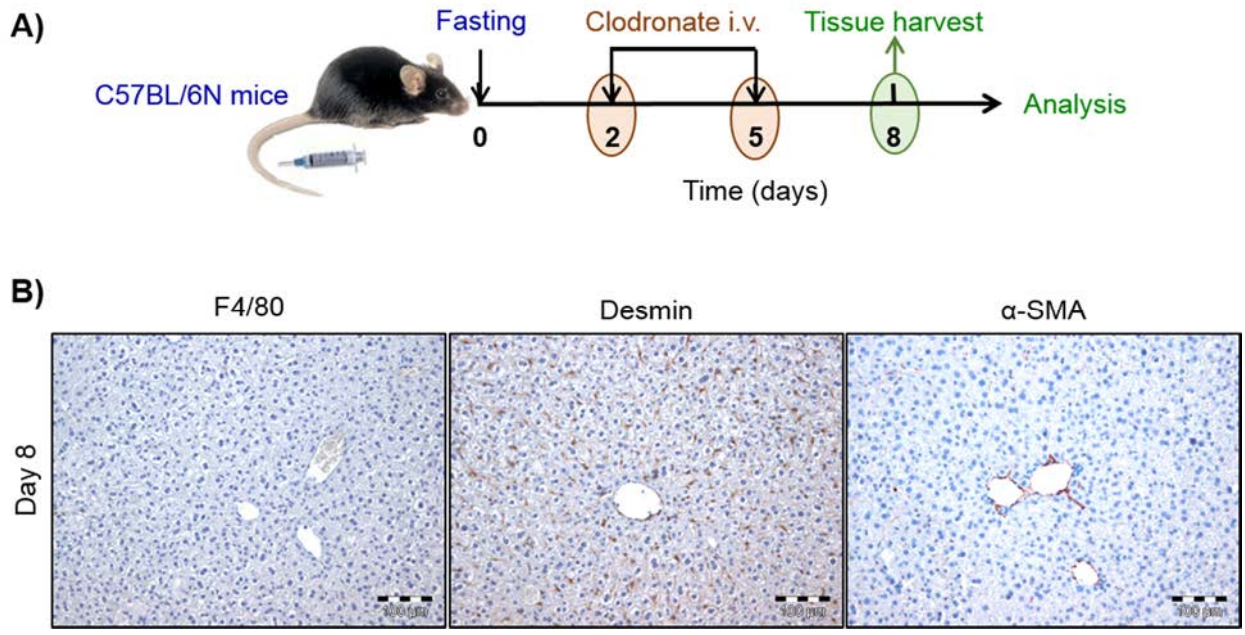

Figure 3. 29: Clodronate administration has no direct effect on HSCs. (A) Mice were overnight fasted, two days later clodronate (50 mg/kg) was injected i.v. repeatedly every 3 days followed by liver collection on day 8. (B) F4/80 immunostaining showing that the liver is free from macrophages after clodronate treatment. Desmin staining shows the normal distribution of quiescent HSCs (α-SMA negative) in the liver lobule. Scale bars: 100 µm.

Based on the results of the previous preliminary trials, an experiment was designed to study the role of macrophages in elimination of activated HSCs. APAP pretreated mice were injected repeatedly with clodronate containing liposomes every three days, started on day 2 after APAP injection. Liver tissue samples were collected on days 2, 4, 8, 12 and 16 after APAP administration (figure 3.30A). As already shown in previous experiments, massive activation and infiltration of HSCs into the dead cell area was observed on day 2 after APAP injection (figure 3.30B).

Clodronate treatment lead to efficient macrophage depletion at all tested time periods as shown by F4/80 negative staining (figure 3.31). In contrast, in saline treated mice, massive macrophage infiltration into the pericentral compartment of the liver lobule was detected on day 4 after APAP administration (figure 3.31). However, both saline as well as clodronate treated mice showed efficient recovery of the dead cell area between days 4 and 8 after APAP intoxication (figure 3.32). In order to investigate the impact of macrophages depletion on HSCs elimination, liver tissue sections were immunostained using antibodies against desmin as well as α-SMA. A very low number of activated HSCs was detected on day 4 after APAP administration in the saline treated mice and completely disappeared by day 8 (figures 3.33 and 3.34). In contrast, massive presence of activated HSCs in the pericentral compartment was detected in the clodronate treated mice on day 4 after APAP administration (figures 3.33 and 3.34). This was associated with slight deposition of ECM particularly on days 4 and 8 after APAP intoxication (figure 3.34). However, this effect was transient and the activated HSCs as well as ECM were slowly eliminated between days 8 and 12 after APAP injection (figures 3.33 and 3.34). In conclusion, removal of macrophages leads to delayed elimination of HSCs after APAP-induced acute liver injury.

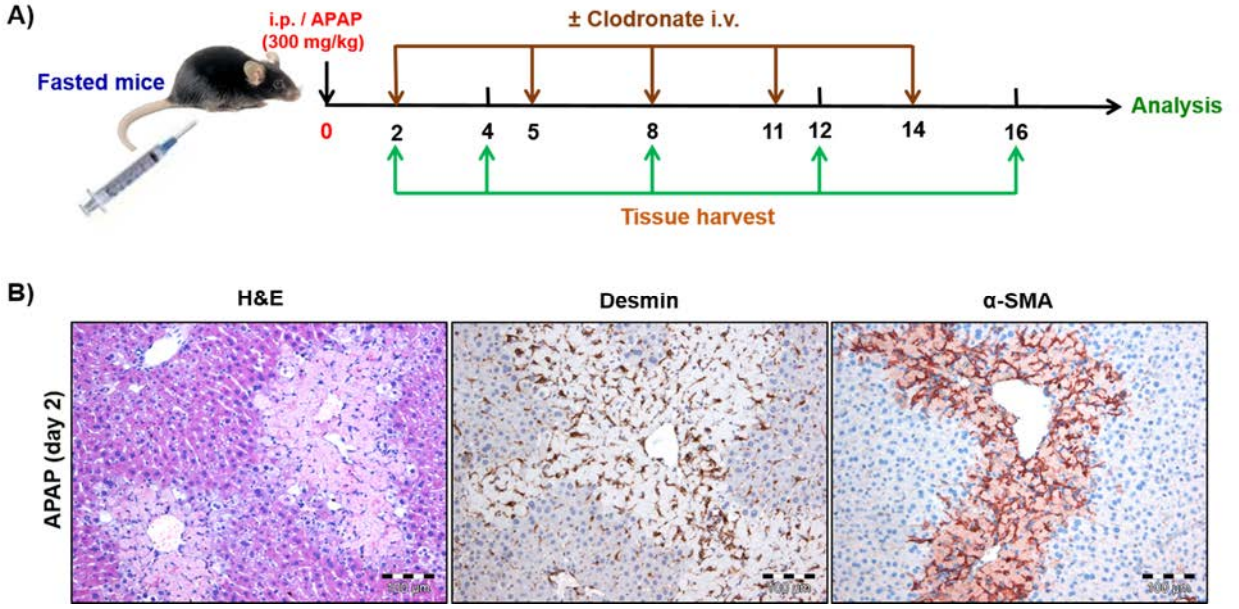

Figure 3. 30: Depletion of restorative macrophages after injection of 300 mg/kg APAP. (A) Experimental design: mice received APAP (300mg/kg). Two days later, the mice were injected with clodronate (50 mg/kg) repeatedly every 3 days. The livers of 3 mice were collected on days 2, 4, 8, 12 and 16 after APAP administration. (B) Day 2 after APAP intoxication showing massive activation (desmin, α-SMA) and infiltration of HSCs into the dead cell area (H&E). Scale bars: 100 µm.

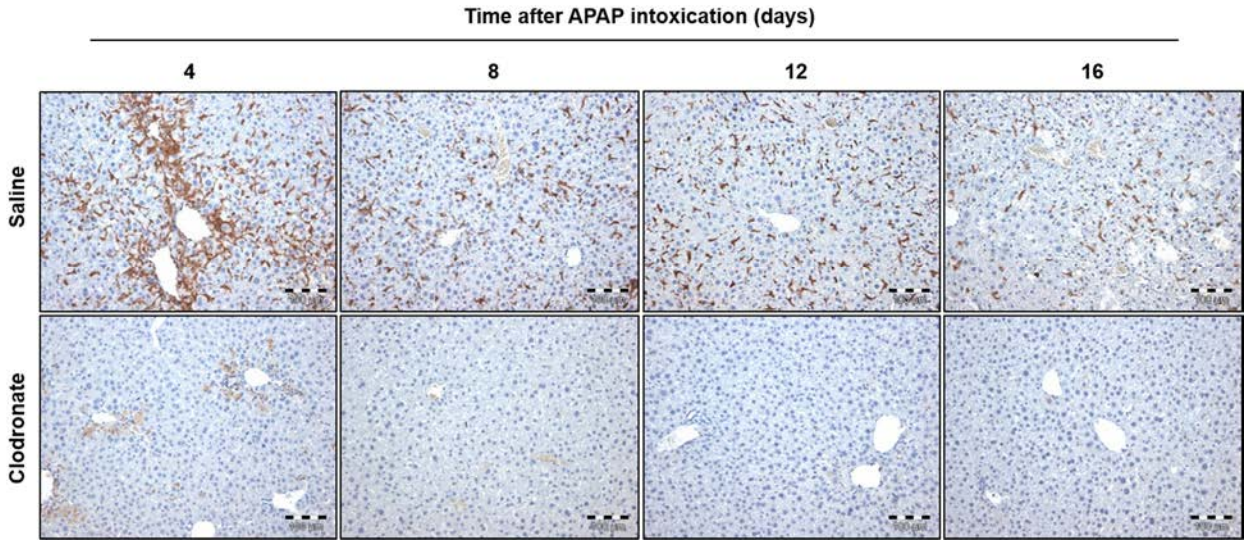

Figure 3. 31: F4/80 immunostaining of liver tissue sections at different time intervals after treatment with APAP ± clodronate. The images show that clodronate treatment leads to efficient depletion of macrophages. Scale bars: 100 µm.

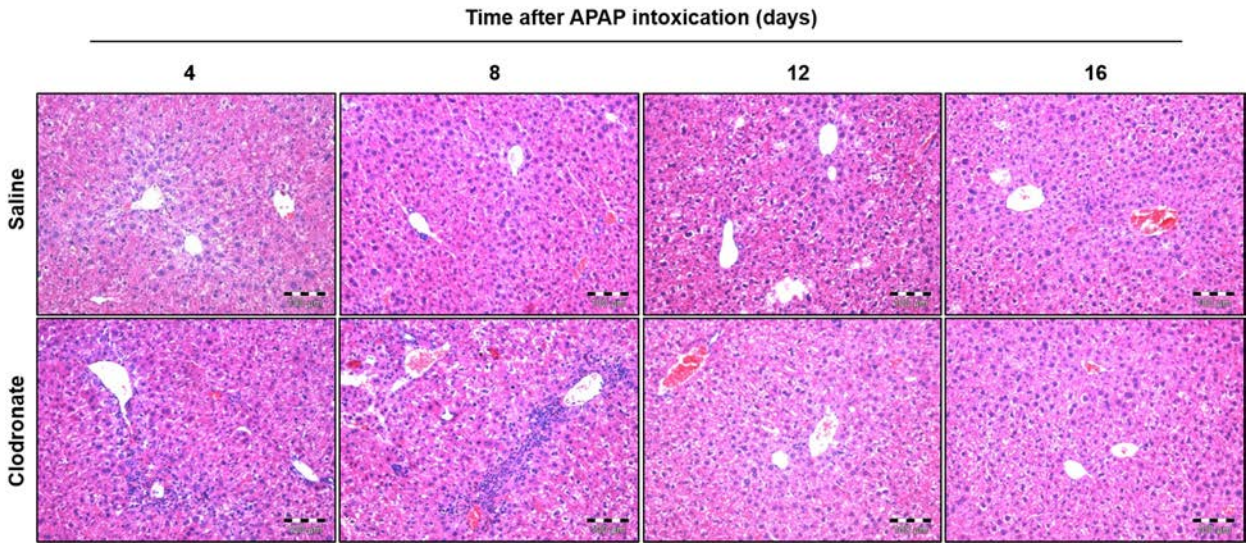

Figure 3. 32: Hematoxylin and eosin staining of liver tissue sections at different time intervals after treatment with APAP ± clodronate. The images show that clodronate treatment has no influence on the recovery of the dead cell area. The dead cell area is restored both in saline as well as clodronate treated mice. Scale bars: 100 µm.

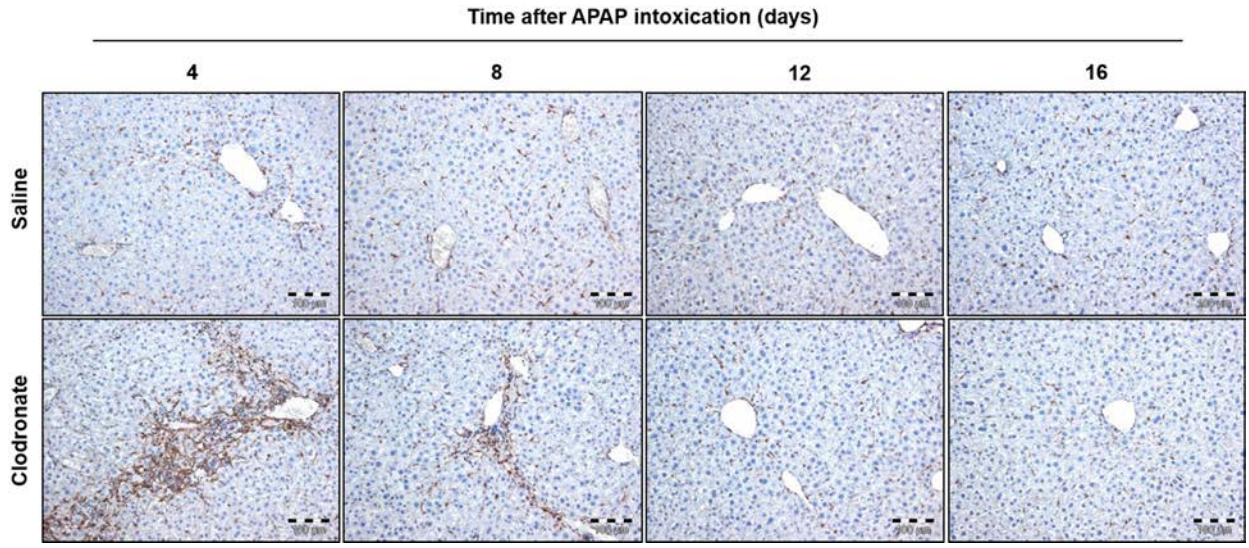

Figure 3. 33: Desmin immunostaining in liver tissue sections at different time intervals after treatment with APAP ± clodronate. Depletion of macrophages by clodronate treatment leads to prolonged accumulation of HSCs in the pericentral area of the liver lobule. Scale bars: 100 µm.

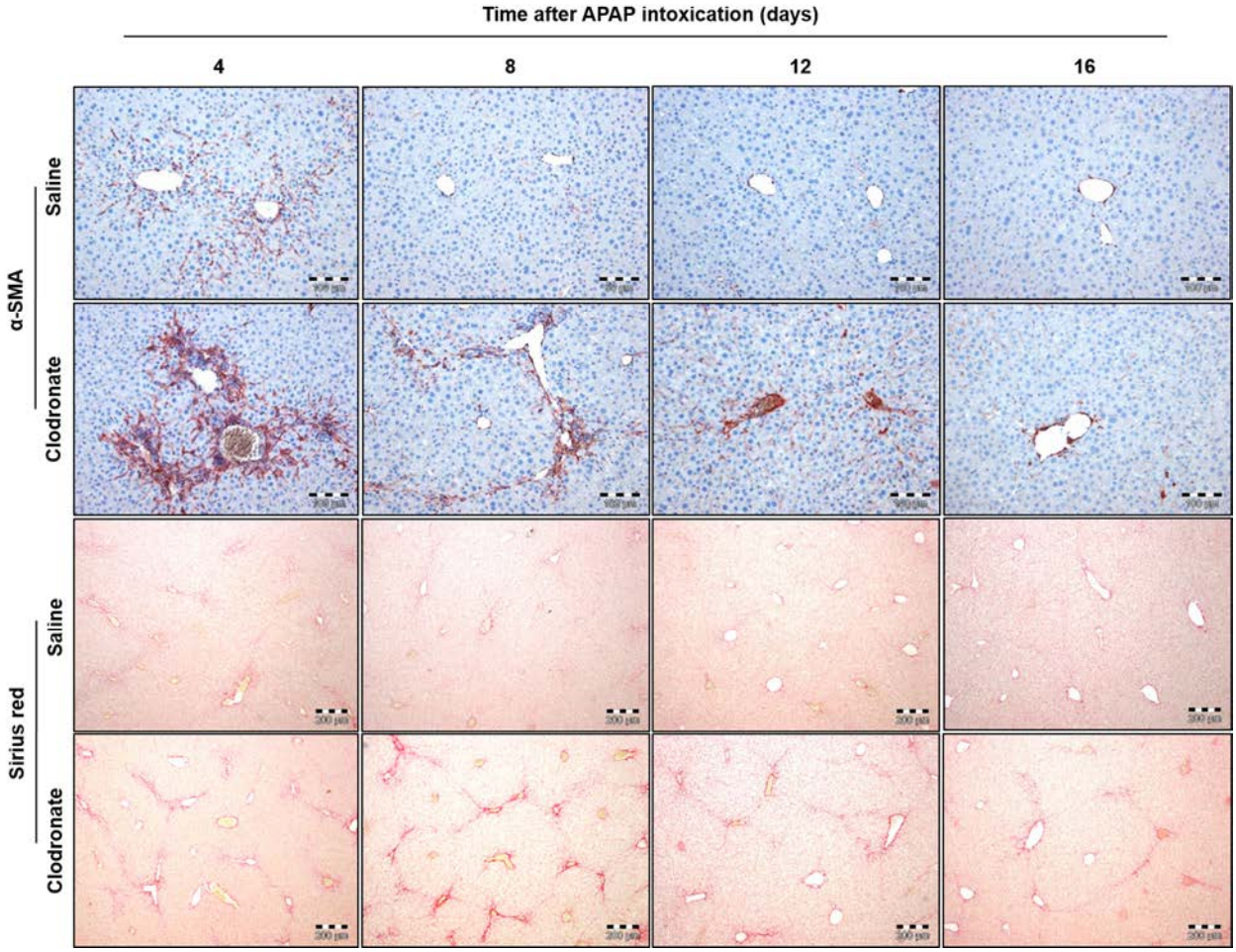

Figure 3. 34: Alpha smooth muscle actin and picrosirius red staining of mouse liver tissue sections at different time intervals after treatment with APAP ± clodronate. Macrophages depletion by clodronate leads to prolonged presence of activated HSCs and slight deposition of extracellular matrix (ECM) in the pericentral compartment of the liver lobule. However, both activated as well as ECM disappear slowly between days 4 and 16. Scale bars: 100 µm.

3.6 Identification of backup mechanisms for elimination of activated HSCs

In the next step, the mechanism of elimination of activated HSCs in the absence of macrophages was investigated. First, we checked whether there was a reversion of activated HSCs to a quiescent phenotype. For this purpose, liver tissue sections from both saline as well as clodronate treated mice were co-stained using antibodies against desmin and α-SMA. As shown in previous experiments, low numbers of activated HSCs were detected in the pericentral compartment of the liver lobule on day 4 after APAP injection (α-SMA positive, desmin positive, figure 3.24A). After day 4, only the basal level of quiescent HSCs was observed distributed all over the liver lobule (α-SMA negative, desmin positive), (figure 3.35). Similarly, in clodronate treated mice, there was no evidence of reversion of activated HSCs to the quiescent state despite of the prolonged accumulation in the pericentral compartment of the liver lobule (figure 3.35).

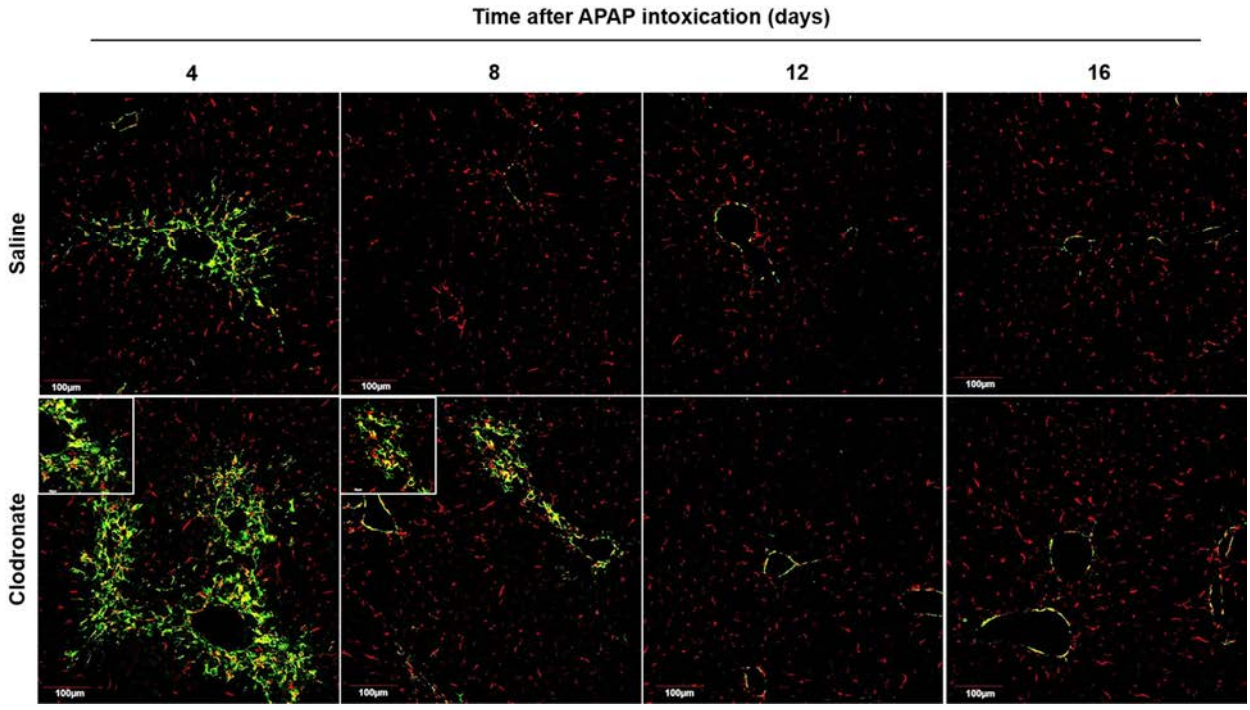

Figure 3. 35: Co-staining of desmin (red) and α-SMA (green) at different time intervals after treatment with APAP ± clodronate. The images show that activated HSCs are eliminated both in saline as well as clodronate treated mice without reversion to the quiescent state. However, removal of activated HSCs takes longer time in clodronate treated mice. Scale bars: 100 µm.

Another hypothesis was that activated HSCs undergo apoptosis in the absence of macrophages, perhaps triggered by other infiltrating immune cells. To validate this hypothesis, TUNEL staining was performed in saline as well as clodronate treated mice. TUNEL positive signal was not detectable in the saline treated mice at all tested time periods (figure 3.36). Interestingly, following macrophage removal by clodronate treatment massive apoptosis of HSCs was observed, particularly on days 4 and 8 after APAP intoxication. Apoptosis of HSCs was confirmed by co-localization of TUNEL and desmin staining (figure 3.36). In order to confirm these interesting findings, another mouse model was used in which acute liver injury was induced by administration of the hepatotoxic compound CCl_4 (1.6 g/kg). Macrophages were depleted by i.v. administration of clodronate on day 3 after CCl_4 injection and liver tissue sections were collected on days 5 and 6 after CCl_4 administration for analysis. Similar to the APAP model, removal of macrophages lead to prolonged presence of activated HSCs after recovery of the dead cell area (figure 3.37). This was also not associated with reversion of activated HSCs to a quiescent state as evidenced by desmin and α-SMA co-staining (figure 3.38A). In accordance with the APAP model, a relatively a high number of apoptotic HSCs were detected on day 6 after CCl_4 intoxication in the absence of macrophages (figure 3.38B). In conclusion, in absence of macrophages a less efficient apoptosis dependent mechanism is triggered to eliminate activated HSCs after acute liver injury. This stimulated me to investigate the trigger of the observed apoptotic mechanism. Can apoptosis of activated HSCs be induced by other infiltrating immune cells? In order to obtain an overview about the presence of infiltrating leukocytes, liver tissue sections from the clodronate treated mice were immunostained using antibodies against CD45; a pan leukocytes marker. Interestingly, massive leukocyte infiltration was observed between days 4 and 8 after APAP administration, the time when activated HSCs were eliminated (figure 3.39). These CD45 positive cells were arranged in clusters at the pericentral compartment of the liver lobule. Since these cells were negative for F4/80, they were not macrophages (figure 3.31B). In order to identify these infiltrating immune cells, tissue sections were immunostained using antibodies against B220 (a B cell marker), CD3 (a T cell marker) and LY6G (a marker of neutrophils). The results revealed that a significant fractions of these cell clusters were positive for B220 and CD3 indicating infiltration of B

and T cells, respectively (figures 3.40 and 3.41). LY6G staining showed no significant neutrophils infiltration both in clodronate as well as saline treated mice (figure 3.42). For further confirmation and identification of these infiltrating immune cells, a group of APAP treated mice were injected with clodronate or saline on day 2 and the liver was collected and homogenized on day 4 after APAP intoxication. Immune cells were isolated and prepared for flow cytometry analysis by staining with fluorescently labeled antibodies against CD45, CD3, CD4, CD8, NK cells, natural killer T (NKT) cells, B cells and dendritic cells. In accordance with the immunostaining results, clodronate treated mice showed higher CD45 positive cell numbers in comparison to the saline group (figure 3.43A). Further identification of these cells showed higher numbers of B, T, NK, NKT and dendritic cells in clodronate treated mice in comparison to the saline group (figure 3.43B). Finally, I investigated whether these findings are reproducible in another model of acute liver injury. Therefore, similar experiments were performed after administration of a single dose of CCl_4 (1.6 g/kg). The mice were treated with clodronate or saline on day three after CCl_4 administration and the livers were collected on days 5 and 6 for analysis. Similar to the results after APAP intoxication, clusters of CD45 positive, F4/80 negative immune cells were detected in the livers of clodronate treated mice (figure 3.44). Furthermore, significant fractions of these cells were B cells as evidenced by B220 immunostaining (figure 3.44). In conclusion, elimination of macrophages during liver regeneration following an acute challenge stimulates immune cells infiltration, particularly B, T, NK and dendritic cells, which might trigger the killing and elimination of activated HSCs.

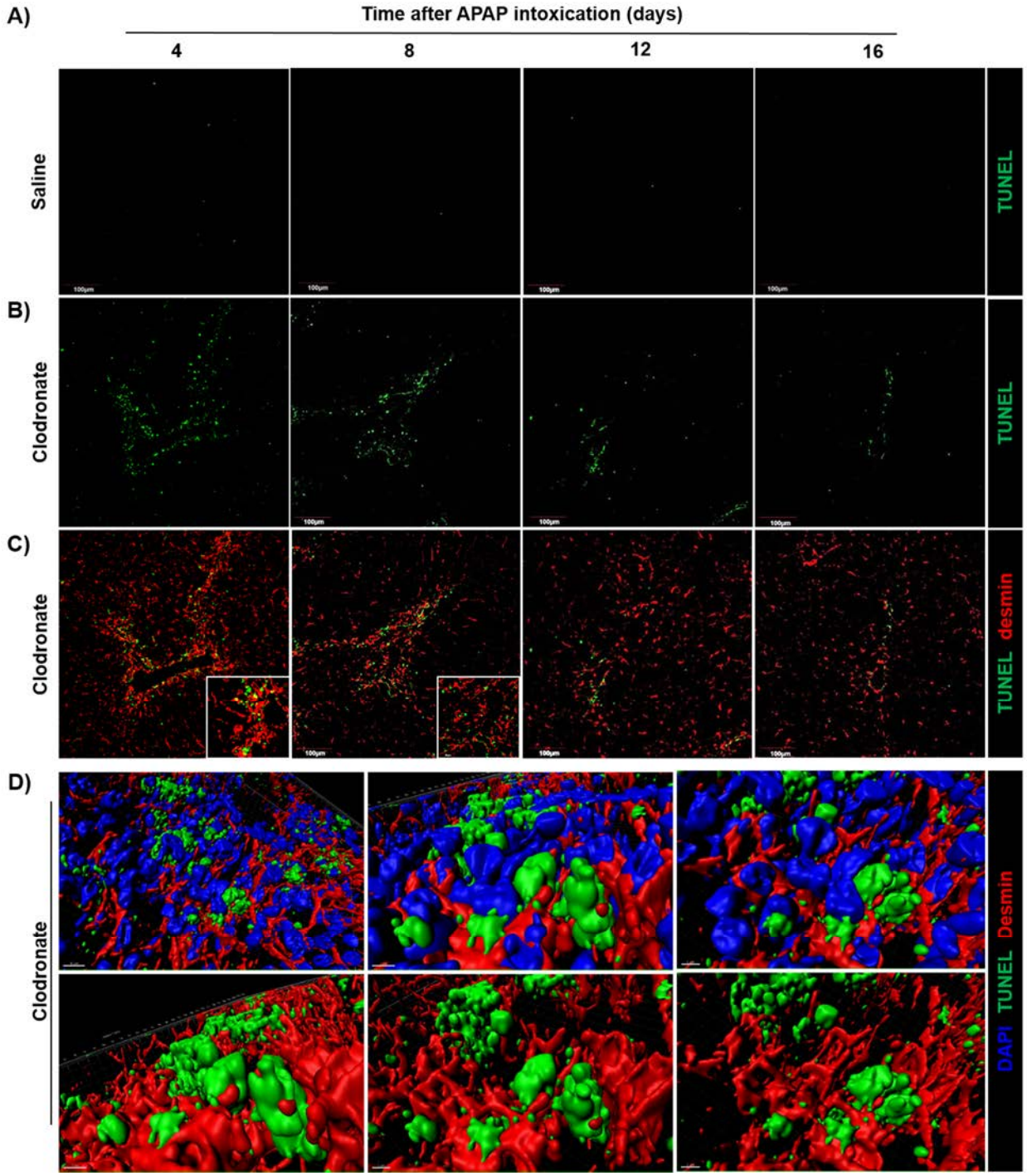

Figure 3. 36: Activated HSCs are eliminated by apoptosis after macrophage depletion during liver regeneration. Liver tissue sections stained with TUNEL at different time periods after administration of APAP ± clodronate. (A) Saline treated mice showing TUNEL negative staining. (B) Clodronate treated mice showing massive apoptosis in the pericentral compartment of the liver lobule particularly on days 4 and 8 after APAP intoxication. (C) Co-staining of TUNEL and desmin in clodronate treated mice confirming apoptosis of HSCs. Scale bars: 100 µm. (D) 3D reconstructions of desmin and TUNEL staining on day 4 after APAP intoxication in clodronate treated mice showing a lot of apoptotic HSCs.

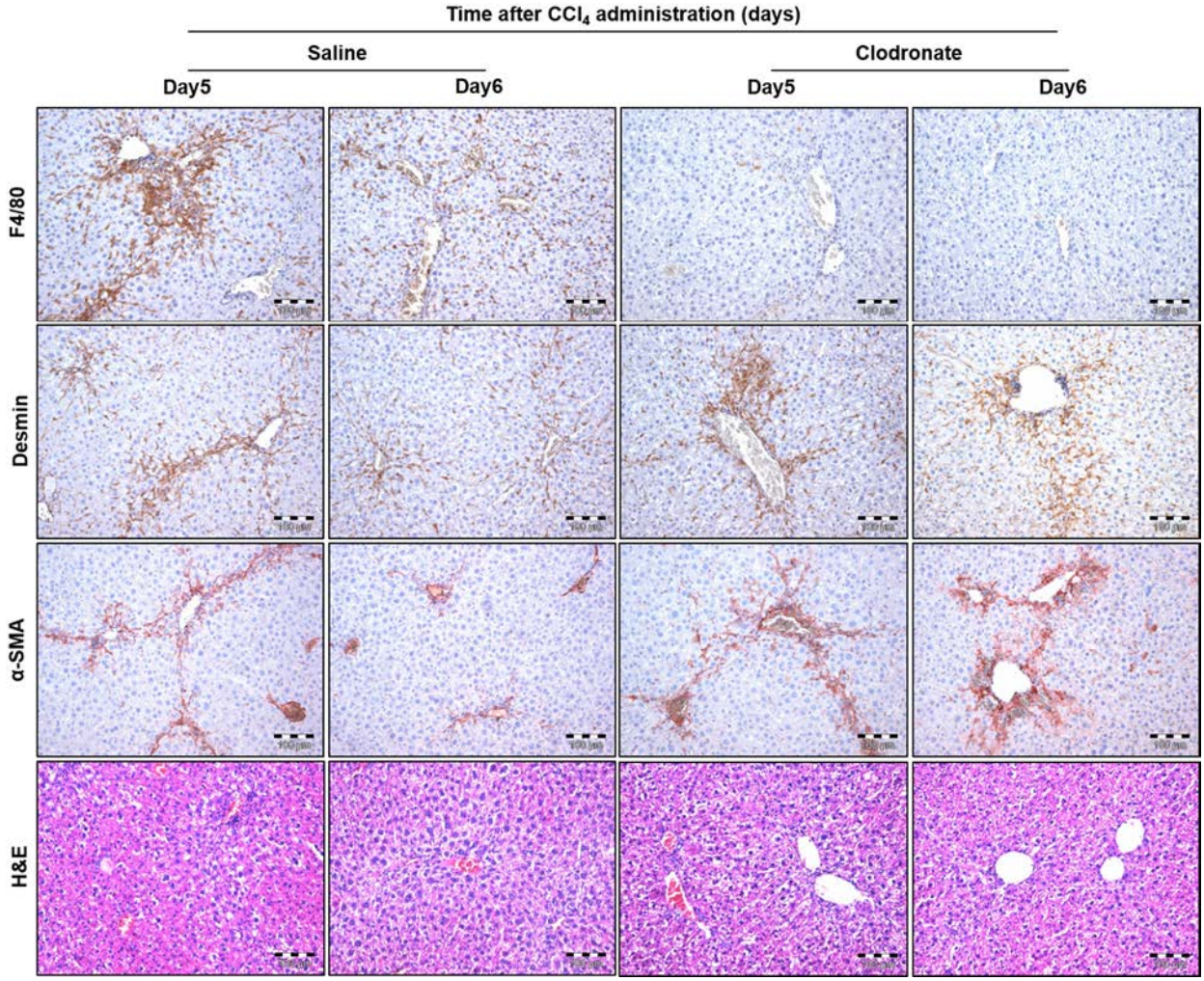

Figure 3. 37: Prolonged presence of activated HSCs after macrophage depletion. Mice were intoxicated with a single dose of CCl_4 (1.6 g/kg) and received an i.v. injection of clodronate (50 mg/kg) or saline on day 3 after CCl_4 administration. Immunostaining of F4/80 on days 5 and 6 after CCl_4 intoxication shows the infiltration of macrophages into the pericentral compartment of the liver lobule in saline treated mice. In contrast, the liver appears almost free of macrophages after clodronate treatment. Immunostaining of desmin as well as α-SMA show prolonged presence of the activated HSCs in the absence of macrophages, although the dead cell area is recovered both in the saline as well as in the clodronate treated mice (H&E). Scale bars: 100 µm.

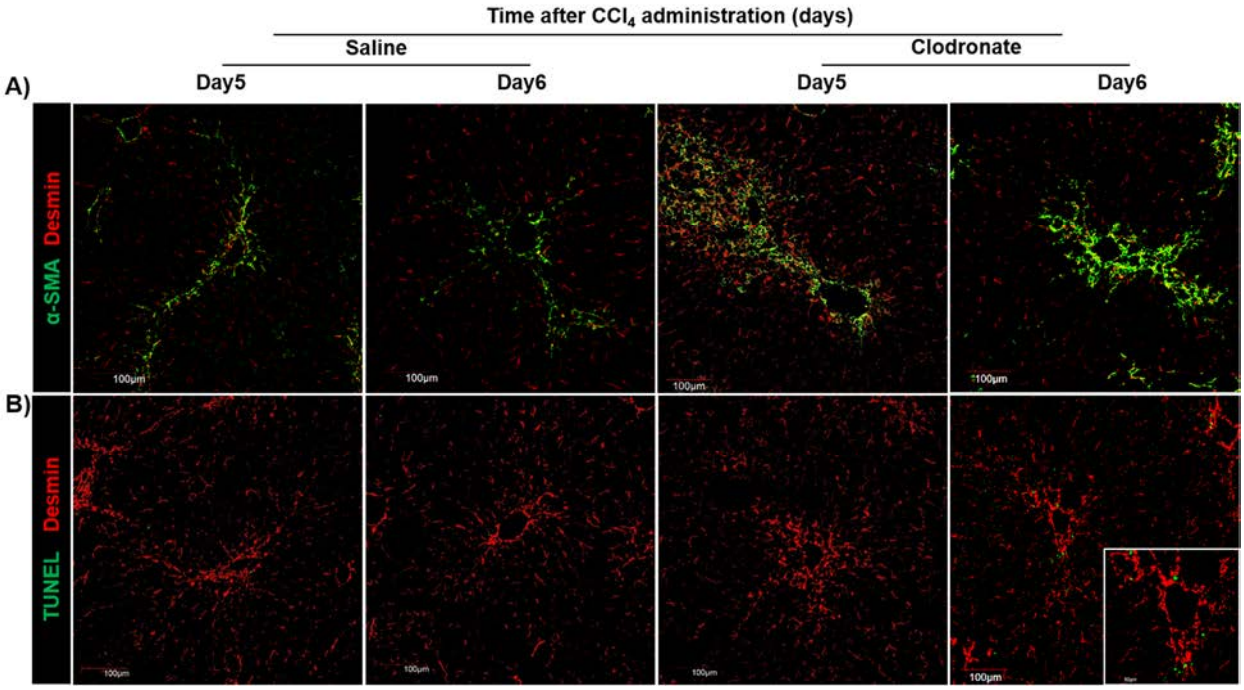

Figure 3. 38: Activated HSCs are slowly eliminated by apoptosis in the absence of macrophages after acute liver injury. Mice are intoxicated with a single dose of CCl_4 (1.6 g/kg) and received an i.v. injection of clodronate (50 mg/kg) or saline on day 3 after CCl_4 administration. (A) Desmin and α-SMA co-staining showing that there is no reversion of HSCs from the active to the quiescent state neither in absence nor in presence of macrophages. (B) TUNEL and desmin co-staining showing a lot of apoptotic HSCs on day 6 after CCl_4 intoxication in the absence of macrophages (clodrontae treated mice). Scale bars: 100 µm.

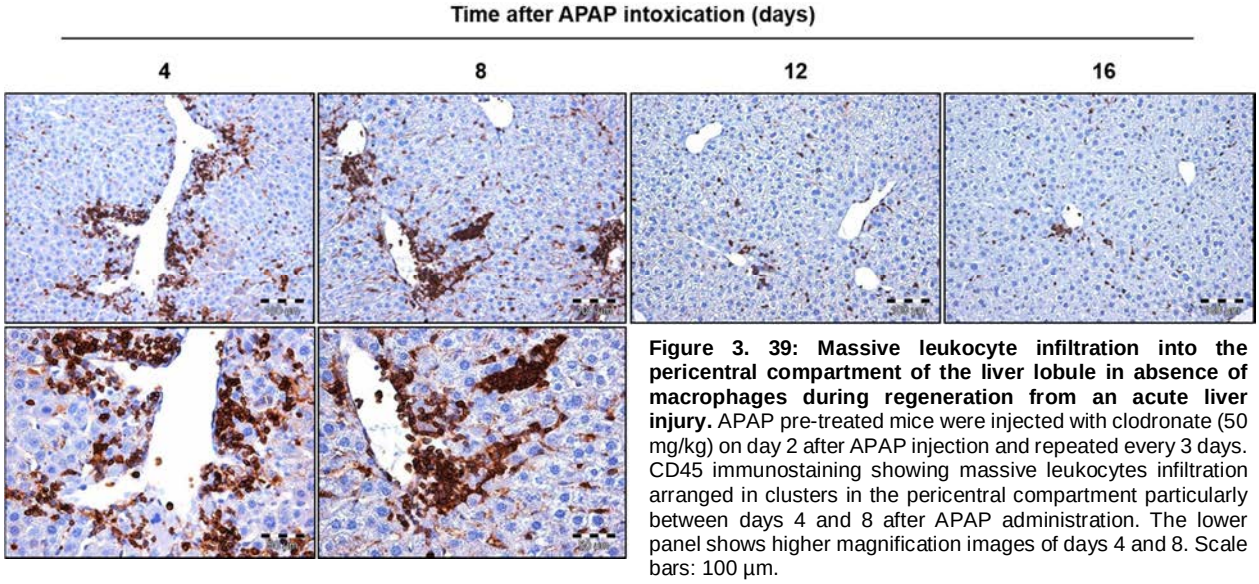

Figure 3. 39: Massive leukocyte infiltration into the pericentral compartment of the liver lobule in absence of macrophages during regeneration from an acute liver injury. APAP pre-treated mice were injected with clodronate (50 mg/kg) on day 2 after APAP injection and repeated every 3 days. CD45 immunostaining showing massive leukocytes infiltration arranged in clusters in the pericentral compartment particularly between days 4 and 8 after APAP administration. The lower panel shows higher magnification images of days 4 and 8. Scale bars: 100 µm.

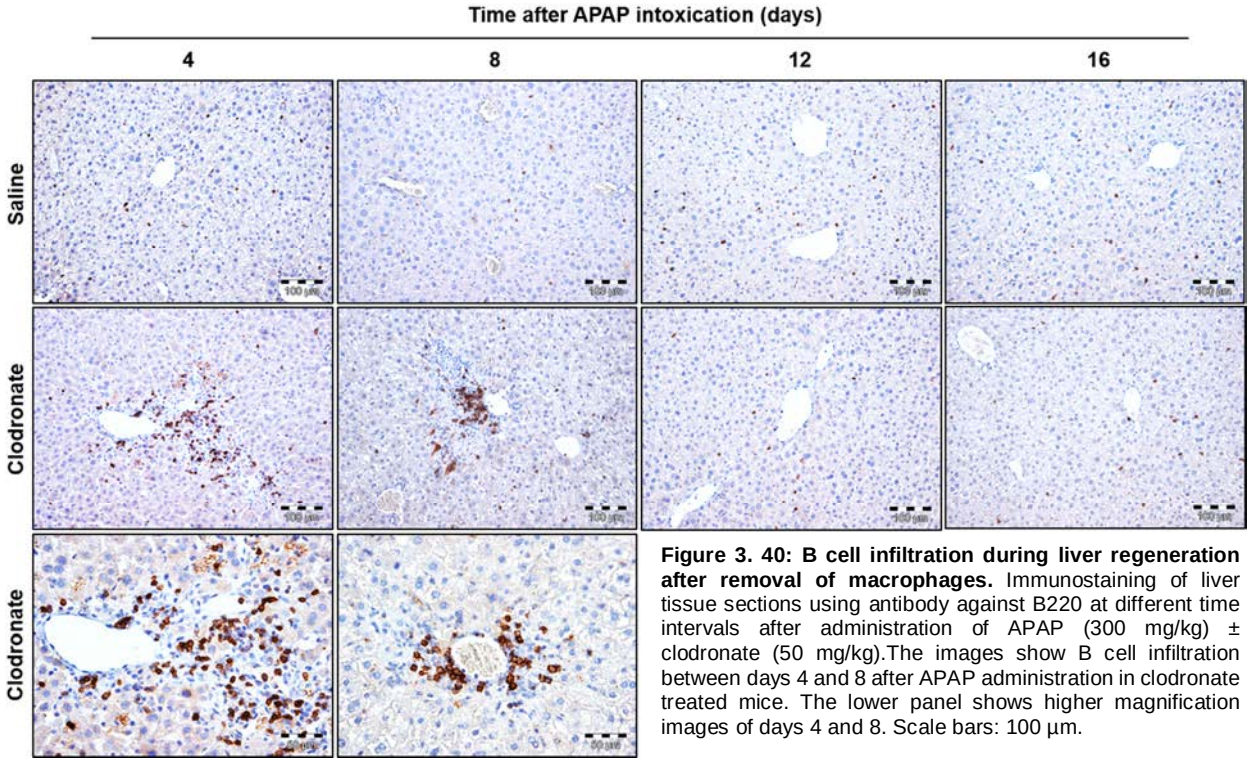

Figure 3. 40: B cell infiltration during liver regeneration after removal of macrophages. Immunostaining of liver tissue sections using antibody against B220 at different time intervals after administration of APAP (300 mg/kg) ± clodronate (50 mg/kg).The images show B cell infiltration between days 4 and 8 after APAP administration in clodronate treated mice. The lower panel shows higher magnification images of days 4 and 8. Scale bars: 100 µm.

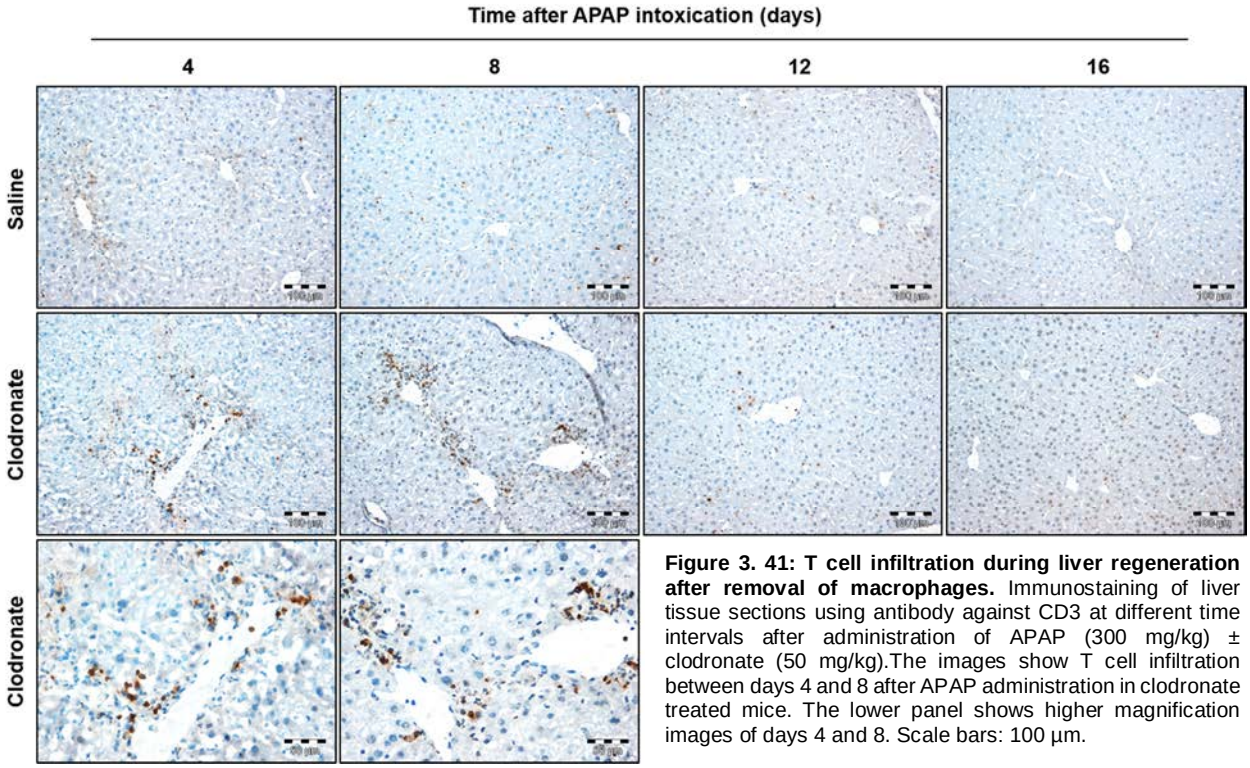

Figure 3. 41: T cell infiltration during liver regeneration after removal of macrophages. Immunostaining of liver tissue sections using antibody against CD3 at different time intervals after administration of APAP (300 mg/kg) ± clodronate (50 mg/kg).The images show T cell infiltration between days 4 and 8 after APAP administration in clodronate treated mice. The lower panel shows higher magnification images of days 4 and 8. Scale bars: 100 µm.

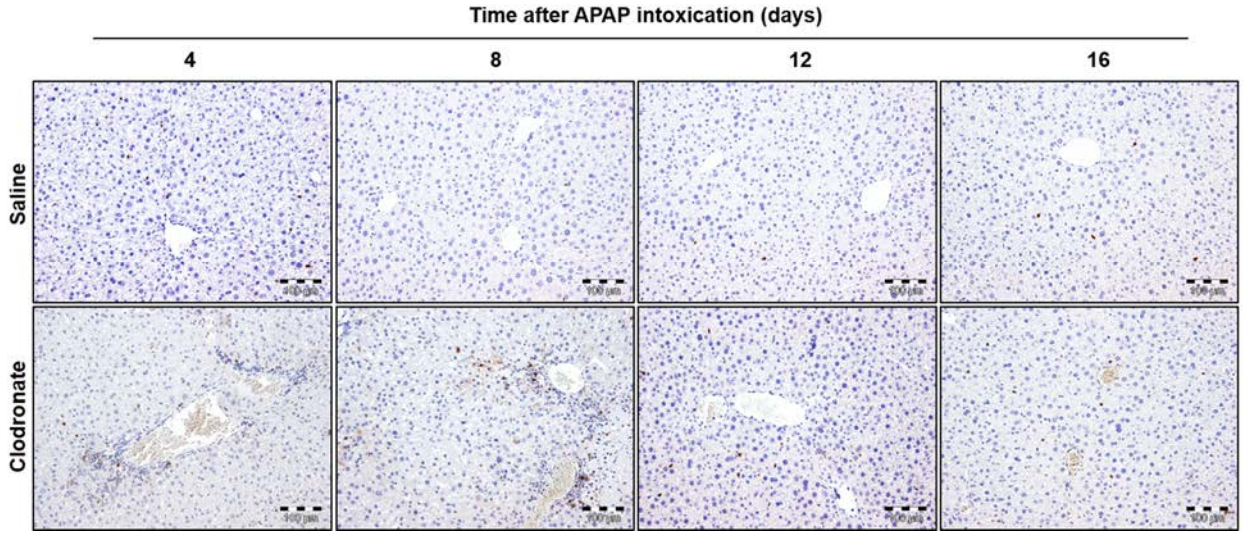

Figure 3. 42: Neutrophils do not contribute to elimination of activated HSCs during liver regeneration. Liver tissue sections from mice treated with APAP ± clodronate were immunostained using antibodies against LY6G. The images show very few infiltrating neutrophils both in saline as well as clodronate treated mice. Scale bars: 100 µm.

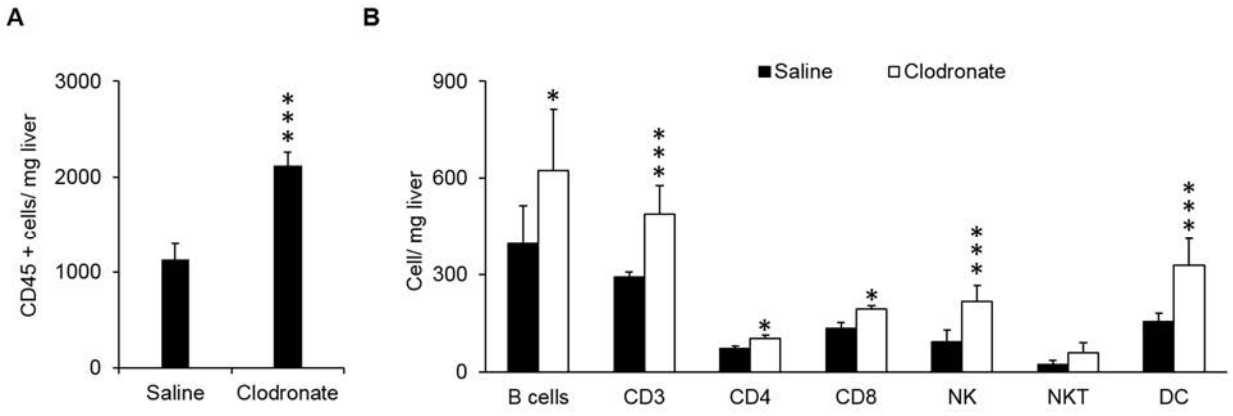

Figure 3. 43: Flow cytometry analysis of infiltrating leukocytes in liver tissues of APAP ± clodronate treated mice on day four after APAP injection. (A) CD45 positive cells showing more leukocytes in the livers of clodronate treated in comparison to saline treated mice. These cells are a mixture of B, T, NK, NKT and dendritic cells (B). Data are means ± SD of six mice. ***p<0.001, *p<0.05 when compared to the corresponding control (saline) group.

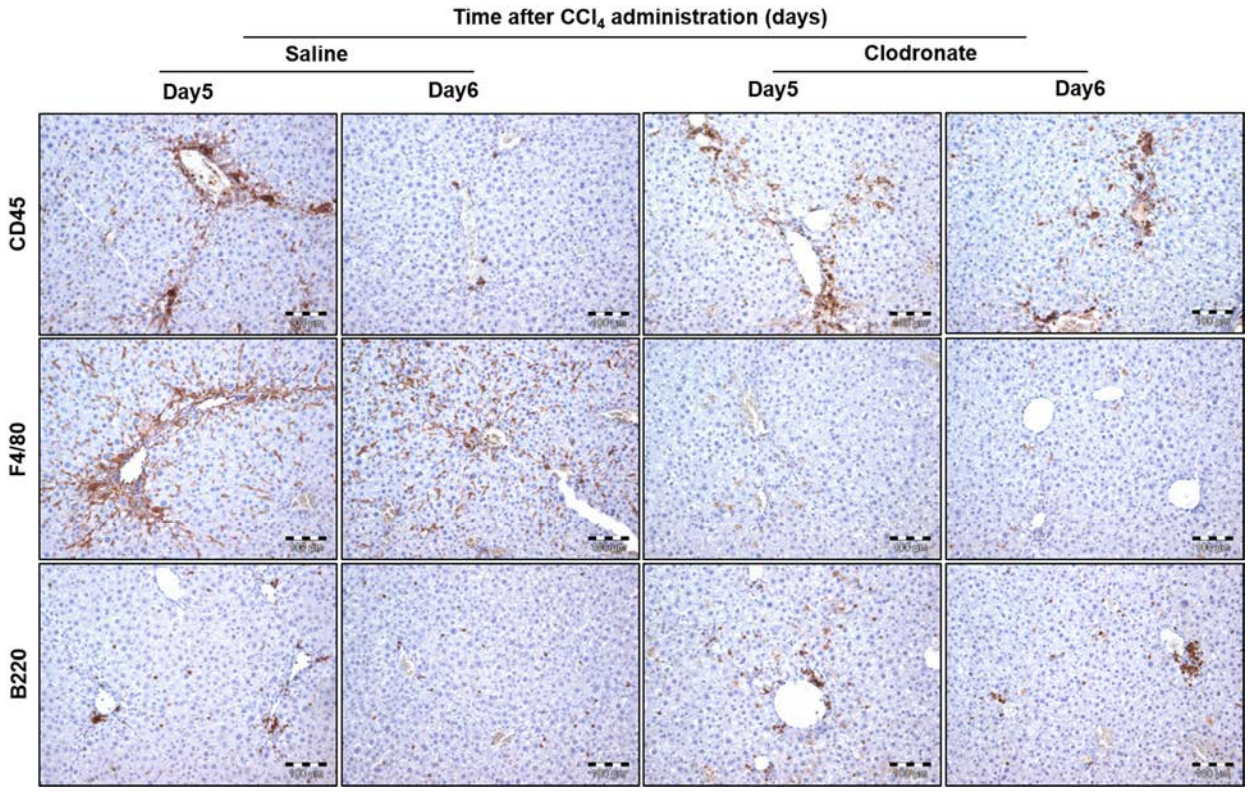

Figure 3. 44: Leukocytes infiltration during liver regeneration after CCl_4 intoxication and depletion of macrophages. The images show leukocytes infiltration (CD45 positive) particularly B cell (B220 positive) in clodronate treated mice. F4/80 staining shows massive macrophages infiltration into the pericentral compartment of the liver lobule of the saline treated group. Scale bars: 100 µm.

4. Discussion

Unexpected findings of this thesis are: (1) massive activation of HSCs and infiltration into the dead cell area following acute liver injury, (2) activation of HSCs under these conditions is not associated with fibrosis development but, (3) the activated HSCs are efficiently eliminated by macrophages following recovery of the dead cell area, (4) removal of macrophages activate backup mechanisms for elimination of activated HSCs.

4.1 Similar responses but different consequences of HSCs following acute and chronic liver damage scenarios

It is well known that chronic liver injury leads to activation and trans-differentiation of quiescent HSCs into myofibroblast-like cells (Duffield et al. 2005; Henderson and Iredale 2007; Tacke and Zimmermann 2014). Activation of HSCs results mainly of interaction with $CD11b^{hi}$ $LY6C^{hi}$ pro-inflammatory macrophages which infiltrate the liver tissue during the destruction process following liver intoxication (Baeck et al. 2014; Ju and Tacke 2016; Ramachandran et al. 2012; Zigmond et al. 2014). These pro-inflammatory macrophages produce: (1) TGF-β which activate the resting HSCs into myofibroblast-like cells (Ramachandran and Iredale 2012b; Seki et al. 2007); (2) platelet derived growth factor (PDGF), which stimulate proliferation and migration of HSCs into the site of injury (Tacke and Zimmermann 2014; Wang et al. 2016); and (3) IL-1β and TNF-α which stimulate the NF-kB pathway that maintains survival of activated HSCs (Pradere et al. 2013; Seki and Schwabe 2015) (figure 4.1). Activation of HSCs in case of chronic liver injury leads to production and accumulation of extracellular matrix (ECM) and fibrosis development (Baeck et al. 2014; Ramachandran and Iredale 2012a; Ramachandran and Iredale 2012b) (figures 4.1 and 4.2).

In contrast to chronic liver injury, despite of massive cell killing and activation of HSCs following administration of a single toxic dose of APAP or CCl_4, liver fibrosis was not induced. Instead, perfect liver regeneration was obtained within a week following intoxication (figure 4.1). This suggests that liver fibrosis can develop only after repeated exposure to a hepatotoxic agent until a certain threshold is exceeded. The transient

massive activation of HSCs following acute liver damage may be critical for liver regeneration because: (1) HSCs can engulf apoptotic bodies of damaged hepatocytes which attenuates inflammation and triggers regeneration signals (Weiskirchen and Tacke 2014). The engulfment of apoptotic bodies by HSCs also helps in its activation and stimulates survival pathways (Canbay et al. 2003; Jiang et al. 2009; Zhan et al. 2006). (2) Activated HSCs are known to produce hepatocyte growth factor (Skrtic et al. 1999; Yin et al. 2013), which is a potent hepatocyte mitogen. The present data show that administration of very high doses of APAP (450 mg/kg) lead to weak and delayed activation of HSCs. This was associated with delayed hepatocyte proliferation and compromised liver regeneration. Furthermore, (Shen et al. 2011) have reported that depletion of activated HSCs correlate with severe liver injury and compromised liver regeneration after APAP intoxication. (3) Infiltration of activated HSCs into the dead cell area may serve as a niche that stabilizes the wound until replacement proliferation takes place.

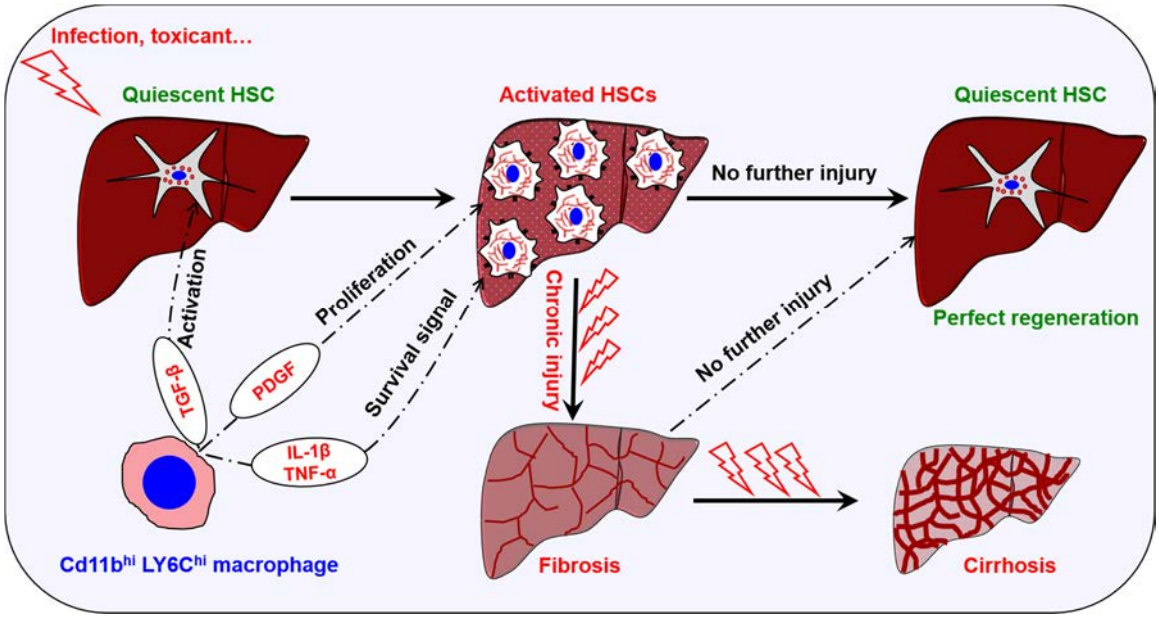

Figure 4. 1: Different consequence to stellate cell activation in case of acute and chronic damage scenarios: following liver injury CD11b^{hi} LY6C^{hi} pro-inflammatory macrophages infiltrate the liver tissue and interact with HSCs via: (1) secretion of TGF-β which induce activation of HSCs; (2) platelet derived growth factor (PDGF), which stimulates proliferation of HSCs; and (3) IL-1β and TNF-α which promote survival of HSCs. After single intoxication the activation of HSCs occurs only transiently and disappears within few days without fibrosis development. In contrast, repeated liver injury leads to prolonged activation of HSCs and excessive deposition of extracellular matrix leading to liver fibrosis which may progress to cirrhosis.

4.2 Different mechanisms are responsible for removal of activated HSCs after acute and chronic damage scenarios

In order to explain the discrepancy between fibrosis induction as a consequence of repeated intoxication and perfect regeneration following single intoxication, the mechanisms of activated HSCs elimination were studied in both scenarios. The present study demonstrates that despite of elimination of activated HSCs following both single (acute) and repeated (chronic) challenges, the responsible mechanisms are different (figure 4.3). Elimination of activated HSCs represents an active process. The responsible mechanisms have been extensively studied during fibrosis regression and include: (1) reversion of activated HSCs to an inactive phenotype (Friedman 2012; Kisseleva et al. 2012; Troeger et al. 2012). However, these cells remain primed and are highly sensitive for rapid fibrogenesis if the injury is repeated (Kisseleva et al. 2012; Mallat and Lotersztajn 2013). (2) Elimination of activated HSCs by apoptosis; the main players are NK cells, which induce killing of HSCs either directly in a TRAIL dependent manner or indirectly via production of IFN-γ (Radaeva et al. 2006; Tian et al. 2013); and the restorative ($CD11b^{hi}$ $LY6C^{lo}$ macrophages), which kill activated HSCs in a TRAIL dependent manner (Ramachandran and Iredale 2012b; Seki and Schwabe 2015; Tacke and Trautwein 2015). In addition, these restorative macrophages are also a rich source of matrix metalloproteinases (MMPs) particularly MMP9, MMP12 and MMP13 which are important for degradation of ECM (Fallowfield et al. 2007; Ramachandran et al. 2012; Seki and Schwabe 2015; Tacke and Zimmermann 2014). (3) A fraction of activated HSCs also undergoes senescence during fibrosis recovery. This results in a phenotype with reduced fibrogenic properties that also more labile to immune cell induced killing (Kim et al. 2013; Krizhanovsky et al. 2008). All these mechanisms could be reproduced under our experimental setup following repeated CCl_4 intoxication (figures 4.2 and 4.3). In contrast, none of these mechanisms were observed during regeneration after acute challenge. However, activated HSCs were rapidly removed. While the peak of HSCs activation can be seen between days 2 and 3 following APAP administration, it takes only until day 6 for all of them to be removed. The elimination of activated HSCs occurred during the time period when macrophages massively infiltrate the pericentral compartment of the liver

lobule. The present findings suggest direct engulfment of living activated HSCs by macrophages. This was supported by prolonged presence of activated HSCs upon macrophages depletion. Direct phagocytosis of living cells by macrophages was previously reported only for cancer cells. (Feng et al. 2015) reported that blocking of CD47 (Do not eat me signal) on tumor cells allows their recognition and direct phagocytosis by macrophages.

In conclusion, these data show that the extent of cell killing and activation of HSCs do not necessarily correlate with fibrosis induction. A balance between fibrotic and anti-fibrotic

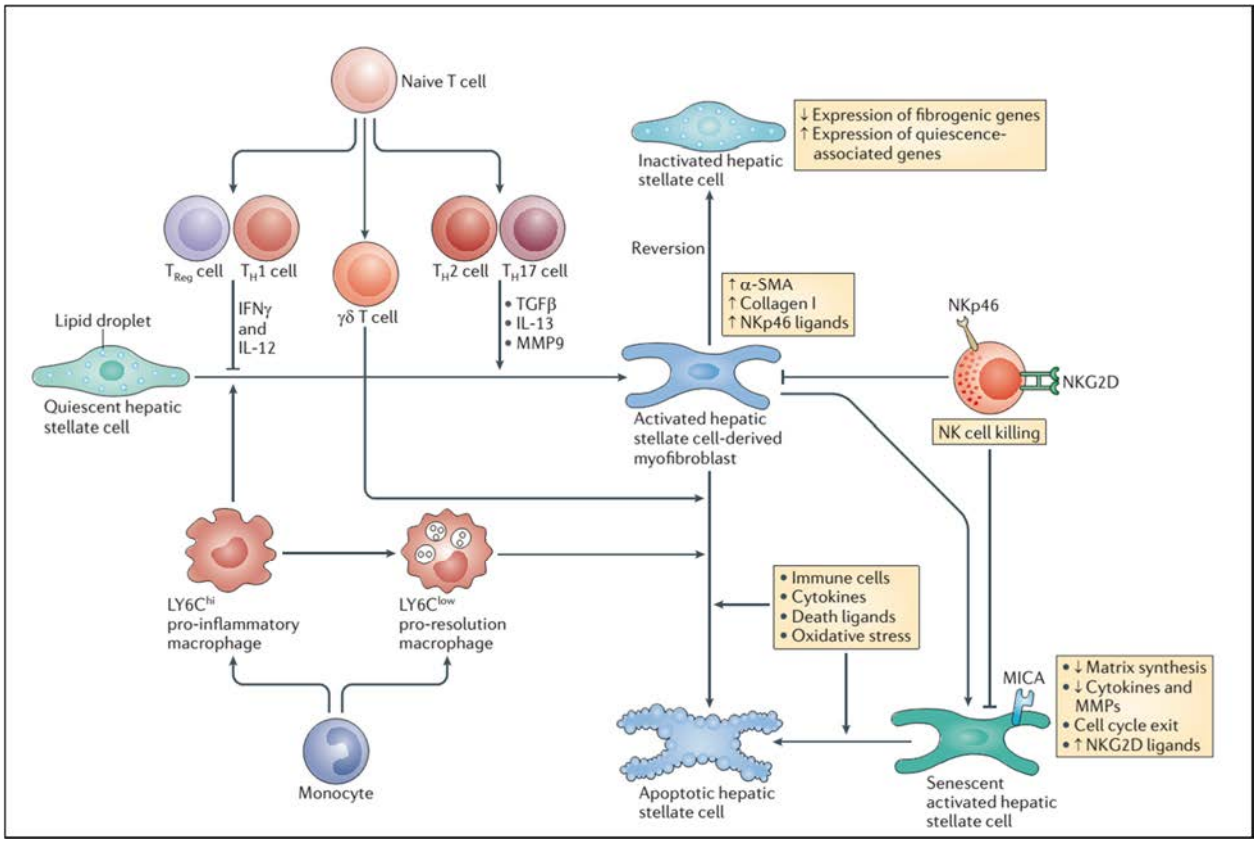

Figure 4. 2: Activation of HSCs during fibrosis progression and their elimination during fibrosis recovery. Following liver injury LY6C^{hi} pro-inflammatory macrophages infiltrate the liver tissue and stimulate activation and proliferation of HSCs. After cessation of liver injury, activated HSCs disappear by reversion to inactive phenotype, apoptosis or senescence then apoptosis. The major cell types which are relevant for elimination of activated HSCs are LY6C^{lo} macrophages, NK cells, dendritic cells and γδ-T cells (Source: Pellicoro et al. 2014).

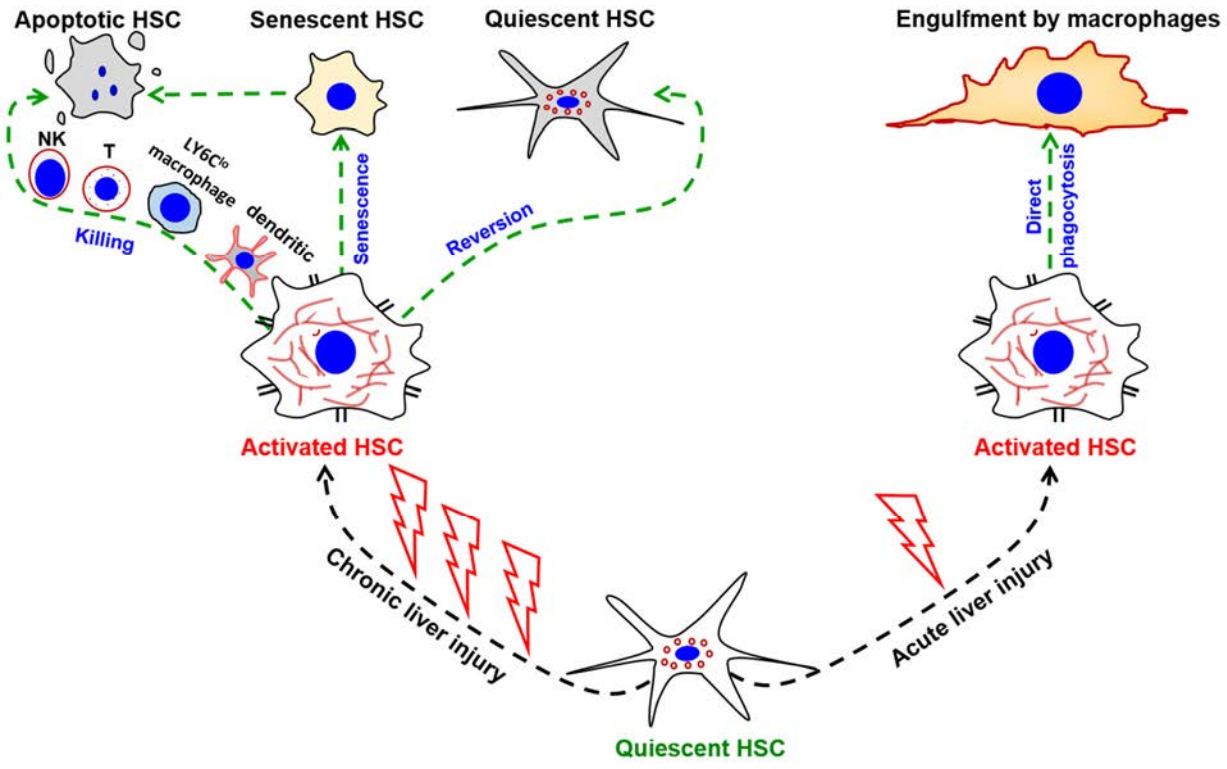

Figure 4. 3: Different mechanisms for elimination of activated hepatic stellate cells (HSCs) after repeated (chronic) and single (acute) liver injury. After single or repeated liver injury HSCs get activated and become myofibroblast-like cells that produce excessive amount of extracellular matrix. However, after cessation of liver injury, activated HSCs are eliminated by different mechanisms. During fibrosis recovery, a fraction of activated HSCs reverts back to the quiescent state; another fraction undergoes apoptosis (the main players are NK cells, γδ-T cells, restorative macrophages and dendritic cells) and a third fraction first undergoes senescence and then becomes apoptotic. In contrast, during regeneration from a cute challenge, activated HSCs are eliminated via direct engulfment by macrophages.

4.3 Identification of backup mechanisms of activated HSCs elimination

The present data revealed that activated HSCs are eliminated actively via direct engulfment by macrophages during liver regeneration after acute challenge. This is a very efficient process, since it does not allow ECM deposition. Elimination of macrophages by clodronate administration leads to prolonged presence of activated HSCs after single injection of a toxic dose of APAP or CCl_4. This was associated with mild ECM accumulation in the pericentral compartment of the liver lobule. However, this effect was transient since activated HSCs as well as ECM were eliminated within 1-2 weeks. While looking for the responsible mechanism, there was no detectable reversion of activated HSCs to the quiescent state. However, interestingly massive apoptosis of activated HSCs was detected (figure 4.4). Since, it is already known that apoptosis of activated HSCs results mainly of interaction with immune cells, leukocytes infiltration was checked in clodronate treated livers by immunostaining using anti-CD45 antibodies. Surprisingly, massive leukocyte infiltration arranged in clusters was detected, particularly in the pericentral compartment of the liver lobule. Further characterization via flow cytometry and immunohistochemical analyses revealed that these cell clusters consist of B, T, NK as well as dendritic cells (figure 4.4). This suggests that these cell types are responsible for elimination of activated HSCs as well as degradation of ECM in absence of macrophages.

NK cells are innate lymphoid cells and well known to possess anti-fibrotic properties and their blocking leads to enhanced liver fibrosis (Fasbender et al. 2016; Gao and Radaeva 2013). The cytotoxicity of NK cells is triggered by activation of its stimulatory receptors as well as some cytokines particularly IFN-γ (discussed in details in the introduction section, figure 1.10). NK cells inhibit liver fibrosis by killing of HSCs directly via expression of the death receptor ligand TRAIL (Gao and Radaeva 2013; Gao et al. 2009; Tian et al. 2013). Another anti-fibrotic mechanism of NK cells is the production of IFN-γ (Gao and Radaeva 2013; Gao et al. 2009; Tian et al. 2013; Weiskirchen and Tacke 2014). IFN-γ plays a duel role against activated HSCs: (1) direct inhibition of HSCs activation (Tian et al. 2013), and (2) upregulation of NKG2D (NK cells stimulatory receptor) and TRAIL expression on NK

cells which result in amplification of NK cells cytotoxicity against activated HSCs (Radaeva et al. 2006) (figure 4.5)

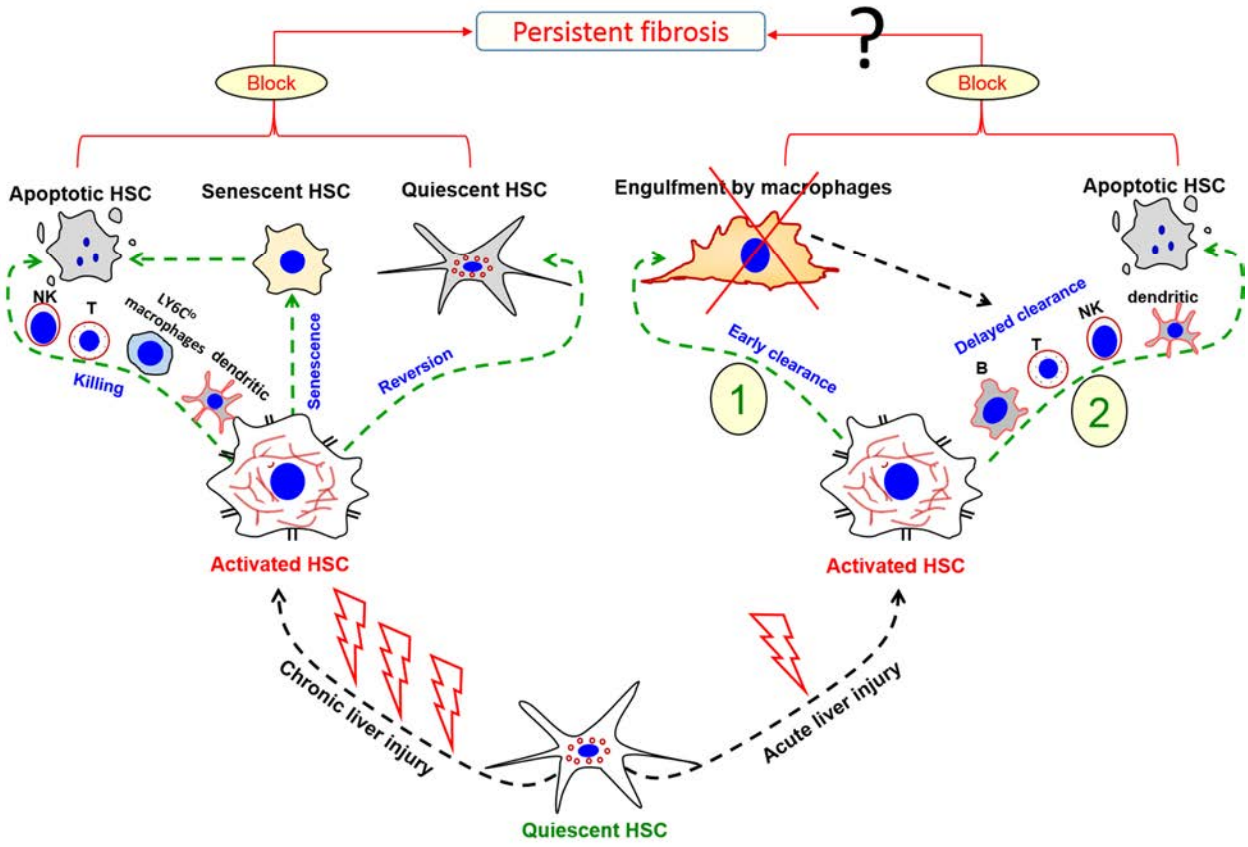

Figure 4. 4: Identification of a second backup mechanism of elimination of activated HSCs after macrophage removal during liver regeneration following acute challenge. The primary pathway for elimination of activated HSCs following a single exposure to a hepatotoxic compound is the direct engulfment by macrophages. This is a very efficient mechanism and does not lead to deposition of extracellular matrix. Removal of macrophages stimulates infiltration of a backup system for elimination of activated HSCs, which consists of B, T, NK and dendritic cells. These infiltrating cells lead to massive apoptosis of activated HSCs. However, this backup mechanism is less efficient and leads to transient deposition of collagen; but the liver also return to the normal state within 8-16 days.

Dendritic cells (DCs) are immature and tolerogenic in steady state (Lukacs-Kornek and Schuppan 2013). It was already reported that DCs exhibit fibrolytic properties after withdrawal of the causative agent of liver injury (Rahman and Aloman 2013; Seki and Schwabe 2015). Depletion of DCs during fibrosis recovery results in delayed resolution and reduced clearance of activated HSCs (Jiao et al. 2012; Ramachandran and Iredale 2012a). However, the anti-fibrotic mechanism of DCs is not fully understood. Some

studies showed that dendritic cell enhance ECM degradation via production of MMP9 (Jiao et al. 2012; Pellicoro et al. 2014; Ramachandran and Iredale 2012a; Tacke and Trautwein 2015). Other studies reported that DCs indirectly contribute to activated HSCs apoptosis via production of IFN-γ which induce NK cells activation (Okazaki et al. 2012; Tian et al. 2013) (figure 4.5).

The role of T cells in fibrogenesis/fibrosis regression is still unclear and most likely depends on the causative agent (Pellicoro et al. 2014). Using mice which are deficient in $CD4^+$ and $CD8^+$ T cells showed no difference in fibrosis development or regression following toxic liver injury (Novobrantseva et al. 2005; Pellicoro et al. 2014). In contrast, other studies showed that fusion of T cells with HSCs leads to fibrosis regression by upregulation of anti-fibrotic genes (Kornek et al. 2011). There are two important subtypes of T cells which have been reported to interact with activated HSCs: $CD4^+$ (T-helper) and gamma delta T (γδ-T) cells. $CD4^+T_H$ cells are sub-classified into T_H1, T_H2 and T_H17 cells (Heymann and Tacke 2016). The balance between T_H1 and T_H2 is important in response of $CD4^+$ cells to fibrosis. When T_H1 cells predominate this results in anti-fibrotic effects via the release of IFN-γ and IL-12. The later decreases expression of pro-fibrotic genes production by T_H2 cells (Muhanna et al. 2008; Pellicoro et al. 2014). Additionally, $CD4^+$ T cells induce activation of NK cells in a IL-2/NKG2D dependent manner, leading to amplification of NK cell cytotoxicity against activated HSCs (Fehniger et al. 2003; Glassner et al. 2013; He et al. 2004; Horowitz et al. 2010). The presence of DCs can also help in T cells activation via the production of IL-10 and TNF (Heymann and Tacke 2016; Mathan et al. 2013; Robinson et al. 2016). γδ-T cells represent 25% of liver T cell (Hammerich and Tacke 2014). Upon liver injury, γδ-T cells are recruited to the liver in a CCR6 – CCL20 chemokine dependent manner. These cells induce apoptosis of activated HSCs via expression of Fas ligand which binds to the death receptors Fas in activated HSCs (Hammerich et al. 2014).

The role of B cells in fibrogenesis and fibrosis regression is still not fully understood. (Novobrantseva et al. 2005) reported that absence of B cells attenuates liver fibrosis. However, they did not show any mechanism by which B cells induce fibrosis. Several studies have shown that B cells are involved in T cell activation (Holt et al. 2008; Parekh

et al. 2003; Tian et al. 2001) and thereby may indirectly contribute to HSCs apoptosis.

In conclusion, absence of macrophages during liver regeneration is replaced by a backup mechanism which induces apoptosis of activated HSCs and prevents liver fibrosis. This consists of NK cells, T cells (which induce apoptosis of activated HSCs), B cells (which activate T cells) and dendritic cells (which activate NK and T cells as well as induce matrix degradation).

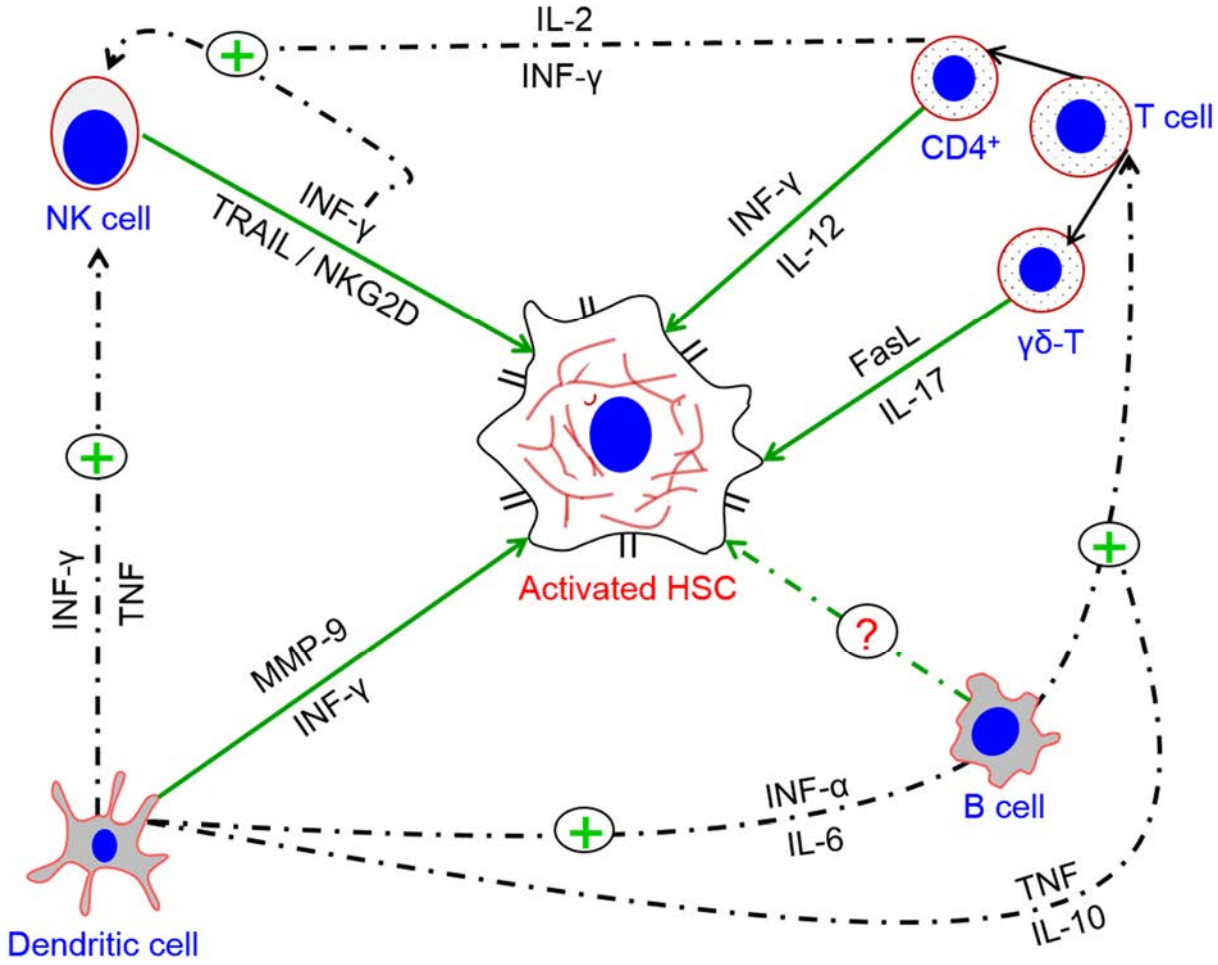

Figure 4. 5: Identification of backup mechanism for elimination of activated HSCs: in absence of macrophages massive infiltration of four cell types occurs during liver regeneration. The cooperation between these cells allows apoptosis of activated HSCs as well as degradation of extracellular matrix (ECM). These cells are: (1) NK cells, which induce apoptosis of activated HSCs; (2) T cells, which contribute to HSCs apoptosis and also amplify the cytotoxicity of NK cells via release of IL-2 and IFN-γ; (3) dendritic cells, which enhance ECM degradation via the release of MMP9 and also activate NK, B and T cells; and (4) B cells, which indirectly contribute to the elimination of activated HSCs via T cell activation.

5. Summary

Liver fibrosis is a wound healing process in case of repeated liver injury characterized by activation of hepatic stellate cells (HSCs) and excessive accumulation of extracellular matrix (ECM). Depending on the duration and the nature of injury, liver fibrosis can be reversible; via elimination of activated HSCs and degradation of ECM. In contrast to chronic liver injury efficient liver regeneration occurs following acute liver injury without fibrosis development. However, little is known about the state of HSCs following acute liver injury. Here, our goal was to investigate HSCs dynamics during liver injury and regeneration and to identify the mechanisms that protect against liver fibrosis. For this purpose, mouse models of acute (single dose of acetaminophen or carbon tetrachloride, CCl_4) and chronic (repeated CCl_4 intoxication) liver injury were used. Induction of acute liver injury by APAP or CCl_4 lead to massive killing of the pericentral hepatocytes. This was associated with massive activation and infiltration of HSCs into the dead cell area. However, these activated HSCs were efficiently eliminated within a week following liver injury without fibrosis development. In contrast, moderate cell killing and activation of HSCs following repeated liver injury lead to massive accumulation of ECM and fibrosis. Next, we investigated the mechanisms of activated HSCs elimination during liver recovery following acute and chronic damage scenarios. As already known, a fraction of activated HSCs reverts back to a quiescent phenotype during fibrosis recovery and a further fraction undergoes apoptosis. This effect was associated with massive infiltration of macrophages and NK cells. In contrast, although massive infiltration of macrophages was also observed following acute liver damage at the time when activated HSCs were eliminated, there was no reversion or apoptosis. It seems that activated HSCs are eliminated via direct engulfment by macrophages. This was supported by prolonged presence of activated HSCs after macrophage depletion. However, this prolonged preserve was transient, since activated HSCs were also eliminated within two weeks after induction of acute liver injury. Further analysis identified a backup mechanism of infiltrating immune cells (mainly B, T, NK and dendritic cells) which trigger apoptosis of activated HSCs in absence of macrophages. In conclusion, the efficient macrophage response following acute liver injury prevents liver fibrosis. When macrophages are

eliminated a backup mechanism of infiltrating immune cells becomes active and triggers apoptosis of activated HSCs.

6. Zusammenfassung

Die Leberfibrose ist Folge eines Wundheilungsprozesses bei wiederholten Leberbeschädigungen. Sie ist durch die Aktivierung von Sternzellen der Leber (HSC) und die übermäßige Ablagerung von extrazellulärer Matrix charakterisiert. In Abhängigkeit von Art und Intensität kann Leberfibrose reversibel sein. Im Gegensatz zu chronischer Leberschädigung regeneriert ein akuter Leberschaden ohne Fibrose. Allerdings ist nur wenig über die Bedeutung von HSC bei akuter Leberschädigung bekannt. Das Ziel dieser Arbeit bestand darin, den zeitlichen Verlauf der Aktivierung und Entfernung von HSC nach akuter Leberschädigung zu untersuchen und zu verstehen, warum in diesem Fall im Gegensatz zur chronischen Situation keine Fibrose entsteht. Um dieses Ziel zu erreichen wurden Mausmodelle mit akuter (einzelne hepatotoxische Dosen von Paracetamol oder CCl_4) und chronischer (wiederholte Applikation von CCl_4) eingesetzt. Die Verursachung akuter Leberschädigung durch Paracetamol oder CCl_4 führte wie erwartet zu einer massiven zentrilobulären Nekrose von Hepatozyten. Dies ging mit einer massiven Aktivierung von HSC und deren Einwanderung in das nekrotische Areal einher. Allerdings waren diese aktivierten HSC bereits eine Woche nach Induktion der Leberschädigung nicht mehr nachweisbar. Im Gegensatz zur akuten Situation führte die wiederholte Leberschädigung zu einer starken Anhäufung extrazellulärer Matrix (ECM) und Fibrose. Daher wurde als nächstes untersucht, welche Mechanismen zur Eliminierung der HSC im akuten und chronologischen Schadensszenario führen. Wie bereits bekannt wurde bei chronischer Schädigung beobachtet, dass aktivierte HSC entweder in einen ruhenden Zustand oder in Apoptose übergehen. Dies war mit einer starken Infiltration von natürlichen Killerzellen (NKC) und Makrophagen vergesellschaftet. Im Gegensatz zur chronischen Schädigung wurde nach akuter Intoxikation ebenfalls eine starke Infiltration von Makrophagen aber keine Apoptose von HSC beobachtet. Weitere Untersuchungen ergaben starke Hinweise darauf, dass aktivierte HSC in dieser Situation durch direkte Phagozytose durch Makrophagen entfernt werden. Dies konnte durch Depletion der Makrophagen bestätigt werden, wodurch es zu einer verlängerten Präsenz der HSC kam. Trotz der verlängerten Präsenz kam es jedoch zu einer späteren Entfernung der HSC innerhalb von etwa zwei Wochen nach akuter Leberschädigung. Weitere Untersuchungen zeigten, dass in diesem Zusammenhang andere Immunzellen als

Makrophagen, nämlich B-, T-, NK- und dendritische Zellen eine Rolle spielen. In Abwesenheit von Makrophagen scheinen diese die apoptische Antwort der HSC zu verursachen. Zusammenfassend kann festgestellt werden, dass es bei akuter Leberschädigung zu einer sehr effizienten Entfernung von aktivierten HSC durch Makrophagen kommt, wodurch Leberfibrose verhindert wird. Falls diese Makrophagenantwort eliminiert wird, kommt es zu einem Ersatzmechanismus infiltrierender Immunzellen, wodurch Apoptose von HSC verursacht wird.

7. References

Artis, D. and H. Spits (2015). "The biology of innate lymphoid cells." Nature 517(7534): 293-301.

Baeck, C., X. Wei, M. Bartneck, V. Fech, F. Heymann, N. Gassler, K. Hittatiya, D. Eulberg, T. Luedde, C. Trautwein and F. Tacke (2014). "Pharmacological inhibition of the chemokine C-C motif chemokine ligand 2 (monocyte chemoattractant protein 1) accelerates liver fibrosis regression by suppressing Ly-6C$^{(+)}$ macrophage infiltration in mice." Hepatology 59(3): 1060-1072.

Bajt, M. L., A. Ramachandran, H. M. Yan, M. Lebofsky, A. Farhood, J. J. Lemasters and H. Jaeschke (2011). "Apoptosis-inducing factor modulates mitochondrial oxidant stress in acetaminophen hepatotoxicity." Toxicol Sci 122(2): 598-605.

Bataller, R. and D. A. Brenner (2005). "Liver fibrosis." J Clin Invest 115(2): 209-218.

Bessems, J. G. and N. P. Vermeulen (2001). "Paracetamol (acetaminophen)-induced toxicity: molecular and biochemical mechanisms, analogues and protective approaches." Crit Rev Toxicol 31(1): 55-138.

Bohm, F., U. A. Kohler, T. Speicher and S. Werner (2010). "Regulation of liver regeneration by growth factors and cytokines." EMBO Mol Med 2(8): 294-305.

Canbay, A., P. Taimr, N. Torok, H. Higuchi, S. Friedman and G. J. Gores (2003). "Apoptotic body engulfment by a human stellate cell line is profibrogenic." Lab Invest 83(5): 655-663.

Ding, B. S., Z. Cao, R. Lis, D. J. Nolan, P. Guo, M. Simons, M. E. Penfold, K. Shido, S. Y. Rabbany and S. Rafii (2014). "Divergent angiocrine signals from vascular niche balance liver regeneration and fibrosis." Nature 505(7481): 97-102.

Duffield, J. S., S. J. Forbes, C. M. Constandinou, S. Clay, M. Partolina, S. Vuthoori, S. Wu, R. Lang and J. P. Iredale (2005). "Selective depletion of macrophages reveals distinct, opposing roles during liver injury and repair." J Clin Invest 115(1): 56-65.

Fallowfield, J. A., M. Mizuno, T. J. Kendall, C. M. Constandinou, R. C. Benyon, J. S. Duffield and J. P. Iredale (2007). "Scar-associated macrophages are a major source of hepatic matrix metalloproteinase-13 and facilitate the resolution of murine hepatic fibrosis." J Immunol 178(8): 5288-5295.

Fasbender, F., A. Widera, J. G. Hengstler and C. Watzl (2016). "Natural Killer Cells and Liver Fibrosis." Front Immunol 7: 19.

Fehniger, T. A., M. A. Cooper, G. J. Nuovo, M. Cella, F. Facchetti, M. Colonna and M. A. Caligiuri (2003). "CD^{56} bright natural killer cells are present in human lymph nodes and are activated by T cell-derived IL-2: a potential new link between adaptive and innate immunity." Blood 101(8): 3052-3057.

Feng, M., J. Y. Chen, R. Weissman-Tsukamoto, J. P. Volkmer, P. Y. Ho, K. M. McKenna, S. Cheshier, M. Zhang, N. Guo, P. Gip, S. S. Mitra and I. L. Weissman (2015).

"Macrophages eat cancer cells using their own calreticulin as a guide: roles of TLR and Btk." Proc Natl Acad Sci USA 112(7): 2145-2150.

Fiebig, T., H. Boll, G. Figueiredo, H. U. Kerl, S. Nittka, C. Groden, M. Kramer and M. A. Brockmann (2012). "Three-dimensional in vivo imaging of the murine liver: a micro-computed tomography-based anatomical study." PLoS One 7(2): e31179.

Fischer, R., A. Cariers, R. Reinehr and D. Haussinger (2002). "Caspase 9-dependent killing of hepatic stellate cells by activated Kupffer cells." Gastroenterology 123(3): 845-861.

Forbes, S. J. and N. Rosenthal (2014). "Preparing the ground for tissue regeneration: from mechanism to therapy." Nat Med 20(8): 857-869.

Friedman, S. L. (2012). "Fibrogenic cell reversion underlies fibrosis regression in liver." Proc Natl Acad Sci USA 109(24): 9230-9231.

Gao, B. and S. Radaeva (2013). "Natural killer and natural killer T cells in liver fibrosis." Biochim Biophys Acta 1832(7): 1061-1069.

Gao, B., S. Radaeva and O. Park (2009). "Liver natural killer and natural killer T cells: immunobiology and emerging roles in liver diseases." J Leukoc Biol 86(3): 513-528.

Gebhardt, R. (1992). "Metabolic zonation of the liver: regulation and implications for liver function." Pharmacol Ther 53(3): 275-354.

Ghallab, A., G. Celliere, S. G. Henkel, D. Driesch, S. Hoehme, U. Hofmann, S. Zellmer, P. Godoy, A. Sachinidis, M. Blaszkewicz, R. Reif, R. Marchan, L. Kuepfer, D. Haussinger, D. Drasdo, R. Gebhardt and J. G. Hengstler (2016). "Model-guided identification of a therapeutic strategy to reduce hyperammonemia in liver diseases." J Hepatol 64(4): 860-871.

Glassner, A., M. Eisenhardt, P. Kokordelis, B. Kramer, F. Wolter, H. D. Nischalke, C. Boesecke, T. Sauerbruch, J. K. Rockstroh, U. Spengler and J. Nattermann (2013). "Impaired $CD4^{(+)}$ T cell stimulation of NK cell anti-fibrotic activity may contribute to accelerated liver fibrosis progression in HIV/HCV patients." J Hepatol 59(3): 427-433.

Guicciardi, M. E., G. J. Gores and H. Jaeschke (2015). "Acetaminophen knocks on death's door and receptor interacting protein 1 kinase answers." Hepatology 62(6): 1664-1666.

Gur, C., S. Doron, S. Kfir-Erenfeld, E. Horwitz, L. Abu-Tair, R. Safadi and O. Mandelboim (2012). "NKp46-mediated killing of human and mouse hepatic stellate cells attenuates liver fibrosis." Gut 61(6): 885-893.

Hammerich, L., J. M. Bangen, O. Govaere, H. W. Zimmermann, N. Gassler, S. Huss, C. Liedtke, I. Prinz, S. A. Lira, T. Luedde, T. Roskams, C. Trautwein, F. Heymann and F. Tacke (2014). "Chemokine receptor CCR6-dependent accumulation of gammadelta T cells in injured liver restricts hepatic inflammation and fibrosis." Hepatology 59(2): 630-642.

Hammerich, L. and F. Tacke (2014). "Role of gamma-delta T cells in liver inflammation and fibrosis." World J Gastrointest Pathophysiol 5(2): 107-113.

Han, D., L. Dara, S. Win, T. A. Than, L. Yuan, S. Q. Abbasi, Z. X. Liu and N. Kaplowitz (2013). "Regulation of drug-induced liver injury by signal transduction pathways: critical role of mitochondria." Trends Pharmacol Sci 34(4): 243-253.

He, X. S., M. Draghi, K. Mahmood, T. H. Holmes, G. W. Kemble, C. L. Dekker, A. M. Arvin, P. Parham and H. B. Greenberg (2004). "T cell-dependent production of IFN-gamma by NK cells in response to influenza A virus." J Clin Invest 114(12): 1812-1819.

Henderson, N. C. and J. P. Iredale (2007). "Liver fibrosis: cellular mechanisms of progression and resolution." Clin Sci (Lond) 112(5): 265-280.

Heymann, F. and F. Tacke (2016). "Immunology in the liver--from homeostasis to disease." Nat Rev Gastroenterol Hepatol 13(2): 88-110.

Hinson, J. A., D. W. Roberts and L. P. James (2010). "Mechanisms of acetaminophen-induced liver necrosis." Handb Exp Pharmacol(196): 369-405.

Hoehme, S., M. Brulport, A. Bauer, E. Bedawy, W. Schormann, M. Hermes, V. Puppe, R. Gebhardt, S. Zellmer, M. Schwarz, E. Bockamp, T. Timmel, J. G. Hengstler and D. Drasdo (2010). "Prediction and validation of cell alignment along microvessels as order principle to restore tissue architecture in liver regeneration." Proc Natl Acad Sci USA 107(23): 10371-10376.

Hollander, C. F., C. F. van Bezooijen and H. A. Solleveld (1987). "Anatomy, function and aging in the mouse liver." Arch Toxicol Suppl 10: 244-250.

Holt, A. P., M. Salmon, C. D. Buckley and D. H. Adams (2008). "Immune interactions in hepatic fibrosis." Clin Liver Dis 12(4): 861-882, x.

Horowitz, A., K. C. Newman, J. H. Evans, D. S. Korbel, D. M. Davis and E. M. Riley (2010). "Cross-talk between T cells and NK cells generates rapid effector responses to Plasmodium falciparum-infected erythrocytes." J Immunol 184(11): 6043-6052.

Iredale, J. P. (2007). "Models of liver fibrosis: exploring the dynamic nature of inflammation and repair in a solid organ." J Clin Invest 117(3): 539-548.

Iredale, J. P., R. C. Benyon, J. Pickering, M. McCullen, M. Northrop, S. Pawley, C. Hovell and M. J. Arthur (1998). "Mechanisms of spontaneous resolution of rat liver fibrosis. Hepatic stellate cell apoptosis and reduced hepatic expression of metalloproteinase inhibitors." J Clin Invest 102(3): 538-549.

Ishibashi, H., M. Nakamura, A. Komori, K. Migita and S. Shimoda (2009). "Liver architecture, cell function, and disease." Semin Immunopathol 31(3): 399-409.

Jaeschke, H. (2005). "Role of inflammation in the mechanism of acetaminophen-induced hepatotoxicity." Expert Opin Drug Metab Toxicol 1(3): 389-397.

Jaeschke, H., T. R. Knight and M. L. Bajt (2003). "The role of oxidant stress and reactive nitrogen species in acetaminophen hepatotoxicity." Toxicol Lett 144(3): 279-288.

Jaeschke, H., M. R. McGill, C. D. Williams and A. Ramachandran (2011). "Current issues with acetaminophen hepatotoxicity--a clinically relevant model to test the efficacy of natural products." Life Sci 88(17-18): 737-745.

Jiang, J. X., K. Mikami, S. Venugopal, Y. Li and N. J. Torok (2009). "Apoptotic body engulfment by hepatic stellate cells promotes their survival by the JAK/STAT and Akt/NF-kappaB-dependent pathways." J Hepatol 51(1): 139-148.

Jiao, J., D. Sastre, M. I. Fiel, U. E. Lee, Z. Ghiassi-Nejad, F. Ginhoux, E. Vivier, S. L. Friedman, M. Merad and C. Aloman (2012). "Dendritic cell regulation of carbon tetrachloride-induced murine liver fibrosis regression." Hepatology 55(1): 244-255.

Jollow, D. J., J. R. Mitchell, W. Z. Potter, D. C. Davis, J. R. Gillette and B. B. Brodie (1973). "Acetaminophen-induced hepatic necrosis. II. Role of covalent binding in vivo." J Pharmacol Exp Ther 187(1): 195-202.

Ju, C. and F. Tacke (2016). "Hepatic macrophages in homeostasis and liver diseases: from pathogenesis to novel therapeutic strategies." Cell Mol Immunol 13(3): 316-327.

Jungermann, K. and T. Kietzmann (1996). "Zonation of parenchymal and nonparenchymal metabolism in liver." Annu Rev Nutr 16: 179-203.

Katz, N., H. F. Teutsch, K. Jungermann and D. Sasse (1977). "Heterogeneous reciprocal localization of fructose-1,6-bisphosphatase and of glucokinase in microdissected periportal and perivenous rat liver tissue." FEBS Lett 83(2): 272-276.

Kim, K. H., C. C. Chen, R. I. Monzon and L. F. Lau (2013). "Matricellular protein CCN1 promotes regression of liver fibrosis through induction of cellular senescence in hepatic myofibroblasts." Mol Cell Biol 33(10): 2078-2090.

Kisseleva, T., M. Cong, Y. Paik, D. Scholten, C. Jiang, C. Benner, K. Iwaisako, T. Moore-Morris, B. Scott, H. Tsukamoto, S. M. Evans, W. Dillmann, C. K. Glass and D. A. Brenner (2012). "Myofibroblasts revert to an inactive phenotype during regression of liver fibrosis." Proc Natl Acad Sci USA 109(24): 9448-9453.

Kong, D., F. Zhang, Z. Zhang, Y. Lu and S. Zheng (2013). "Clearance of activated stellate cells for hepatic fibrosis regression: molecular basis and translational potential." Biomed Pharmacother 67(3): 246-250.

Kornek, M., Y. Popov, T. A. Libermann, N. H. Afdhal and D. Schuppan (2011). "Human T cell microparticles circulate in blood of hepatitis patients and induce fibrolytic activation of hepatic stellate cells." Hepatology 53(1): 230-242.

Krizhanovsky, V., M. Yon, R. A. Dickins, S. Hearn, J. Simon, C. Miething, H. Yee, L. Zender and S. W. Lowe (2008). "Senescence of activated stellate cells limits liver fibrosis." Cell 134(4): 657-667.

Liedtke, C., T. Luedde, T. Sauerbruch, D. Scholten, K. Streetz, F. Tacke, R. Tolba, C. Trautwein, J. Trebicka and R. Weiskirchen (2013). "Experimental liver fibrosis research: update on animal models, legal issues and translational aspects." Fibrogenesis Tissue Repair 6(1): 19.

Lukacs-Kornek, V. and D. Schuppan (2013). "Dendritic cells in liver injury and fibrosis: shortcomings and promises." J Hepatol 59(5): 1124-1126.

Malarkey, D. E., K. Johnson, L. Ryan, G. Boorman and R. R. Maronpot (2005). "New insights into functional aspects of liver morphology." Toxicol Pathol 33(1): 27-34.

Mallat, A. and S. Lotersztajn (2013). "Cellular mechanisms of tissue fibrosis. 5. Novel insights into liver fibrosis." Am J Physiol Cell Physiol 305(8): C789-799.

Maroni, L., B. Haibo, D. Ray, T. Zhou, Y. Wan, F. Meng, M. Marzioni and G. Alpini (2015). "Functional and structural features of cholangiocytes in health and disease." Cell Mol Gastroenterol Hepatol 1(4): 368-380.

Marques, P. E., A. G. Oliveira, R. V. Pereira, B. A. David, L. F. Gomides, A. M. Saraiva, D. A. Pires, J. T. Novaes, D. O. Patricio, D. Cisalpino, Z. Menezes-Garcia, W. M. Leevy, S. E. Chapman, G. Mahecha, R. E. Marques, R. Guabiraba, V. P. Martins, D. G. Souza, D. S. Mansur, M. M. Teixeira, M. F. Leite and G. B. Menezes (2015). "Hepatic DNA deposition drives drug-induced liver injury and inflammation in mice." Hepatology 61(1): 348-360.

Masten, B. J., G. K. Olson, D. F. Kusewitt and M. F. Lipscomb (2004). "Flt3 ligand preferentially increases the number of functionally active myeloid dendritic cells in the lungs of mice." J Immunol 172(7): 4077-4083.

Mathan, T. S., C. G. Figdor and S. I. Buschow (2013). "Human plasmacytoid dendritic cells: from molecules to intercellular communication network." Front Immunol 4: 372.

McCuskey, R. S. (2006). "Anatomy of the liver." Hepatology a text book of liver disease fifth edition: 3-19.

McGill, M. R., C. D. Williams, Y. Xie, A. Ramachandran and H. Jaeschke (2012). "Acetaminophen-induced liver injury in rats and mice: comparison of protein adducts, mitochondrial dysfunction, and oxidative stress in the mechanism of toxicity." Toxicol Appl Pharmacol 264(3): 387-394.

McHedlidze, T., M. Waldner, S. Zopf, J. Walker, A. L. Rankin, M. Schuchmann, D. Voehringer, A. N. McKenzie, M. F. Neurath, S. Pflanz and S. Wirtz (2013). "Interleukin-33-dependent innate lymphoid cells mediate hepatic fibrosis." Immunity 39(2): 357-371.

Michalopoulos, G. K. (2007). "Liver regeneration." J Cell Physiol 213(2): 286-300.

Michalopoulos, G. K. and M. DeFrances (2005). "Liver regeneration." Adv Biochem Eng Biotechnol 93: 101-134.

Mitchell, J. R., D. J. Jollow, W. Z. Potter, D. C. Davis, J. R. Gillette and B. B. Brodie (1973). "Acetaminophen-induced hepatic necrosis. I. Role of drug metabolism." J Pharmacol Exp Ther 187(1): 185-194.

Moles, A., L. Murphy, C. L. Wilson, J. B. Chakraborty, C. Fox, E. J. Park, J. Mann, F. Oakley, R. Howarth, J. Brain, S. Masson, M. Karin, E. Seki and D. A. Mann (2014). "A TLR2/S100A9/CXCL-2 signaling network is necessary for neutrophil recruitment in acute and chronic liver injury in the mouse." J Hepatol 60(4): 782-791.

Muhanna, N., S. Doron, O. Wald, A. Horani, A. Eid, O. Pappo, S. L. Friedman and R. Safadi (2008). "Activation of hepatic stellate cells after phagocytosis of lymphocytes: A novel pathway of fibrogenesis." Hepatology 48(3): 963-977.

Nakatani, K., K. Kaneda, S. Seki and Y. Nakajima (2004). "Pit cells as liver-associated natural killer cells: morphology and function." Med Electron Microsc 37(1): 29-36.

New, L. S. and E. C. Chan (2008). "Evaluation of BEH C18, BEH HILIC, and HSS T3 (C18) column chemistries for the UPLC-MS-MS analysis of glutathione, glutathione disulfide, and ophthalmic acid in mouse liver and human plasma." J Chromatogr Sci 46(3): 209-214.

Novobrantseva, T. I., G. R. Majeau, A. Amatucci, S. Kogan, I. Brenner, S. Casola, M. J. Shlomchik, V. Koteliansky, P. S. Hochman and A. Ibraghimov (2005). "Attenuated liver fibrosis in the absence of B cells." J Clin Invest 115(11): 3072-3082.

Okazaki, A., N. Hiraga, M. Imamura, C. N. Hayes, M. Tsuge, S. Takahashi, H. Aikata, H. Abe, D. Miki, H. Ochi, C. Tateno, K. Yoshizato, H. Ohdan and K. Chayama (2012). "Severe necroinflammatory reaction caused by natural killer cell-mediated Fas/Fas ligand interaction and dendritic cells in human hepatocyte chimeric mouse." Hepatology 56(2): 555-566.

Parekh, V. V., D. V. Prasad, P. P. Banerjee, B. N. Joshi, A. Kumar and G. C. Mishra (2003). "B cells activated by lipopolysaccharide, but not by anti-Ig and anti-CD40 antibody, induce anergy in CD8+ T cells: role of TGF-beta 1." J Immunol 170(12): 5897-5911.

Pellicoro, A., P. Ramachandran, J. P. Iredale and J. A. Fallowfield (2014). "Liver fibrosis and repair: immune regulation of wound healing in a solid organ." Nat Rev Immunol 14(3): 181-194.

Pollheimer, M. J., P. Fickert and B. Stieger (2014). "Chronic cholestatic liver diseases: clues from histopathology for pathogenesis." Mol Aspects Med 37: 35-56.

Pradere, J. P., J. Kluwe, S. De Minicis, J. J. Jiao, G. Y. Gwak, D. H. Dapito, M. K. Jang, N. D. Guenther, I. Mederacke, R. Friedman, A. C. Dragomir, C. Aloman and R. F. Schwabe (2013). "Hepatic macrophages but not dendritic cells contribute to liver fibrosis by promoting the survival of activated hepatic stellate cells in mice." Hepatology 58(4): 1461-1473.

Radaeva, S., R. Sun, B. Jaruga, V. T. Nguyen, Z. Tian and B. Gao (2006). "Natural killer cells ameliorate liver fibrosis by killing activated stellate cells in NKG2D-dependent and tumor necrosis factor-related apoptosis-inducing ligand-dependent manners." Gastroenterology 130(2): 435-452.

Rahman, A. H. and C. Aloman (2013). "Dendritic cells and liver fibrosis." Biochim Biophys Acta 1832(7): 998-1004.

Ramachandran, P. and J. P. Iredale (2012a). "Liver fibrosis: a bidirectional model of fibrogenesis and resolution." QJM 105(9): 813-817.

Ramachandran, P. and J. P. Iredale (2012b). "Macrophages: central regulators of hepatic fibrogenesis and fibrosis resolution." J Hepatol 56(6): 1417-1419.

Ramachandran, P., A. Pellicoro, M. A. Vernon, L. Boulter, R. L. Aucott, A. Ali, S. N. Hartland, V. K. Snowdon, A. Cappon, T. T. Gordon-Walker, M. J. Williams, D. R. Dunbar, J. R. Manning, N. van Rooijen, J. A. Fallowfield, S. J. Forbes and J. P. Iredale (2012). "Differential Ly-6C expression identifies the recruited macrophage phenotype, which orchestrates the regression of murine liver fibrosis." Proc Natl Acad Sci USA 109(46): E3186-3195.

Ramadori, G., F. Moriconi, I. Malik and J. Dudas (2008). "Physiology and pathophysiology of liver inflammation, damage and repair." J Physiol Pharmacol 59 Suppl 1: 107-117.

Reif, R., A. Ghallab, L. Beattie, G. Gunther, L. Kuepfer, P. M. Kaye and J. G. Hengstler (2017). "In vivo imaging of systemic transport and elimination of xenobiotics and endogenous molecules in mice." Arch Toxicol 91(3): 1335-1352.

Robinson, M. W., C. Harmon and C. O'Farrelly (2016). "Liver immunology and its role in inflammation and homeostasis." Cell Mol Immunol 13(3): 267-276.

Saito, C., C. Zwingmann and H. Jaeschke (2010). "Novel mechanisms of protection against acetaminophen hepatotoxicity in mice by glutathione and N-acetylcysteine." Hepatology 51(1): 246-254.

Seki, E., S. De Minicis, C. H. Osterreicher, J. Kluwe, Y. Osawa, D. A. Brenner and R. F. Schwabe (2007). "TLR4 enhances TGF-beta signaling and hepatic fibrosis." Nat Med 13(11): 1324-1332.

Seki, E. and R. F. Schwabe (2015). "Hepatic inflammation and fibrosis: functional links and key pathways." Hepatology 61(3): 1066-1079.

Senoo, H. (2004). "Structure and function of hepatic stellate cells." Med Electron Microsc 37(1): 3-15.

Shen, K., W. Chang, X. Gao, H. Wang, W. Niu, L. Song and X. Qin (2011). "Depletion of activated hepatic stellate cell correlates with severe liver damage and abnormal liver regeneration in acetaminophen-induced liver injury." Acta Biochim Biophys Sin (Shanghai) 43(4): 307-315.

Skrtic, S., V. Wallenius, S. Ekberg, A. Brenzel, A. M. Gressner and J. O. Jansson (1999). "Hepatocyte-stimulated expression of hepatocyte growth factor (HGF) in cultured rat hepatic stellate cells." J Hepatol 30(1): 115-124.

Stockert, R. J. and A. W. Wolkoff (2001). "Cellular and molecular biology of the liver." Curr Opin Gastroenterol 17(3): 205-210.

Tacke, F. and C. Trautwein (2015). "Mechanisms of liver fibrosis resolution." J Hepatol 63(4): 1038-1039.

Tacke, F. and H. W. Zimmermann (2014). "Macrophage heterogeneity in liver injury and fibrosis." J Hepatol 60(5): 1090-1096.

Taub, R. (2004). "Liver regeneration: from myth to mechanism." Nat Rev Mol Cell Biol 5(10): 836-847.

te Koppele, J. M. and R. G. Thurman (1990). "Phagocytosis by Kupffer cells predominates in pericentral regions of the liver lobule." Am J Physiol 259(5 Pt 1): G814-821.

Thoolen, B., R. R. Maronpot, T. Harada, A. Nyska, C. Rousseaux, T. Nolte, D. E. Malarkey, W. Kaufmann, K. Kuttler, U. Deschl, D. Nakae, R. Gregson, M. P. Vinlove, A. E. Brix, B. Singh, F. Belpoggi and J. M. Ward (2010). "Proliferative and nonproliferative lesions of the rat and mouse hepatobiliary system." Toxicol Pathol 38(7 Suppl): 5S-81S.

Tian, J., D. Zekzer, L. Hanssen, Y. Lu, A. Olcott and D. L. Kaufman (2001). "Lipopolysaccharide-activated B cells down-regulate Th1 immunity and prevent autoimmune diabetes in nonobese diabetic mice." J Immunol 167(2): 1081-1089.

Tian, Z., Y. Chen and B. Gao (2013). "Natural killer cells in liver disease." Hepatology 57(4): 1654-1662.

Troeger, J. S., I. Mederacke, G. Y. Gwak, D. H. Dapito, X. Mu, C. C. Hsu, J. P. Pradere, R. A. Friedman and R. F. Schwabe (2012). "Deactivation of hepatic stellate cells during liver fibrosis resolution in mice." Gastroenterology 143(4): 1073-1083 e1022.

Vollmar, B. and M. D. Menger (2009). "The hepatic microcirculation: mechanistic contributions and therapeutic targets in liver injury and repair." Physiol Rev 89(4): 1269-1339.

Wang, H., T. Peters, A. Sindrilaru and K. Scharffetter-Kochanek (2009). "Key role of macrophages in the pathogenesis of CD18 hypomorphic murine model of psoriasis." J Invest Dermatol 129(5): 1100-1114.

Wang, L. and J. L. Boyer (2004). "The maintenance and generation of membrane polarity in hepatocytes." Hepatology 39(4): 892-899.

Wang, X., X. Wu, A. Zhang, S. Wang, C. Hu, W. Chen, Y. Shen, R. Tan, Y. Sun and Q. Xu (2016). "Targeting the PDGF-B/PDGFR-beta Interface with Destruxin A5 to Selectively Block PDGF-BB/PDGFR-betabeta Signaling and Attenuate Liver Fibrosis." EBioMedicine 7: 146-156.

Weiskirchen, R. and F. Tacke (2014). "Cellular and molecular functions of hepatic stellate cells in inflammatory responses and liver immunology." Hepatobiliary Surg Nutr 3(6): 344-363.

Williams, C. D., M. L. Bajt, A. Farhood and H. Jaeschke (2010). "Acetaminophen-induced hepatic neutrophil accumulation and inflammatory liver injury in CD18-deficient mice." Liver Int 30(9): 1280-1292.

Xu, J., X. Liu, Y. Koyama, P. Wang, T. Lan, I. G. Kim, I. H. Kim, H. Y. Ma and T. Kisseleva (2014). "The types of hepatic myofibroblasts contributing to liver fibrosis of different etiologies." Front Pharmacol 5: 167.

Yin, C., K. J. Evason, K. Asahina and D. Y. Stainier (2013). "Hepatic stellate cells in liver development, regeneration, and cancer." J Clin Invest 123(5): 1902-1910.

Zhan, S. S., J. X. Jiang, J. Wu, C. Halsted, S. L. Friedman, M. A. Zern and N. J. Torok (2006). "Phagocytosis of apoptotic bodies by hepatic stellate cells induces NADPH oxidase and is associated with liver fibrosis in vivo." Hepatology 43(3): 435-443.

Zigmond, E., S. Samia-Grinberg, M. Pasmanik-Chor, E. Brazowski, O. Shibolet, Z. Halpern and C. Varol (2014). "Infiltrating monocyte-derived macrophages and resident kupffer cells display different ontogeny and functions in acute liver injury." J Immunol 193(1): 344-353.

Zook, E. C. and B. L. Kee (2016). "Development of innate lymphoid cells." Nat Immunol 17(7): 775-782.

List of publications

Hassan R," Highlight Report: Possibilities and limitations of intravital imaging". ***EXCLI Journal*** 15 (2016): 872-874. ***(impact factor: 1.292).***

Hassan R. "Highlight Report: Adaptations of the biliary tree to cholestasis." ***Arch Toxicol*** (2017), accepted. ***(impact factor: 6.673).***

Schenk A, A. Ghallab, U. Hofmann, **R. Hassan**, M. Schwarz, A. Schuppert, O. Schwen, A. Braeuning, D. Teutonico, JG. Hengstler and L. Kuepfer. "Physiologically-based modelling in mice suggests an aggravated loss of clearance capacity after toxic liver damage." ***Scientific Reports*** 7 (2017): 6224. ***(impact factor: 5.228).***

8. Erklärung

Ich erkläre:

Ich habe die vorgelegte Dissertation selbständig, ohne unerlaubte fremde Hilfe und nur mit den Hilfen angefertigt, die ich in der Dissertation angegeben habe. Alle Textstellen, die wörtlich oder sinngemäß aus veröffentlichten oder nicht veröffentlichten Schriften entnommen sind, und alle Angaben, die auf mündlichen Auskünften beruhen, sind als solche kenntlich gemacht. Bei den von mir durchgeführten und in der Dissertation erwähnten Untersuchungen habe ich die Grundsätze guter wissenschaftlicher Praxis, wie sie in der „Satzung der Justus-Liebig-Universität Gießen zur Sicherung guter wissenschaftlicher Praxis“ niedergelegt sind, eingehalten.

Reham Hassan

Acknowledgments

I am very grateful to **Prof. Dr. med. Jan G. Hengstler** for giving me the opportunity to do my PhD at IfADo. Thank you very much for the supervision, fruitful discussion, guidance and continuous support.

I would like to express my deepest respect to **Prof. Dr. Joachim Geyer** for his guidance and professional supervision during my work. Thank you very much for the opportunity to get my PhD from Giessen University.

Many thanks to Prof. Dr. Abdel latif Shaker Seddek for his continuous help, support and his personal kindness.

I would like to thank my co-supervisor Dr. Ahmed Ghallab for his supervision, continuous support and the brilliant ideas during all my PhD work.

Special thanks to Ms. Simone keil for the daily help and competent technical assistance.

I want also to thank Ms. Brigitte Begher-Tibbe who help me a lot especially in the architectural staining and 3D reconstruction.

Many thanks to Dr. Agata Widera for supporting me in flow cytometry analyses.

Special thanks to Dr. Meinolf Blaszkewicz for helping me in glutathione assay.

I want also to thank Dr. Martin Vonbergen for helping me in measuring acetaminophen and its metabolites in blood.

I would like to thank Ms. Silke Hankinson, Ms. Monika Turajski, Ms. Beate Graf and Ms. Viviane Lopes for their help and support in all administrative documents.

I am very grateful to Dr. Patricio Godoy, Dr. Raymond Reif, Dr. Cristina Cadenas, Dr. Rosemarie Marchan, Dr. Gisela Campos, Dr. Regina Stöber, Dr. Wolfram Foellmann and Ms. Georgia Guenther for the continuous helpful discussion and support.

My special thanks should go to my dear parents, my brother and my sister. You are waiting this day when I am coming to say “I finished”. Thank you very much for praying, support and encouragement throughout all these years. I would like also to thank my husband’s family, his parents and brothers, they encourage me always with love and praying.

My deepest heartfelt thanks to my dear husband Ahmed Ghallab for his patience, continuous kindness and encouragement. This work was done only because you are in my life. Finally I would like to thank my little cute princess Alaa for her smiling which encourage me during this hard period in my life, I want to say to you and to your Dad “you are my life”.